• U C •

FCTUC FACULDADE DE CIÊNCIAS
E TECNOLOGIA
UNIVERSIDADE DE COIMBRA

Nuno Miguel Saraiva Santos

Development of a New, Improved Deep-Brain Transcranial Magnetic Stimulator (TMS)

A dissertation submitted in fulfilment of the requirements
for the degree of Master of Science in Biomedical Engineering

at the

Laboratório de Instrumentação e Física Experimental de Partículas
Departamento de Física

Supervisor:
Prof. Paulo Alexandre Vieira Crespo

Co-supervisors:
Prof. Ricardo Nuno Braço Forte Salvador
Prof. João Carlos Gonçalves Silvestre

Coimbra, 2015

This work was developed in collaboration with:

Departamento de Física, Faculdade de Ciências e Tecnologia,
Universidade de Coimbra

UNIVERSIDADE DE COIMBRA

Laboratório de Instrumentação e Física Experimental de Partículas

Instituto de Biofísica e Engenharia Biomédica,
Universidade de Lisboa

Instituto Superior de Engenharia de Coimbra

Para ti Mãe, para ti Pai

Acknowledgements

Ao meu orientador, Professor Paulo Crespo, por todo o apoio prestado, disponibilidade, compreensão, entusiasmo e todo o conhecimento que partilhou comigo. Um grande obrigado por me ter ensinado a dar valor a todas as pequenas grandes vitórias que fomos conquistando ao longo deste percurso.

Aos coorientadores deste trabalho, Professor Ricardo Salvador e Professor João Silvestre e ainda ao Professor Pedro Cavaleiro Miranda por todas as valiosas sugestões e indicações que enriqueceram bastante esta dissertação e sem as quais não teria sido possível alcançar todos os objetivos.

Aos meus futuros colegas, Engº Hugo e Engª Sónia. Obrigado por toda a ajuda, todas as dicas, por me guiarem ao longo de todo este tempo e por partilharem comigo parte das vossas experiências e conhecimentos. Foram sem dúvida um grande suporte e este trabalho não teria sido o mesmo sem vocês.

Ao Professor Francisco pela contribuição nos trabalhos experimentais e à Professora Emília por toda a motivação e por me ter ensinado a ser um pouco mais "cientista".

A todas as instituições envolvidas que tão bem me acolheram, com um agradecimento especial à direção do LIP pela oportunidade e pelo apoio e ao pessoal da secretaria e da oficina do LIP que sempre se mostraram disponíveis e prontos a ajudar.

A todos os meus amigos com os quais partilhei estes cinco anos fantásticos e que fizeram com que Coimbra fique para sempre na minha memória. Obrigado aos meus colegas de casa, João e Pinheiro, ao pessoal do futebol, à minha família de praxe e a todos com o quais me cruzei neste percurso académico. Não tenho palavras para vocês!

A toda a minha família por sempre me acompanharem, apoiarem e fazerem de mim a pessoa que sou hoje. Um eterno obrigado aos meus avós Pedro, António, Isabel e Emília. Este trabalho também é para vocês.

À Andreia, por todo o amor, dedicação e companhia. Obrigado por estares sempre presente e por me veres e fazeres crescer ao longo destes cinco anos.

Por último, ao meu mais novo, Renato, e aos meus pais Olga e Rui. Não há palavras que descrevam toda a minha gratidão por tudo o que fizeram por mim. Obrigado por sempre acreditarem em mim e me apoiarem incondicionalmente nas minhas escolhas. Todo este percurso e claro esta dissertação são inteiramente dedicados a vocês.

Abstract

The term transcranial magnetic stimulation (TMS) refers to the capability of inducing neurocurrents in the brain by the application of transient magnetic fields, properly generated and delivered through a stimulating coil. Since its introduction, about 30 years ago, this non-invasive technique has been widely used both for neuroscience research and, more recently, in the handling of refractory depression and migraine. However, many other clinical applications such as Alzheimer disease, Parkinson disease, schizophrenia or autism, may potentially benefit from the ability of TMS systems to neuromodulate deeply located brain regions with sufficient intensity, which remains inaccessible to standard TMS coils.

The present dissertation describes the optimisation work that allowed the proposal of a new TMS system, comprised of five large coils, termed orthogonal configuration, specifically designed to induce an electric field at the centre of the brain with unprecedented magnitude (60 % of the magnitude of the field induced at the superficial cortex). By immersing the whole system in a conducting liquid it was demonstrated, via COMSOL Multiphysics® AC/DC simulations, that such penetration capability clearly surpasses state of the art TMS devices. For the first time, the safety of the patient and of the system operator was guaranteed, through the implementation of a metal shielding structure, surrounding the 5-coil system and the patient head, able to reduce the current density induced in the patient(operator) torso by, at least, two(four) orders of magnitude.

In addition, a pioneer simulation study proved the importance of having conductive tissues around the brain, including the skull. The orthogonal configuration induces brain currents via TMS only. Nevertheless, we have found that, with the conductive liquid surrounding the patient brain, a strong component of the induced brain current arises by means of currents existing in all head interfaces, with the skull being the limiting medium.

Finally, a new power electronics system was designed and simulated, under PSpice®, towards the development of a high-frequency magnetic stimulator capable

of delivering TMS pulses up to 10 Hz, thus allowing the 5-coil system to apply excitatory TMS protocols.

Keywords: Transcranial Magnetic Stimulation; Deep Transcranial Magnetic Stimulation; Power electronics.

Resumo

A estimulação magnética transcraniana (TMS) é uma técnica não invasiva capaz de induzir correntes elétricas no tecido cerebral, através da aplicação de campos magnéticos transientes, gerados e aplicados a partir de uma bobina. Desde o seu aparecimento, em 1985, a TMS tem sido bastante utilizada quer em investigação académica quer na prática clínica, tendo sido recentemente aprovada para o tratamento da depressão refratária e enxaqueca. No entanto, doenças como esquizofrenia, doença de Alzheimer ou autismo poderiam beneficiar bastante se os sistemas atuais de TMS tivessem a capacidade de estimular regiões profundas do cérebro com a intensidade necessária à ativação neuronal.

A presente dissertação descreve todo o processo de otimização que serviu de base ao desenvolvimento, através do software COMSOL Multiphysics® AC/DC, de um novo sistema TMS, designado por configuração ortogonal, cujas cinco bobinas foram especificamente projetadas para induzir no centro do cérebro um campo elétrico com uma intensidade sem precedentes (60 % da intensidade do campo induzido à superfície do córtex), ultrapassando o estado da arte dos dispositivos de TMS. Para além deste resultado e pela primeira vez, conseguiu-se ainda garantir a segurança tanto do doente como do operador do sistema através da implementação de uma estrutura metálica em redor das 5 bobinas e da cabeça do paciente, que permitiu reduzir a valores negligenciáveis a densidade de corrente induzida no coração do doente/operador.

Através deste trabalho foi ainda possível provar a importância de existirem tecidos condutores em torno do cérebro, incluindo o crânio, que influenciam fortemente a distribuição de correntes induzidas no cérebro. É verdade que a indução de correntes provocada pela configuração ortogonal se baseia apenas na TMS. No entanto, a existência de líquido condutor envolvendo a cabeça do paciente possibilita a existência de uma corrente elétrica no crânio que influencia fortemente a distribuição de corrente obtida no cérebro.

Finalmente, projetou-se um circuito de eletrónica de potência, através do PSpice®, capaz de alimentar o sistema proposto de 5 bobinas de tal forma a que

seja possível aplicar pulsos TMS a uma taxa de 10 Hz, um protocolo responsável por induzir respostas neuronais excitatórias.

Palavras-chave: Estimulação Magnética Transcraniana, Estimulação Magnética Transcraniana Profunda; Eletrónica de Potência.

Abbreviations

AC	**A**lternating **C**urrent
AH	**A**uditory **H**allucinations
AP	**A**ction **P**otential
ATP	**A**denosine **Tri**p**h**osphate
ASD	**A**utism **S**pectrum **D**isorder
B-field	Magnetic field
CNS	**C**entral **N**ervous **S**ystem
CS	**C**onditioning **S**timulus
CSF	**C**erebro**s**pinal **F**luid
cTMS	Near-rectangular **c**ontrollable-width **TMS** pulse
DC	**D**irect **C**urrent
dlPFC	**d**orso**l**ateral **P**re**f**rontal **C**ortex
dmPFC	**d**orso**m**edial **P**re**f**rontal **C**ortex
dTMS	**d**eep **T**ranscranial **M**agnetic **S**timulation
ECT	**E**lectro**c**onvulsive **T**herapy
EEG	**E**lectro**e**ncephalo**g**raphy
EMG	**E**lectro**m**yo**g**raphy
EMF	**E**lectro**m**agnetic **F**ields
E-field	**E**lectric field
H-coil	**H**esed coil
HF-rTMS	**H**igh-**F**requency **r**epetitive **T**ranscranial **M**agnetic **S**timulation
IGBT	**I**nsulated **G**ate **B**ipolar **T**ransistor
IPI	**I**nter-**P**ulse **I**nterval
ICNIRP	**I**nternational **C**omission on **N**on-**I**onizing **R**adiation **P**rotection

LF-rTMS	**L**ow-**F**requency **r**epetitive **T**ranscranial **M**agnetic **S**timulation
LTD	**L**ong-**T**erm **D**epression
LTP	**L**ong-**T**erm **P**otentiation
MDD	**M**ajor **D**epressive **D**isorder
MEP	**M**otor-**E**voked **P**otential
MSO	**M**aximum **S**timulator **O**utput
MT	**M**otor **T**hreshold
OC	**O**rtoghonal **C**onfiguration
PFC	**P**ref**f**rontal **C**ortex
PNS	**P**eripheral **N**ervous **S**ystem
ppTMS	**p**aired-**p**ulse **T**ranscranial **M**agnetic **S**timulation
PTSD	**P**ost-**T**raumatic **S**tress **D**isorder
rTMS	**r**epetitive **T**ranscranial **M**agnetic **S**timulation
RI	**R**elative **I**nduction
SCR	**S**ilicon **N**ontrolled **R**ectifier
SNS	**S**omatic **N**ervous **S**ystem
spTMS	**s**ingle-**p**ulse **T**ranscranial **M**agnetic **S**timulation
TBS	**T**heta **B**urst **S**timulation
TES	**T**ranscranial **E**lectrical **S**timulation
TMS	**T**ranscranial **M**agnetic **S**timulation
TS	**T**est **S**timulus
VEP	**V**isual-**E**voked **P**otential
vlPFC	**v**entro**l**ateral **P**ref**f**rontal **C**ortex

List of Figures

List of Tables

Index

Chapter 1

Introduction

The present chapter includes a brief description of the project that originated this dissertation. Such work was developed during the final year of the Biomedical Engineering Integrated Master.

Next, the main objectives are highlighted, so as the thesis motivation, structure and scientific contributions.

1.1 Objectives

The development of a new, improved deep-brain transcranial magnetic stimulator was this project main goal.

To achieve such purpose, several milestones were proposed at the beginning of this work.

- Familiarisation with the theoretical background on the relevant topics and the necessary literature research on state of the art deep transcranial magnetic stimulation (dTMS) devices and its applications.
- Development, via simulation, of a new five coil system embedded in conducting liquid.
- Simulation of a shielding structure for the proposed dTMS system in order to guarantee the safety of the patient and the system operator.

- Experimental validation of the simulated shielding results for different materials via electric potential readouts from a cylindrical container filled with saline solution and from two probe coils.
- Investigation of the existence and relevance of induced currents in all media comprising the head, including the skull.
- Study, by simulation, of the feasibility of a new power electronics system for the development of a high-frequency transcranial magnetic stimulator, to be constructed in the future.

All the outcome measures were obtained at LIP (Laboratório de Instrumentação e Física Experimental de Partículas) using a pulsed power electronics system already available.

1.2 Project Motivation

Transcranial magnetic stimulation (TMS), refers to a non-invasive procedure, proposed 30 years ago, capable of stimulating the human brain tissue. Through the application of coil generated transient (*i.e.* rapidly time-varying intensity) magnetic fields, TMS allows for induction of brain currents which lead to excitatory/inhibitory effects on neural activity.

As a constantly evolving technique, TMS has been the subject of numerous published studies regarding its promising ability to treat or improve therapeutic outcome for several neurological and psychological disorders such as Alzheimer Disease, stroke rehabilitation and post-traumatic stress disorder (PTSD). TMS protocols have been approved by the United States Food and Drug Administration (FDA) for the treatment of pharmacoresistant major depressive disorder (MDD) and to relieve migraine headache pain, in 2008 (Neuronetics Inc.) and 2013 (eNeura Inc.), respectively. In Europe, some devices also received European CE Mark approval for use both in diagnostic and therapeutic clinical practice. TMS pulses can be delivered one at a time, with a minimum interval of 3-4 seconds to

avoid influencing short-term plasticity[1], although other authors point to longer periods of time to avoid this, namely 10 seconds (Opitz et al., 2013), in a protocol termed single-pulsed TMS, or can be delivered repeatedly, in trains of pulses applied at the same intensity over one specific brain region. The latter technique is known as repetitive TMS (rTMS) and it is characterised by the frequency of stimulation and the structure of the train pulse (*i.e.* length of intertrain interval). With rTMS, one can induce long-term effects, namely facilitative or suppressive, accordingly to the stimuli frequency. Lower frequencies, in the range of 1 Hz, are known for decreasing neural activity in adjacent brain tissue, whereas higher frequencies, up to 50 Hz, lead to an excitatory effect thus increasing neurons excitability.

Being an electromagnetic induction based technique, conventional TMS coils can not overcome the exponentially decrease of the magnetic field intensity throughout the brain with the distance from the coil. Consequently, the induced current in the brain also decreases, which explains why the majority of TMS devices are still intended for cortex stimulation, *i.e.* stimulation of the superficial layers of the brain. Therefore the development and optimisation of new coil designs, allowing for deeper brain stimulation are of paramount importance, since it will open new therapeutic windows for the treatment of several conditions like schizophrenia, Alzheimer and Parkinson Disease.

Deep-brain TMS is a recent new technique with a very promising clinical potential. The main objective of the work presented here was to further optimise equipment design so that stimulation of these deeply located brain regions can become more effective.

LIP in collaboration with IBEB (Instituto de Biofísica e Engenharia Biomédica) and ISEC (Instituto Superior de Engenharia de Coimbra) have proposed an innovative TMS system based on a five coil configuration immersed in a conducting liquid. This system, termed Orthogonal Configuration (OC), allows the direct stimulation of deeper brain structures, including the centre of the brain. Previous simulation work (Sousa et al., 2014) yielded exciting results, achieving

[1]Short-term plasticity reflects the history of prior synaptic activity, consisting of synaptic efficacy changes (depression or facilitation) observed for only a few minutes after the activation.

more than 50 % relative induction at the centre of the brain model relative to surface maximum, although the safety of the patient and the system operator was not guaranteed by this previous system. Therefore, to assure the safety of all the ones involved in a future potential clinical use of the proposed system, it is necessary to study and predict via simulation, the dimensions and material to be used in a proper shielding structure, which is absolutely necessary because of the high magnetic field transient values.

Since the proposed system, to the best of our knowledge, was the first to use conducting liquid surrounding the patient head, there is a possibility that electrical conduction occurs within the conductive tissues of the head. Thus, it is crucial to understand whether the proposed dTMS system induces also electrical stimulation via the tissues that surround the head, including the skull.

Due to the improved therapeutic effects of rTMS, LIP is planning to develop a transcranial magnetic stimulator capable of delivering repetitive trains of pulses allowing the application of high-frequency rTMS protocols through the proposed new five-coil TMS system. The feasibility of such stimulator must be studied, particularly the design of new power electronics in order to construct the aforementioned stimulator in the near future.

1.3 Thesis structure

The present dissertation is divided into six chapters. A brief introduction to this work, Chapter 1, is followed by a more detailed description of the underlying physical and physiological principles of TMS as well as the state of the art devices and respective application, Chapter 2.

In the third chapter, it will be explained all the simulation and experimental work that lead to a new and improved five-coil dTMS system that had the patient and operator safety as the main concern.

The relevance of the currents induced within the surrounding tissues of the brain is discussed in Chapter 4, with particular attention to the skull tissue.

Additionally, in Chapter 5, a new power electronics system is proposed and two different configurations are simulated. This initial study was performed with the

purpose to develop a high-frequency rTMS device capable of feeding the five-coil system.

Finally, all the conclusions gathered along this work are summarised in the sixth chapter as well as some indications regarding future perspectives of this project.

1.4 Scientific contributions

The work entitled "Shielding The Magnetic Field From a Transcranial Stimulator Using Aluminium and Iron: Simulation And Experimental Results", developed in the scope of this project, was presented in the "2015 IEEE 4th Portuguese BioEngineering Meeting (ENBENG)", which took place in February 2015 in the city of Porto, Portugal.

The main results presented in this dissertation are also part of a scientific article, entitled "Multiple Coils Immersed in a Conducting Liquid for Whole-Brain or One-Hemisphere Deep Transcranial Magnetic and Electrical Stimulation: A Simulation Study", to be submitted to IEEE Transactions on Biomedical Engineering.

Both contributions demonstrate the scientific validity of the work developed in the scope of the present dissertation.

Chapter 2

Fundamentals of Transcranial Magnetic Stimulation

2.1 Overview of TMS

Transcranial magnetic stimulation (TMS) is a non-invasive neuromodulatory/neurostimulatory technique which has been increasingly used both in clinical and research practices. This modulatory effect can be either excitatory or inhibitory and either transient or more permanent where the neurobiological response remains for a relatively long time after the application of the TMS protocol. Despite its wider application for research purposes, TMS has also been proved to be a clinically useful technique both for diagnostic and therapeutic applications in neurology, psychiatry and rehabilitation (Horvath et al., 2011, Kobayashi and Pascual-Leone, 2003).

2.1.1 History and evolution of brain stimulation

The perception of electric and magnetic fields as a therapeutic tool dates back to about 2000 years ago and its use has been expanding since.

The first therapeutic application of electricity reports back to circa 46 AD when the Roman Scribonius Largus applied an electrical current on the scalp of patients with headaches. Nevertheless, it was not until the 18th century that the concept of electrophysiology appeared, by the hand of the Italian physician Luigi Galvani,

and the use of electrical stimulation for the treatment of several diseases became more recognised. Charles Le Roy and Giovanni Aldini, the nephew of Galvani, are considered pioneers in the application of direct current (DC) electrical stimulation (non-time-varying current) in order to treat or somehow relief several symptoms in neurological and psychiatric conditions (Vidal-Dourado et al., 2013).

Until this time, it was believed that magnetic and electric fields existed as separate and distinct phenomena. Nonetheless, by 1819, the idea that electrical currents are surrounded by magnetic fields was proposed by the Danish physicist Hans Christian Oersted who published his work reporting that a magnetic needle compass could be deflected only by the influence of an electrical current. Many more scientists followed Oersted hypothesis, Faraday, Ampère, Jean-Baptiste Biot and Felix Savart also contributed for the widely-spread belief that electricity and magnetism should be considered as two related quantities which are connected through space and time (Vidal-Dourado et al., 2013). Shortly after Oersted discovery of electromagnetism, the English Michael Faraday described the principle of electromagnetic induction, in 1831, which states that a transient electrical current flowing through a wire coil generates a time-varying magnetic field (Faraday, 1832). The opposite effect is also true, meaning that an electrical current can be induced in a coil by simply moving the coil within a static magnetic field, generated, for example, by a permanent magnet.

In 1874, Robert Bartholow, an American physician, studied the response of muscles and nerve fibres after the direct application of electrical currents over exposed tissues. Through the insertion of needle electrodes in a 30-year-old woman with a parietal epithelioma, and after successive alternating current (AC) electrical stimulation, Bartholow reported loss of consciousness, epileptic seizure followed by coma and death. Consequently, Bartholow methodology was heavily criticised but it was of paramount importance since it raised ethical issues and dilemmas regarding the risk-to-benefit assessment of electrical stimulation protocols (Horvath et al., 2011).

Regarding the use of magnetic pulses to stimulate brain structures, Jacques d'Arsonval, a French physician, played a very important role. In 1893, d'Arsonval

applied high-frequency (circa 500 kHz) transient magnetic fields, using several types of coils, of different sizes, on human subjects. Three years later, in 1896, his work on non-invasive brain magnetic stimulation was published, where he reported some adverse effects after the stimulation protocol. The induction of flickering visual sensations (magnetophosphenes), vertigo and even syncope (loss of consciousness) were observed in human subjects that placed their heads inside the coil used by d'Arsonval. Such phenomena are described in detail further in this chapter and in Chapter 4. In the following years, several investigators continue the work of d'Arsonval focusing on the visual sensations evoked by magnetic stimulation of the brain (Vidal-Dourado et al., 2013). Barlow *et al.*, in 1947, demonstrated that magnetophosphenes were induced after selective magnetic stimulation of the retina rather than the occipital lobe as it was believed until then (Barlow et al., 1947). Using transient magnetic fields, Kolin *et al.*, in 1959, were the first to demonstrate that magnetic stimulation *per se* was able to evoke motor nerve response. Through the stimulation of a frog sciatic nerve, Kolin *et al.* induced *ex vivo* muscle contractions (Kolin et al., 1959).

The modern age of TMS began in 1976 with the work of Anthony Barker and colleagues at the University of Sheffield (see Figure 2.1). By 1985, Barker *et al.* developed the world first TMS device, capable of effectively stimulating the human motor cortex using only transient magnetic fields. TMS was described by Barker as a contactless and non-invasive new neurophysiological tool (Vidal-Dourado et al., 2013).

Thus, TMS appeared as an improved alternative solution of electrical stimulation, which, until then, was the only available procedure to achieve cortical stimulation. TMS was able to relieve the pain and discomfort caused by electrical stimulation and it allowed for more focal stimulation when compared with electrical stimulation, a technique with a broad activation area (Horvath et al., 2011).

In the field of diagnostics, the interest in TMS has been increasing among physicians since the replacement of transcranial electrical stimulation (TES), widely used in the late 1970s to measure motor conduction time (time taken for

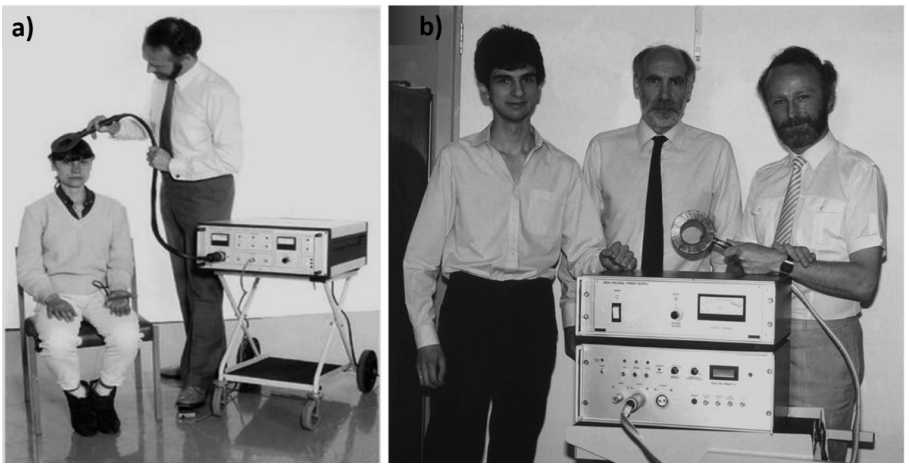

Figure 2.1: (a) Transcranial magnetic stimulation demonstration performed by Barker in London, 1985. **(b)** Reza Jalinous (left), Ian Freeston (middle) and Anthony Barker (right) exhibiting their TMS device in 1985. Adapted from (Vidal-Dourado et al., 2013).

neural impulses to travel from the central nervous system to the target muscles) in patients with multiple sclerosis. TMS then arose as a preferable solution since it allowed the same measures to be done in a much safer and painless way (Horvath et al., 2011). More recently, in the early 1990s and via the application of several consecutive TMS pulses, a protocol known as repetitive TMS (rTMS), Pascual-Leone *et al.* induced cortical effects and neural responses that remained after the cessation of stimulation over 3-4 min (Pascual-Leone et al., 1994). Hence, rTMS emerged as a very promising therapeutic tool due to its ability to induce lasting physiological and cognitive effects allowing for a more sustained intervention regarding the treatment of neurological and psychiatric diseases. This particular TMS sequence of pulses is thoroughly described in Section 2.5.

In spite of being increasingly used worldwide, both for clinical and academic purposes, the exact mechanisms behind TMS are still not fully understood. With this is mind, and as a neurophysiologic technique, TMS has been combined with some brain mapping methodologies (*e.g.* electroencephalography (EEG) and positron emission tomography (PET)), allowing for researchers to study the balance between excitation and inhibition of different brain regions, to better understand neuroplasticity [1] and perceive how different cortical and subcortical

[1]Neuroplasticity, also known as brain plasticity, refers to the brain ability to reorganise itself, forming new neural connections throughout life in order to compensate for injuries and/or diseases.

areas are connected with each other.

2.2 Electromagnetic induction: basic physical principles

The brain stimulation capability of TMS is based on Faraday electromagnetic induction principle (Faraday, 1832). In TMS, a high-intensity pulse of electrical current is applied through a coil placed near the patient head. Such current in the coil will, in turn, generate a transient magnetic field of typically 1-4 T (tesla) which penetrates the scalp and skull with almost no attenuation, leading to the induction of electric fields (E-fields) and associated currents in brain tissue (see Figure 2.2). This induced currents will depolarise neurons, producing different neurophysiological responses and behavioural changes according to the targeted brain region (Horvath et al., 2011, Wagner et al., 2007).

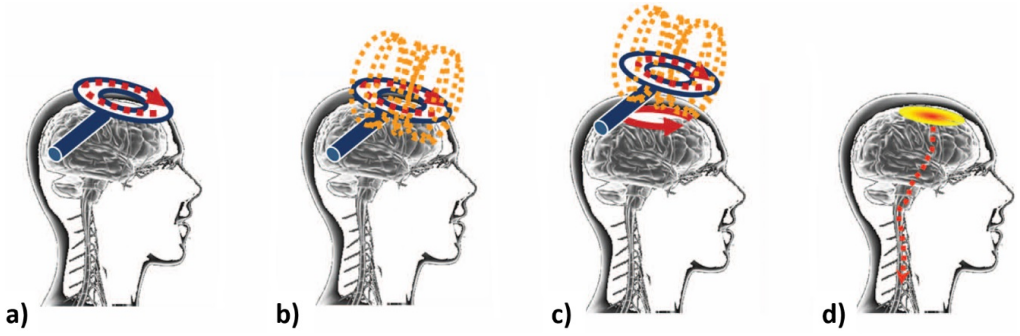

Figure 2.2: TMS underlying principle. **(a)** Transient electrical current flowing briefly in the coil.**(b)** Time-varying magnetic field generated in a perpendicular plane to that of the coil. **(c)** Secondary current induced in brain tissue, by the changing magnetic field, circulating in the opposite direction of the original current, in case such current is increasing. **(d)** Activation of cortical regions by means of depolarisation as a result of TMS. Adapted from (Vidal-Dourado et al., 2013).

The secondary ionic currents, induced in the neural tissue, flow in a parallel plane to that of the coil and in the opposite direction of the original increasing current, according to Lenz law. Heinrich Lenz, a Russian physicist, discovered that an electrical current, induced by a transient magnetic field, always circulates in such a direction that it will oppose the change which produced it. In this particular case,

the induced currents in the brain flow in the opposite direction of the current which generated the increasing magnetic field in the first place. Changing rates of this induced currents can go up to 170 A/μs (Najib et al., 2011). Hence, TMS is usually referred to as an "electrodeless electrical stimulation" of the brain, exploiting the principle of electromagnetic induction.

Next, the physical concepts underlying the TMS methodology are described.

2.2.1 Magnetic field and Lorentz force

Magnetic fields are induced by a wide range of equipments and materials that we use on a daily basis. Electric motors, microwave ovens, disk drives, computers, loudspeakers, all of them experience magnetic forces. Unlike electric forces, which act on electric charges, whether they are moving or not, magnetic forces only exert influence over moving charges. When two electric charges are at rest the only interaction between them is described by the electrostatic Coulomb force (see Eq. 2.1), where $\varepsilon_0 = 8.854 \cdot 10^{-12}\, C^2/Nm^2$ refers to the vacuum permittivity, q_1 and q_2 are the magnitudes of the two electric charges and r is the distance between them.

$$F = \frac{1}{4\pi\varepsilon_0}\frac{|q_1 q_2|}{r^2} \tag{2.1}$$

However, when the two charges are moving they experience and additional force due to the existence of the magnetic field. The magnetic force, $\vec{F}$, acting on a charged particle, q, moving with velocity $\vec{v}$, under the influence of a magnetic field, $\vec{B}$, is given by:

$$\vec{F} = q\vec{v} \times \vec{B} \tag{2.2}$$

from which, one can deduce the main features of $\vec{F}$. First, its magnitude is proportional to the magnitude of the moving charge and of $\vec{B}$. Second, and unlike the E-field force, the magnetic force depends on the particle velocity and does not have the same direction of the vector field, $\vec{B}$. Instead, the magnetic force $\vec{F}$ is perpendicular to the plane containing both $\vec{B}$ and $\vec{v}$ and the direction of $\vec{F}$ is given by the right-hand rule, considering a positive charged particle. If $q < 0$, the

direction of $\vec{F}$ is the opposite to that given by the right-hand rule (see Figure 2.3). Combining the electric and magnetic fields, the forces that the two fields exert on a charged moving particle are described as follows:

$$\vec{F} = q(\vec{E} + \vec{v} \times \vec{B}) \tag{2.3}$$

a relation commonly known as Lorentz Force law (Young et al., 2004).

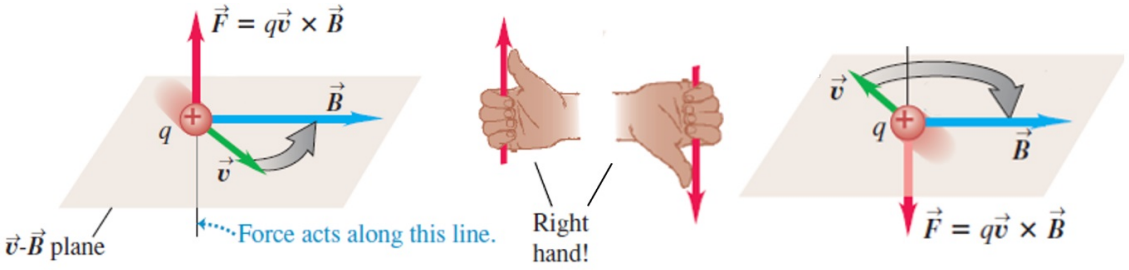

Figure 2.3: Right-hand rule used to find the direction of the magnetic force on a moving charge. Rotating $\vec{v}$ towards $\vec{B}$, the direction of the magnetic force is given by the right thumb, after one curls the remaining fingers of the right hand in the same direction as the rotation $\vec{v} \rightarrow \vec{B}$. Adapted from (Young et al., 2004).

Magnetic fields can be produced by a moving charge or a collection of moving charges (*i.e.* an electrical current) flowing in a conductor, as was discovered by Oersted, or they can be generated simply by a permanent magnet[2] (Jiles, 1998). A magnetic field can be defined in two forms: As magnetic flux density, B, expressed in tesla (T), or as magnetic field strength, H, expressed in ampere per meter (A/m). These quantities are related by $B = \mu H$, where μ is the magnetic permeability[3], which is constant in vacuum and air as well as in non-magnetic materials, such as biological tissue. In these cases, $\mu_0 = 4\pi \cdot 10^{-7}$, expressed in henry per meter (H/m). Since this work focus mainly on biological tissues, the magnetic field could be specified by any of the two quantities aforementioned (ICNIRP, 2010). Henceforth, throughout this work, the magnetic field (B-field) will be represented by $\vec{B}$.

Any B-field, $\vec{B}$, can be characterised by B-field lines (see Figure 2.4). A field line through any given point is tangent to $\vec{B}$ at that point. The more dense the field

[2]In a permanent magnet the magnetisation is caused by the orbital motions and spins of electrons within the material.

[3]Magnetic permeability reflects the ability of a material to respond to an applied magnetic field in which the material magnetises itself.

lines are, the stronger the field $\vec{B}$ is. Since $\vec{B}$ only has one particular direction at each point, B-field lines never intersect. These lines all form closed loops, so they do not have source or end points (Young et al., 2004).

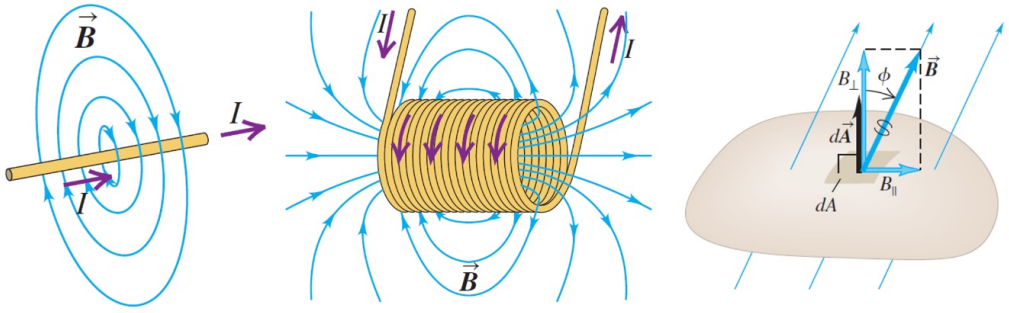

Figure 2.4: B-field of a current-carrying wire (left) and a current-carrying coil (middle). B-field lines are represented by blue lines and arrows. The current direction is indicated by purple arrows. Magnetic flux $d\Phi_B$ through an infinitesimal area element dA (right). Adapted from (Young et al., 2004).

From the number of B-field lines that cross through a surface with area A it is possible to define another useful concept, that is the magnetic flux Φ_B. This scalar quantity can be determined dividing the surface area into infinitesimal elements dA and for each one consider the component of $\vec{B}$ normal to the surface, at that position. Such component is equal to $B_\perp = B\cos\phi$, with ϕ being the angle between $\vec{B}$ and the vector $d\vec{A}$, normal to the surface and usually pointing outwards (see Figure 2.4). The total magnetic flux through a surface is the result of all the contributions of each element dA, and its SI unit is called the weber (Wb):

$$\Phi_B = \int d\Phi_B = \int B\cos\phi dA = \int \vec{B}\cdot d\vec{A} \tag{2.4}$$

Since B-field lines have no end (they form loops), the magnetic flux through a closed surface is always zero because every field line that goes in the surface has to come out, so the "amount" of B-field that enters and then leaves the closed surface is the same (Young et al., 2004).

Due to the electrical activity of all living cells within the human body, biological tissues have the ability to produce B-fields. Skeletal muscle fibres generate B-fields of less than 10^{-10} T, whereas brain cells produce weaker B-fields of about 10^{-12} T of magnitude. Comparatively speaking, the earth B-field has a magnitude of about 10^{-4} T, more than one million times stronger than those produced in our organism

(Young et al., 2004). Magnetic resonance imaging (MRI) scanners can now generate steady B-fields up to 9.4 T (Schmierer et al., 2010).

B-fields can be divided into two major groups. Static and time-varying B-fields. A static B-field remains constant over time and can be produced by permanent magnets or conducting coils with direct electrical current flowing through them. On the other hand, a transient electrical pulse applied through a wire coil generates a time-varying B-field, also known as AC B-field (Horvath et al., 2011).

Until this point, the influence of B-fields over moving charged particles has been analysed, always taking the existence of such fields for granted. But how are B-fields created?

2.2.2 Electromagnetic induction: Biot-Savart law and Faraday law

Biot-Savart law

As it was aforementioned, B-fields can be produced by current-carrying conductors. Biot and Savart defined a very elegant way to determine the B-field, $\vec{B}$, at any given point in space, produced by a current in a complete circuit. Considering a wire of an arbitrary form with a current I divided into infinitesimal segments $d\vec{l}$. The vector $d\vec{l}$, with length dl, has the same direction as the current I in the conductor. The distance between the B-field source $d\vec{l}$ and the field point,P, where $d\vec{B}$ is being calculated is given by r. Pointing from the source to the field point P is the unit vector $\hat{r}$ which has the same direction of the position vector of point P. Proportionality constant, $\mu_0/4\pi$, is equal to 10^{-7} T·m/A and μ_0 is the magnetic permeability of free space. The law of Biot-Savart can then be expressed as follows:

$$\vec{B} = \int_{AB} d\vec{B} = \frac{\mu_0}{4\pi} \int_{AB} \frac{I d\vec{l} \times \hat{r}}{r^2} \tag{2.5}$$

The total B-field is nothing more than the sum of the infinitesimal fields $d\vec{B}$ produced by each one of the segments $d\vec{l}$ of a current-carrying conductor of length AB.

A particular case of the Biot-Savart law is the B-field produced by a circular coil with N turns. Circular coils are perhaps the simplest example of a TMS-like induction coil. The total B-field measured at a point P located on the axis of the coil will be N times the field produced by a singular circular loop, assuming that such turns are closely placed so that the distance between the centre of each loop and the point P is approximately the same. A schematics of a single circular loop, with radius R can be seen in Figure 2.5.

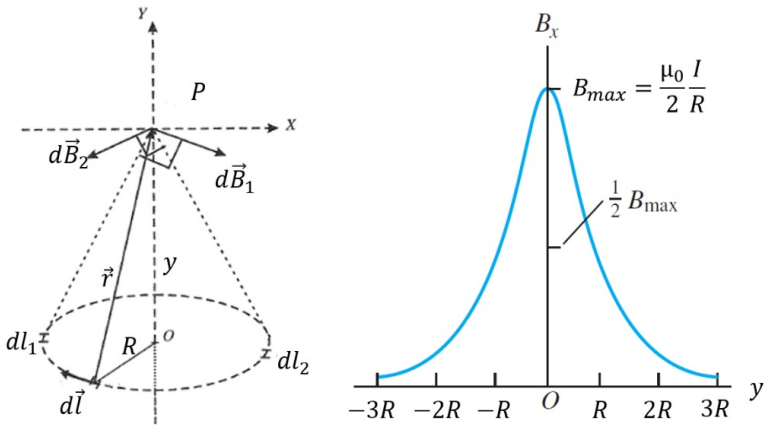

Figure 2.5: B-field on a point P on the axis of a circular loop. R is the radius of the loop and y the distance from P to the loop centre. On the right, the B-field along the axis of the coil as a function of y. At the centre of the loop ($y = 0$), $|\vec{B}|$ is maximum. Adapted from (Costa and Marques de Almeida, 2012) and (Young et al., 2004).

Considering the geometry of the problem, all the projections of $d\vec{B}$, at point P, perpendicular to the axis of the loop will be cancelled in pairs, since they are produced by diametrically opposed segments of the circular wire (such as $dl1$ and $dl2$). Additionally, the position vector $\vec{r}$ and the current element $d\vec{l}$ are perpendicular, so $d\vec{l} \times \hat{r} = dl$. Therefore, each current element contributes with:

$$|d\vec{B}_y| = \left(\frac{\mu_0}{4\pi}\frac{I}{r^2}\right)\cos\theta dl \tag{2.6}$$

being y the axis of the loop. θ represents the smaller angle between $d\vec{B}$ and the y axis which is equal to the angle between $\vec{r}$ and the plane of the loop. Knowing that $\cos\theta = R/r$ and $r^2 = R^2 + y^2$ it is quite simple to calculate the total B-field, $\vec{B}$, on the axis of a circular loop (Costa and Marques de Almeida, 2012). Integrating for

the whole perimeter of the loop:

$$|\vec{B}| = \int_0^{2\pi R} \frac{\mu_0}{4\pi} \frac{IR}{r^3} dl = \frac{\mu_0}{2} \frac{IR^2}{r^3} \tag{2.7}$$

If instead of a single circular loop, it is desirable to determine the total B-field due to a circular coil with N turns, one must simply multiply $\vec{B}$, obtained above in equation (2.7), by the number of turns N.

Faraday law of induction

Following Oersted work, Michael Faraday focused on the capability of a B-field to induce an electrical current on a nearby circuit. He observed that, whenever there was a variation of the B-field, due to the movement of a permanent magnet placed sideways to a coil, for example, an induced electrical current emerged in the circuit. This phenomenon is known as electromagnetic induction and it is a result of the variation of the magnetic flux Φ_B through a surface S delimited by the circuit.

Additionally, in order to induce and maintain an electrical current flowing through a circuit, an electromotive force $\varepsilon = RI$ is required. As the variation of Φ_B generates an induced current in the circuit, one can assume that the very same variation is responsible for the emergence of an electromotive force of induction ε_i. Hence, Faraday deduced the relation between the variation of Φ_B throughout time and the consequent electromotive force induction. The following expression translates such relation and it is widely known as Faraday law of induction:

$$\varepsilon_i = -\frac{d\Phi_B}{dt} \tag{2.8}$$

In the first place, it is important to realise that ε_i only appears as a result of a variation of the magnetic flux. If the flux Φ_B has a constant value over time, its time derivative is zero and therefore the magnetic flux by itself is not capable of inducing an electromotive force and thus neither an electrical current. Secondly, the negative sign implies the Lenz law, already defined in the beginning of Section 2.2. Basically, it means that the direction of the induced current is such that it will oppose the magnetic flux variation responsible for the appearance of that same current (Costa and Marques de Almeida, 2012).

Again, considering a coil with N turns and a transient current $i(t)$ flowing through it, a transient B-field is generated which in turn leads to a variation of the magnetic flux through the surface delimited by the coil. If the rate of change of Φ_B, $d\Phi_B/dt$, is approximately the same across all the turns, then, the total electromotive force induced in a coil with a time-varying current is N times greater than the one induced in a single turn. From Biot-Savart law it is possible to deduce that $|\vec{B}|$ is proportional to the varying current $i(t)$ passing through the coil. The magnetic flux is also proportional to $|\vec{B}|$ and therefore proportional to $i(t)$. The average magnetic flux, through each turn, can then be defined as follows:

$$\Phi_B = \frac{Li}{N} \tag{2.9}$$

where L refers to the self-inductance of the coil. Given that, Faraday law can be rewritten as:

$$\varepsilon_i = -N\frac{d\Phi_B}{dt} = -L\frac{di}{dt} \tag{2.10}$$

The SI unit of self-inductance is called the henry (H). One henry corresponds to the inductance of a coil which generates an electromotive force of 1 volt (V) when a changing current of 1 A/s flows through it (Costa and Marques de Almeida, 2012).

2.2.3 Eddy currents in brain tissue

As it was described by Faraday, an electrical current can be induced in a stationary conductor as a consequence of the variation of the magnetic flux across the conductor which generates an electromotive force ε_i. Assuming R as the resistance of the conductor, the induced current will be $I_i = \varepsilon_i/R$. Such movement of charged particles within a nearby, stationary conductor is due to an induced E-field, $\vec{E}_i$, produced not by electric charges but rather by a transient magnetic flux (Young et al., 2004). This E-field can be defined as follows:

$$\oint \vec{E} \cdot d\vec{l} = \varepsilon = -\frac{d\Phi_B}{dt} \tag{2.11}$$

In TMS, an E-field is induced in the brain tissue beneath the coil, exerting a force $\vec{F} = q\vec{E}$ on charged particles which in this case will be the ions existing in

the brain region that is being stimulated. Consequently, these free particles will start to move at a constant velocity in the direction of the E-field, constituting an electrical current (Miranda, 2013). Thus, TMS is capable of modulating neural activity, since these induced electrical currents circulating throughout the brain volume, known as eddy currents, will alter the transmembrane potential of neural cells inducing action potentials. These mechanisms will be addressed in detail further in Section 2.3. Eddy currents (see Figure 2.6) form closed loops and

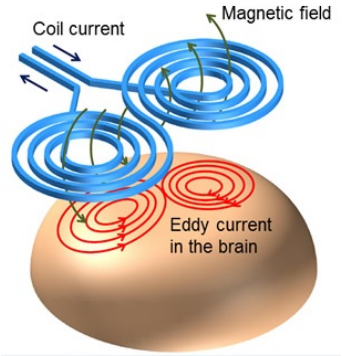

Figure 2.6: Eddy currents (red circular lines) induced in brain tissue by the time-varying B-field (green lines) created by a transient electrical current passing through a TMS figure-8 coil. Eddy currents flow perpendicular to the magnetic flux and in the opposite direction of the change of current in the coil. Adapted from (Sekino, 2011).

circulate within the conductive brain tissue in a perpendicular plane to that of the changing B-field. In compliance with Lenz law, eddy currents flow in the opposite direction relatively to the increasing current in the coil, thus producing a secondary B-field that opposes the variation of the magnetic flux that originated them in the first place.

It is believed, however, that eddy currents are more properly described when expressed as current density, $\vec{J}$. This physical quantity reflects the current that flows through a perpendicular surface in 1 second, divided by the cross sectional area, so the SI unit for current density is ampere per square meter (A/m^2). According to Ohm law, current density is proportional to the E-field, $\vec{E}$, and is given by:

$$\vec{J} = \sigma \vec{E} \tag{2.12}$$

The constant of proportionality, σ, is the electrical conductivity of the tissue and is expressed in siemens per meter (S/m). Current density is of vital importance for

the calculation of the E-field in the brain since the divergence of $\vec{J}$ is zero, meaning that the amount of charge reaching an infinitesimal volume in a given time interval is equal to the amount of charge leaving that same volume. Thus, the considered region is neither a source nor a sink of current (Miranda, 2013).

Along with relative permittivity [4], ε_r, the electrical conductivity describes the dielectric properties of tissues. Nonetheless, in TMS typical frequency range, up to 10 kHz, biological tissues can be considered mainly resistive, so the contribution depending on the permittivity can be neglected and the current density will almost solely depend on the tissue conductivity (Miranda, 2013).

Tissue heterogeneity and anisotropy have a major effect in the efficacy of TMS, particularly in the distribution of the E-fields. Head tissues have very different electrical conductivities which leads to a surface charge effect that will be discussed later in this work. Anisotropic tissues, like muscles, in which charged particles flow preferably in particular directions also influence the spatial distribution of the field $\vec{E}$ (Miranda, 2013). In Chapter 4 some results regarding the effect of tissue conductivity in the distribution of the induced currents in the brain are presented.

Currents induced by TMS normally flow in a parallel plane to that of the coil, so this stimulation methodology, unlike electrical stimulation of the brain cortex, is more likely to modulate nerve cells that are distributed horizontally relative to the brain surface (Horvath et al., 2011).

2.3 Inside the brain: physiological principles

The human nervous system is, beyond dispute, one of the most fascinating and complex of our organism. Through highly organised structures and networks, it allows the accomplishment of several sophisticated tasks like information processing, object recognition, communication, locomotion and development of cognitive processes like memory and learning so that it is possible for us to interact with each other and with the external world. From all the information that converges to the nervous system, it must be capable to interpret that

[4]Relative permittivity, also known as dielectric constant, corresponds to the material permittivity expressed as a ratio in respect to the permittivity of vacuum ($\varepsilon_r = \varepsilon/\varepsilon_0$). The permittivity reflects the force acting between two separate charges within the material.

information, retain what is truly important and emit a command order to effector muscles and/or glands to assure the human body adapts properly to its surroundings.

2.3.1 Structure and organisation of nervous system

Nervous system can be divided into two major categories: Central Nervous System (CNS) and Peripheral Nervous System (PNS). Organs responsible for information processing and integration like the brain and the spinal cord belong to CNS whereas the PNS keeps the connection between the CNS and the receptors/effectors via the sensory and motor neurons.

Additionally, the PNS still includes the somatic nervous system, associated with voluntary body control and the autonomic nervous system which controls the visceral functions of the body, namely, digestive processes, glandular secretions, breathing, cardiac muscle activity and even body temperature. The latter is further subdivided into subsystems, the sympathetic and parasympathetic which enable a suitable adaptation of the human body to everyday situations. The sympathetic system deals with emergency and stress situations keeping us watchful, whereas the parasympathetic system is associated with the daily maintenance of the body, mainly with the more relaxed and calm events.

In short, the PNS is responsible to carry information towards the CNS via sensory neurons (also called afferent neurons) and send the response signal through the motor neurons (also called efferent neurons) to the effectors (muscles or glands), allowing for human beings to change their inner environment in order to suit their needs (Brodal, 2010).

Nervous tissue: neurons and glial cells

This “closed-loop” system of sensation, decision and reaction, characteristic of the nervous system would not be possible without the building block of the nervous tissue, the neuron. These nerve cells are fundamental for the transmission of information along the brain and apart from some differences, all of them have, roughly, a similar structure. Neurons are comprised of a cell body, often called

soma, from which several processes emerge like multiple dendrites and a single axon. Dendrites form the receiving end of the neuron, collecting the stimuli from adjacent neurons or sense organs, originating a nerve impulse that travels to the soma and posteriorly to the axon. Lastly, the axon is a specialised structure in the fast conduction of the nerve impulse towards other neurons or effector organs (Mackay, 2009).

Nevertheless, neurons are not the most abundant cells in the brain, glial cells are, representing circa 90 % of the CNS total cells. They are of three kinds. First, the astrocytes which keep the neuronal environment optimal by controlling the concentration of ions and connecting neurons to capillaries. Second, the oligodendrocytes, responsible for the insulation of axons via production of myelin sheaths and finally the microglial cells that operate as a brain-specific immune system by detecting and eliminating any found pathogens. Glial cells are non-neuronal since they can not transmit an electrical impulse. They exist "only" for the support and protection of the neurons (Brodal, 2010).

2.3.2 Neural transmission

As previously mentioned, TMS stimulates neurons by the force exerted on the free moving charges existing in the intra- and extracellular environment of brain cells. Indeed, the nervous system makes use of membrane electric potentials like no other, exploiting the movement of ions across the cell membrane in order to propagate signals from one place of the body to another.

Resting membrane potential

Neurons can be considered as compartments in equilibrium with the extracellular environment, separated only by a semipermeable membrane. The neuron cell membrane, when in its resting state, only allows the diffusion of the K^+ ion, since it is almost impermeable to other ions (*e.g.* the permeability for K^+ is about 50 times grater than for Na^+).

However, in order for a potential difference through the cell membrane to exist, an ionic gradient must be generated between the intracellular and extracellular

fluids. Achieving such gradient requires energy that is released from the hydrolysis of adenosine triphosphate (ATP) molecules performed by an enzime located in the plasma membrane called Na^+/K^+-ATPase. This sodium-potassium pump moves 3 Na^+ ions outwards and 2 K^+ ions inwards for each ATP molecule hydrolysed. The need for energy comes from the active transport of these two ions against their concentration gradients.

As a result, the concentration gradients are established and maintained since the inside of the neuron has greater concentrations of K^+ and negative charged proteins (too large to permeate the membrane) and the outside of the nerve cell has increased concentrations of Na^+ and Cl^- ions (see Figure 2.7a).

Nevertheless, it is the diffusion of K^+ ions outwards the cell (according to its concentration gradient) that is the main responsible for the potential difference across the membrane since positive charges are being carried out, which leads to an excess of positive charge in the extracellular fluid.

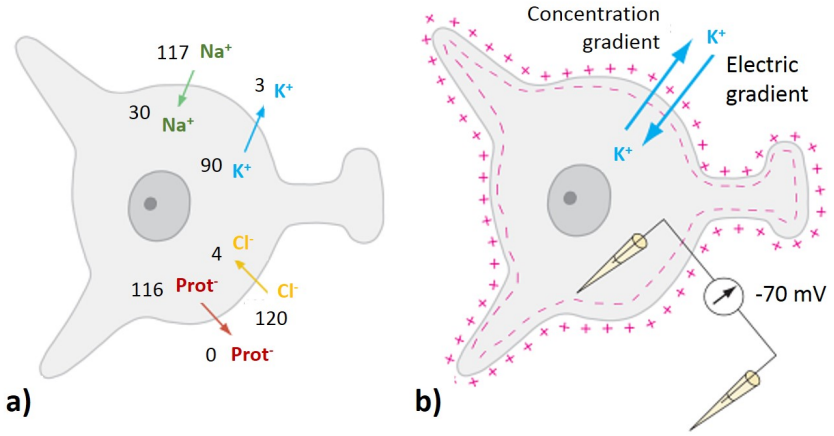

Figure 2.7: **(a)** Distribution of ions and their concentration gradients across the membrane. Concentrations in milimolar (mM). **(b)** Forces exerted on the K^+ ions. Resting potential is explained by the electric and concentration gradients (blue arrows) that balance each other. Two electrodes measure the membrane potential. Adapted from (Brodal, 2010).

Consequently, the efflux of K^+ is balanced by the build-up of negative charge on the inner surface of the membrane resulting in an equilibrium point, defined as the resting membrane potential which is of about -70 mV (may vary from -45 mV to -75 mV depending on the type of neuron), meaning that the neuron inside is at

a potential that is 70 mV less than the potential outside the neuron (Brodal, 2010, Mackay, 2009).

Nerve impulse: action potential

Information exchange across the nervous system requires the generation of nerve impulses that rely on an ionic permeability variation of the plasma membrane. The E-field induced in TMS depolarises the membrane which will lead to a gradual opening of voltage-gated Na^+ channels. When the membrane potential surpasses a certain value, the threshold potential of -55 to -50 mV, the probability of these ionic channels to be in an opened state remarkably rises and the permeability of the membrane for Na^+ ions increases significantly, leading to a large influx of Na^+ that overcomes the efflux of K^+. Both electric and concentration gradients contribute to this inward current of Na^+ that will, in turn, cause the opening of more voltage-gated channels. Consequently, the membrane potential rises up to 50 mV approximately, the membrane becomes depolarised and an action potential (AP) is produced. As depicted in Figure 2.8b, the

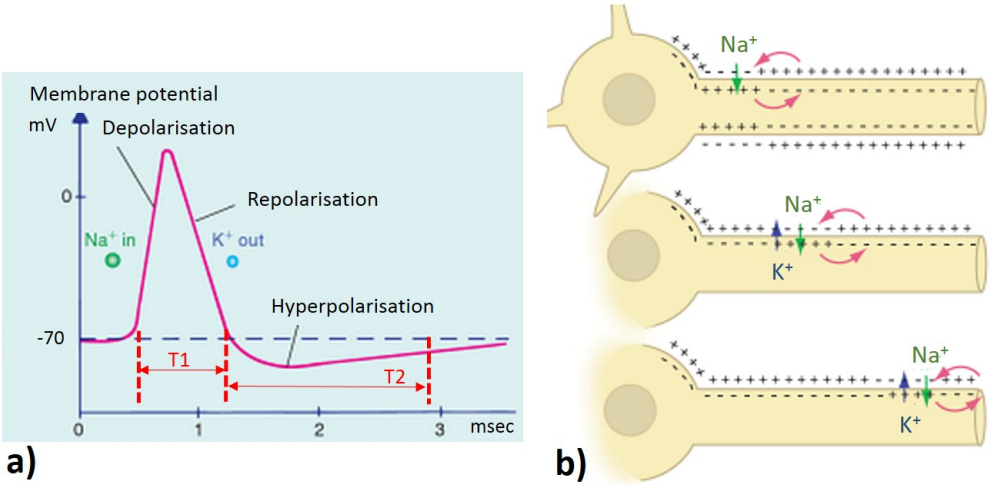

Figure 2.8: **(a)** Action potential. The absolute and relative refractory periods are represented by T1 and T2, respectively. **(b)** Nerve impulse conduction in unmyelinated axon. The membrane potential is being restored by continuous depolarisation-repolarisation processes. Adapted from (Brodal, 2010).

membrane does not remain depolarised forever. Immediately after the peak potential is attained, the Na^+ channels become inactivated and Na^+ ions are no longer capable of permeating the membrane. Such channels are not, however, the

only ones involved in the generation of the AP. Depolarisation also affects voltage-gated K^+ channels which alter the membrane permeability for the K^+ ions, but in a less significant way and more slowly than what happens for the Na^+ channels. This difference is thought to be a consequence of the density of the aforementioned channels since the number of Na^+ channels is about 10 times greater than the number of K^+ channels (Mackay, 2009).

Therefore, the repolarisation stage is characterised by the inactivation of Na^+ channels and the opening of K^+ channels, enabling the outflow of K^+ ions, driven by their electrochemical gradient. This sudden decrease of intracellular K^+ concentration leads to an undershoot phenomenon in the membrane potential, known as hyperpolarisation, that is promptly balanced, returning to its resting value due to an increased probability of the K^+ channels to be in a closed state (Brodal, 2010).

The AP generation is a very fast process, of the order of a few milliseconds, as seen in Figure 2.8a, and after each nerve impulse, a time interval must pass before the neuron is able to fire again. While the membrane is depolarised or in repolarisation stage, the Na^+ channels are inactivated which means that, no matter how strong the stimulus may be, those channels will remain closed and the neuron can not generate a second AP. This is called the absolute refractory period and approximately lasts 1 ms ($T1$ in Figure 2.8a). Thus, there is a physiological limit regarding the maximum stimuli frequency under which the neuron can respond (about 1000 pulses per second) (Brodal, 2010).

However, during the relative refractory period ($T2$ in Figure 2.8a), which is longer than the previous one, since it includes the hyperpolarisation phase, some of the Na^+ channels are no longer inactivated and can be opened by a stronger depolarisation that implies that a stronger stimulus is required (Brodal, 2010).

Nerve impulses are produced whenever the threshold potential is reached, regardless of the stimulus intensity or duration, reflecting the all-or-none principle. The AP normally arises in the initial segment of the axon, known as axon hillock, where the density of Na^+ channels is higher. The signal, then, propagates along the axon, in an unidirectional way because the refractory period prevents the

impulse from going backwards to the cell body. Additionally, in order to enable greater propagation velocities, some axons are insulated by a thin layer of myelin that allows for the AP to jump between gaps on the myelin covering, called nodes of Ranvier. Hence, in myelinated axons, the AP is only regenerated at each node of Ranvier rather than being continuously produced and slowly propagated along the axon membrane. When associated with larger diameters, propagation velocity can be of 30-170 m/s instead of the 3 m/s, obtained with unmyelinated axons (Brodal, 2010, Mackay, 2009). However, other structures of the neuron can act as activation spots, for instance, when the neuron is stimulated by a TMS-induced E-field which can lead to a depolarisation at a bend of a neuron or at the basal/apical dendrites of the neuron (Coop et al., 2010). In these situations bilateral impulse propagation can occur in which the AP is conveyed towards and away from the soma.

The locations where information is transmitted from one neuron to another are termed synapses. The signal propagation occurs at the synaptic cleft, a very narrow gap (20 nm) that exists between two adjacent neurons, where the neurotransmitters are liberated from the pre-synaptic neuron towards the post-synaptic membrane where an action potential is triggered (Brodal, 2010).

2.3.3 Rheobase

As aforementioned, the TMS-induced E-field affects the brain tissue by producing an action potential in excitable neuronal cells which might result in the activation of neuronal circuits, when it is applied above a certain threshold, E_{th}. The neuronal response, however, depends on the E-field intensity as well as on the pulse duration. As the pulse is extended in time, the E-field necessary to reach E_{th} becomes smaller. This dependence on the pulse duration is given by a strength-duration curve (see Figure 2.9) as follows:

$$E_{th} = \beta \left(1 + \frac{\gamma}{T}\right) \tag{2.13}$$

where E_{th} is the threshold E-field required to induce the neuronal response and T is the duration of the field that was above the threshold. The neuronal response is still

influenced by two biological parameters: the threshold at infinite duration, termed the rheobase, β, measured in V/m, and the duration at which the threshold is twice the rheobase, termed the chronaxie, γ, in milliseconds (Roth and Zangen, 2012). Both the rheobase and the chronaxie depend on several biological factors such as whether the nerve fibres are myelinated or not and on stimulation parameters like the train frequency in rTMS that usually reduces the stimulation threshold. If the stimulus magnitude is below the rheobase, regardless of its duration, the stimulation is ineffective since no AP is generated.

As previously discussed in Section 2.2.3, E-field is proportional to current density so the rheobase can also be defined in terms of a current density threshold. In fact, Kowalski *et al.* determined the current density threshold for the stimulation of the motor cortex in the human brain. Using both clinical data and technical specifications of the Magstim® Model 200 stimulator the authors calculated the solution using the finite element method on a head model comprised of four different tissues, scalp, skull, brain and ventricular system. Simulating a pulse of 2.44 kHz and 2843 A in the coil, a threshold current density

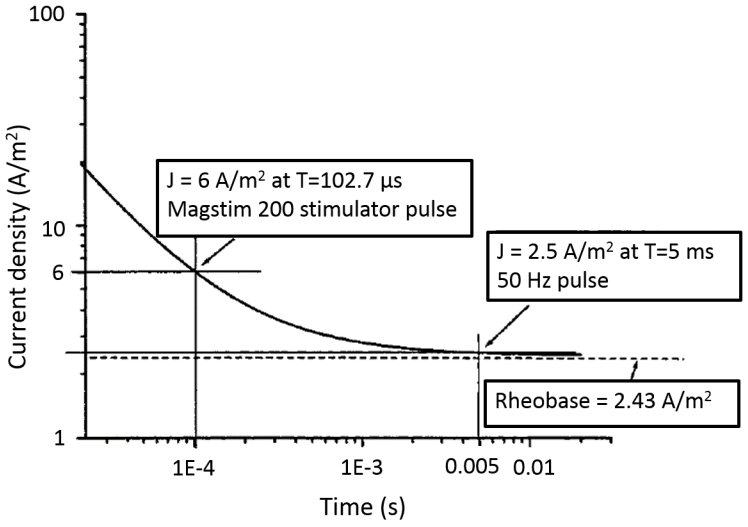

Figure 2.9: Strength-duration curve for the human motor cortex. After (Kowalski et al., 2002).

of 6 A/m^2 was calculated as the maximum current density for the stimulation of the motor cortex. Since it is not possible for the used stimulator to produce such strong pulses in the low frequency range of 50 Hz, a strength-duration curve was

used to interpolate the current density threshold required to stimulate the motor cortex through a B-field of 50 Hz. Considering a current density of 6 A/m^2 for a pulse with rise time of 102.7 μs (1/4 of the period at 2.44 kHz) and a time constant, γ, for the motor cortex of 150 μs, the rheobase is calculated to 2.43 A/m^2, according to Equation 2.13. For a 50 Hz pulse with rise time $T = T_{50Hz}/4 = 5$ ms, the threshold current density was estimated as 2.5 A/m^2 as seen in Figure 2.9 (Kowalski et al., 2002).

2.3.4 Long-term synaptic plasticity

The human CNS in order to compensate for functional brain impairments, due to ageing or brain lesions, or simply to adapt to environmental changes is able to modify its own organisation by altering the structure and function of synapses. This ability is defined as neuronal plasticity or synaptic plasticity (Berlucchi and Buchtel, 2008). This activity-dependent plasticity is believed to be the underlying mechanism of memory formation and learning, where synapses become more efficient. Such changes can last only a few minutes, short-term plasticity, or be more enduring, lasting weeks or even months, long-term plasticity (Brodal, 2010).

Long-term potentiation (LTP) and long-term depression (LTD) are the two most widely studied forms of synaptic plasticity. The first results in a lasting facilitation of synaptic transmission, whereas, the latter is characterised by a reduction of the synaptic strength. They are both input-specific, since changes can be induced at one set of synapses without influencing other synapses (Cooke and Bliss, 2006). Both LTP- and LTD-like changes can be induced in the human CNS via non-invasive stimulation techniques like rTMS. LTP can be induced by high-frequency trains of rTMS and low-frequency (1 Hz) rTMS is believed to induce LTD, since 1 Hz stimulation reduces synaptic activity (Bliss and Cooke, 2011).

With this in mind, rTMS protocols emerge as a powerful therapeutic tool for neurological conditions. They can be applied, for example, either for the reduction of cortical excitability (low-frequency rTMS) in epilepsy patients, or to induce increases in excitatory activity (high-frequency rTMS) in Parkinson sufferers. Subsequently, TMS stands as a preferable alternative to electrical

stimulation-based treatments that require invasive surgery (Bliss and Cooke, 2011).

TMS not only induces action potentials in neurons but also has the ability to alter the level of neural excitability during (online) and after (offline) stimulation by affecting membrane resting potentials, thresholds and synaptic connectivity. TMS offline effects result from an alteration of the long-term neural excitability after the stimulation. The underlying mechanism, however, is not yet fully understood. Current movement and polarisation of charge relative to brain structures and the interaction between the induced E-field and the ionic channels at the axonal boundaries are two hypothesis found in literature (Wagner et al., 2009).

2.4 State of the art: TMS hardware

2.4.1 Stimulators and coils

Magnetic stimulators are quite straightforward regarding its principal components. They consist of a charge-discharge system and a magnetic stimulating coil. These devices are comprised of one or more energy capacitors, charged by a high-voltage power supply, a discharge unit (TMS coil) and the required circuitry to control the pulse shape and the energy recovery.

An effective magnetic stimulator should be capable of achieving high peak coil energies and must be able to transfer the energy, stored in the capacitors, to the coil as quickly and efficiently as possible. Typical TMS stimulators can transfer about 500 J from the capacitor bank to the coil in a few hundreds of microseconds via an electrical switch (Horvath et al., 2011). In Figure 2.10 a typical TMS circuit is shown where low-voltage AC is transformed into high-voltage DC to charge the capacitor bank. The fast switch, typically a thyristor, is one of most important components since it is responsible for switching large currents over a very short time interval (50-250 μs) acting as the bridge between the capacitor and the coil. The TMS circuit is an RLC circuit, with a total resistance R, that translates the amount of energy dissipated as heat, a capacitance C that reflects how much energy

can be stored in the capacitor and finally, the inductance L related to the voltage required to change the current in the circuit, since $dI/dt = V/L$ (Roth and Zangen, 2012). After the capacitor is fully charged with the voltage V_C, all the energy is

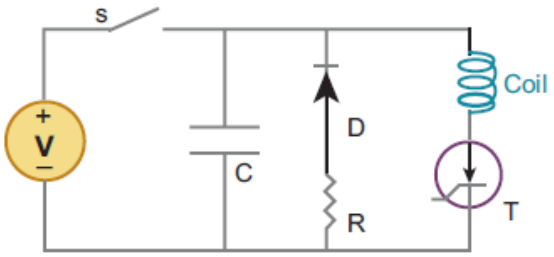

Figure 2.10: Single-pulse TMS device. Capacitor C is charged by the AC-DC transformer. The thyristor (T) allows for the capacitor to discharge through the coil L. The total resistance of the circuit is R and the diode D along with T guarantee that current only flows in the capacitor loop in the charging stage. Adapted from (Wagner et al., 2007).

stored in the capacitor and is given by:

$$W = \frac{1}{2}CV^2 \tag{2.14}$$

The thyristor then starts conducting, leading to the discharge of the capacitor, through the coil, until V_C decays to approximately zero. At this stage, energy is dissipated in R as heat, along the current loop formed by the coil L, the diode D and the thyristor. In the single-pulse system depicted in Figure 2.10 the current flows in a single direction (Roth and Zangen, 2012).

TMS circuitry must be able to generate high-current (2-10 kA) and very fast ($<$ 1 ms) pulses and deal with peak voltages ranging from 0.5 up to 3 kV. Additionally, common capacitance values can vary between 10 and 250 μF, whereas the coil inductance typically ranges from 10 to 30 μH. As for the resistance R, values between 20 and 80 $m\Omega$ are usually found in TMS devices.

Stimulating coils are made of wound copper wire, normally encapsulated in a moulded plastic cover. Commercial TMS coils typically have diameters ranging from 4-9 cm and 10 to 20 turns (Wagner et al., 2007). Both the geometry and design of the coil play a very important role in the effectiveness of the stimulation since the coil shape determines the induced current distribution as well as the strength

and focality of the brain stimulation (Rotenberg et al., 2014). In Figure 2.11 the most commonly used TMS coils are presented.

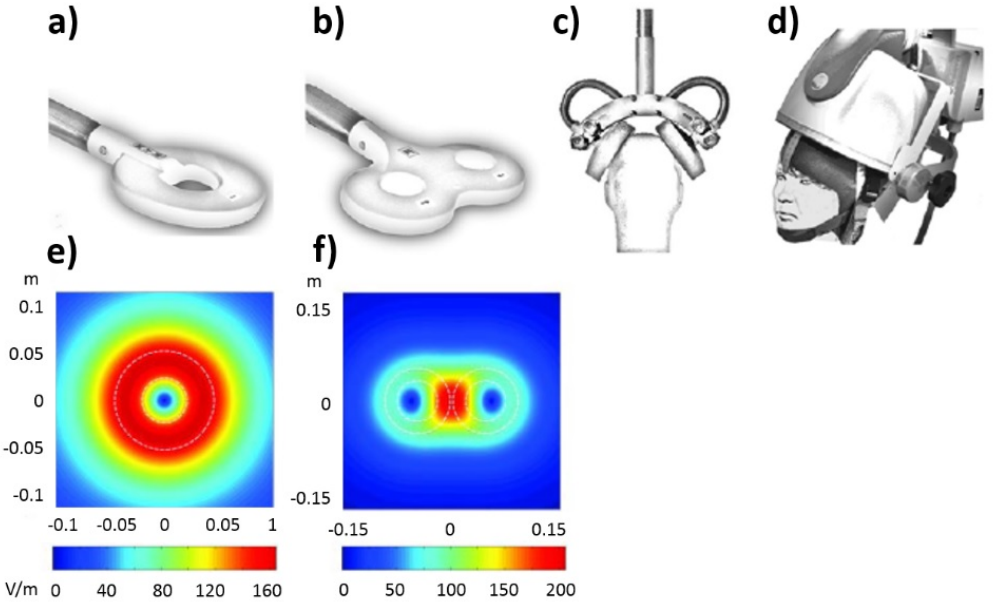

Figure 2.11: Schematic representations of four different types of TMS coils. **(a)** Circular coil. **(b)** Figure-8 coil. **(c)** Double-cone coil. **(d)** Hesed coil (H-coil). **(e)-(f)** Distribution of the induced E-field by a 6.65-cm radius circular coil and a 7.3-cm radius figure-8 coil. The E-field amplitude was calculated in a plane 2 cm below the coils. Adapted from (Rotenberg et al., 2014, Walsh and Pascual-Leone, 2003).

The single circular design was the first to be implemented in TMS devices where a spherical B-field perpendicular to the coil is generated. Such coil is mostly used in the application of single TMS pulses despite being less focal.

The figure-8 coil consists of two intersecting circular coils, allowing for a stronger B-field at the contact point between coils, relatively to the surroundings, enabling a more focal stimulation than circular coils. By means of mathematical modelling, this coil is believed to attain a spatial resolution of 5 mm^3 in the brain volume, although the induced E-fields are limited to the superficial cortical layers underneath the central part of the coil (Rotenberg et al., 2014).

The double-cone coil is formed by two adjacent circular coils separated by an angle of $95^{\underline{o}}$. That way the surface of both wings is tangential to the scalp which is a requirement for an effective stimulation since coil elements that are non-tangential to the head induce an accumulation of charge on the surface (Roth and Zangen, 2012). This surface charge produces an electrostatic E-field that reduces the total

E-field (electrostatic E-field and magnetically induced E-field) within the brain to 58 % of the value obtained when the coil is tangential to the head, so when there is no surface charge (Tofts and Branston, 1991). Comparatively to the figure-8 coil, the double-cone induces stronger and less focal E-fields and can be used for the stimulation of deep-brain regions, albeit some discomfort might be reported (Roth and Zangen, 2012).

Nevertheless, the state-of-the-art coil for deep-brain stimulation is the Hesed coil (H-coil) (see Figure 2.11d) that was developed to stimulate non-cortical layers of the human brain (Zangen et al., 2005). This more complex design will be addressed in detail in Section 2.6.

Despite the aforementioned examples, many other coil designs have been proposed or simulated as reported by Deng *et al.* who compared the E-field focality and attenuation in depth of 50 different coil designs (Deng et al., 2013*b*). The simulations were performed on a human head model with an 8.5 cm radius and isotropic conductivity of 0.33 S/m. Four different coil designs and respective induced E-field distributions are represented below in Figure 2.12.

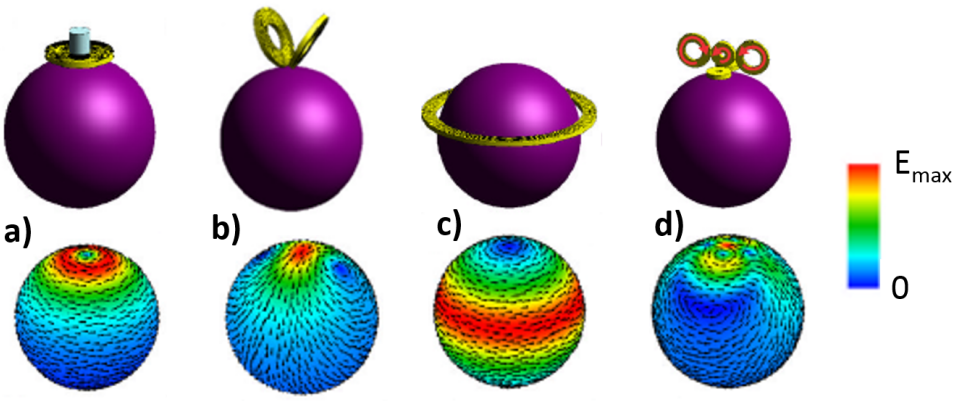

Figure 2.12: Different coil designs (upper row) and induced E-field distribution on the brain surface (lower row). The arrows indicate the E-field direction. **(a)** 5-cm radius circular coil with iron core. **(b)** 5-cm V-coil. **(c)** Supraorbital halo coil. **(d)** 3-D differential coil. Adapted from (Deng et al., 2013*b*).

In this study, the authors concluded that different geometries lead to different induced E-field characteristics and for all of them a depth-focality trade-off is verified. Meaning the stimulation of deeper structures requires higher E-field penetration, achieved at the expense of a reduced focality (Deng et al., 2013*b*).

When particularly used for rTMS, the overheating of the coil can become a limiting problem since several pulses are applied in short time intervals. To surpass such obstacle, coils are being constructed with an air or liquid cooling system or with magnetic cores (see Figure 2.12a) that serve as heat sinks reducing the heat generation and power consumption (Roth and Zangen, 2012).

2.4.2 TMS pulse: waveforms and strength

In this work, in order to maintain consistency, TMS pulses are, henceforth, classified according to the shape of the pulse that is induced in the brain tissue, rather than the current passing through the coil. The temporal variation of the E-field induced in the brain is determined by the rate of change of current in the coil, dI_L/dt, and as a result, this TMS-induced pulse was selected as classification criteria because it is the responsible for the direct stimulation of the neural tissue (Miranda, 2013).

Therefore, the TMS-induced pulse can be classified as monophasic, biphasic and triphasic (see Figure 2.13). The first results from a monophasic coil current, the second is produced by a "half-sine" current passing across the coil and the third is generated by a biphasic current flowing through the coil in which the pulse terminates after a full sinusoidal cycle (Sommer et al., 2006).

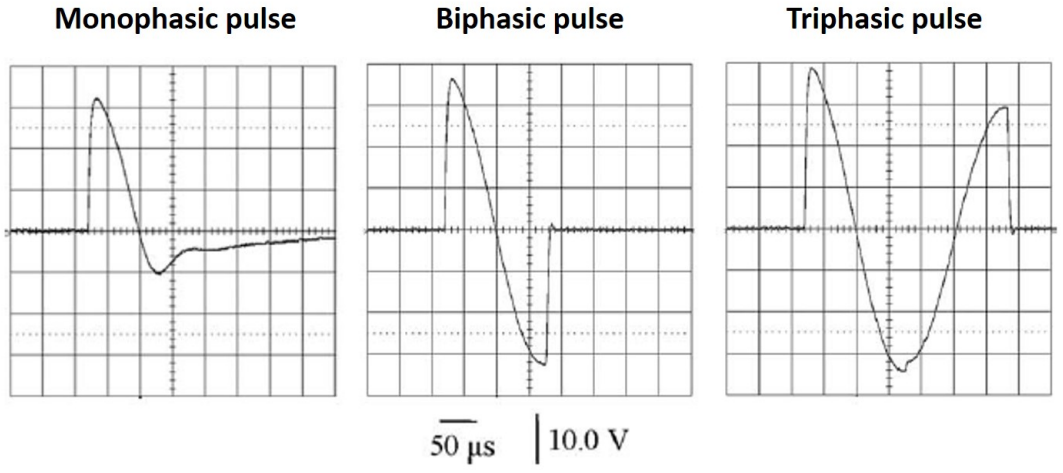

Figure 2.13: Current induced in a probe coil with 5 mm radius by a Magstim MagPro® stimulator in the monophasic mode (left), in the biphasic mode (middle) and in the triphasic mode (right). Adapted from (Sommer et al., 2006).

The first TMS stimulators were only capable of generating monophasic pulses, where, as represented in Figure 2.10, current flows in a single direction. After the peak of a monophasic pulse the energy is completely dissipated as heat, not returning to the capacitor and consequently, the stimulator is not capable of recharging (see Figure 2.14a).

Nevertheless, more recent TMS stimulators induce triphasic pulses, where the current is capable of flowing in both directions (Roth and Zangen, 2012). For this case, thyristor switching schemes are used to allow for part of the energy to be recovered in the capacitive charging unit (Wagner et al., 2007). Such TMS devices are the most widely used, since their ability to recover a great portion of the energy enables them to significantly reduce the capacitor charging time between pulses and also the power consumption.

Consequently, stimulators designed to produce triphasic pulses are well suited for rTMS, which demands a rapid recharging of the capacitor bank in order to achieve up to 100 Hz stimulation frequencies (Roth and Zangen, 2012, Wagner et al., 2007). As demonstrated in Figure 2.14, the variation of the transmembrane potential, V_m, during the application of a triphasic pulse is longer during the second phase, when hyperpolarisation occurs. Since neuron activation is only induced by depolarisation, the threshold to achieve such activation would be inferior if the current polarity was inverted because the depolarisation would last longer. This reflects the dependence of TMS effects, over the neural tissue, with the current polarity (Roth and Zangen, 2012).

Triphasic pulses are particularly advantageous for repetitive-pulse stimulators not only because of their energy efficiency but also because of their ability to induce currents in the brain with lower-intensity fields, meaning the threshold for neuronal activation is lower with triphasic than with monophasic pulses (Roth, Padberg and Zangen, 2007). The fast rise times in TMS pulses are crucial since neurons are not ideal capacitors and therefore, by inducing the E-field with faster pulses, less charge is allowed to escape from the neurons, attaining a more effective stimulation (Walsh and Pascual-Leone, 2003).

If the triphasic pulse is not terminated after a single sinusoidal cycle, another

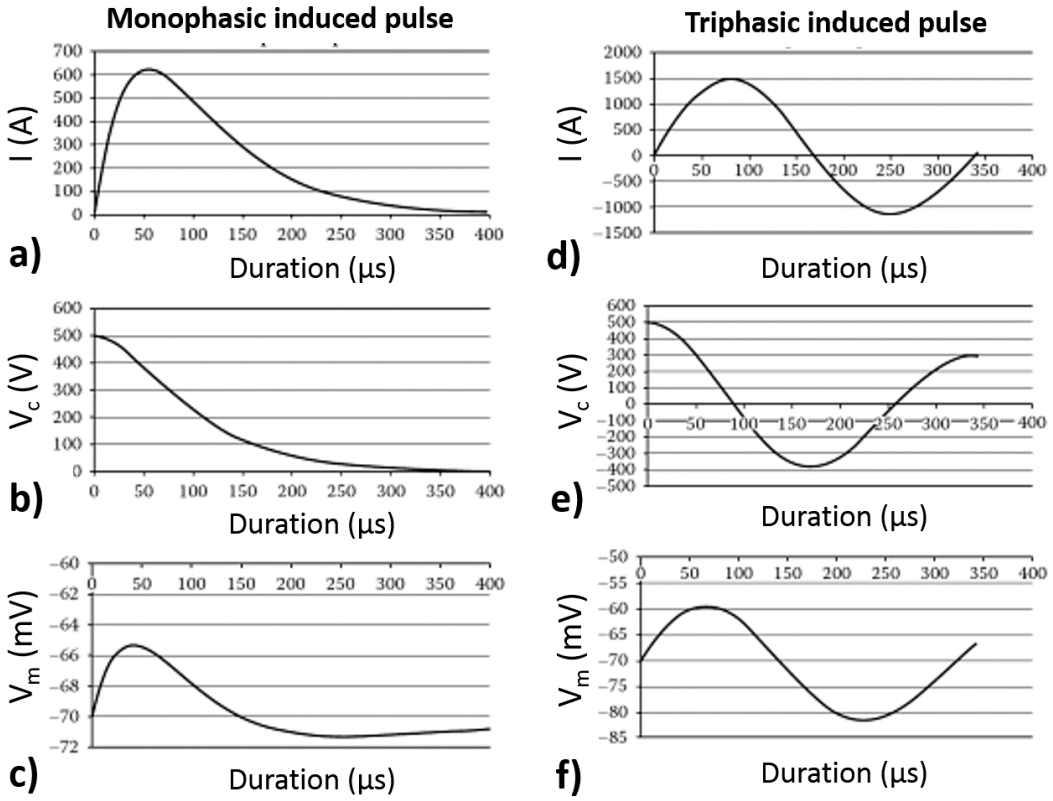

Figure 2.14: Monophasic **(a)-(c)** and triphasic **(d)-(f)** waveforms for a circuit with $C = 180\mu$ F , $L = 16\mu$ H and $R = 50m\Omega$. **(a)** Monophasic coil current. **(b)** Capacitor voltage V_C decaying to almost zero at the end of the pulse. **(c)** Membrane potential V_m. Only the first portion of the pulse induces significant depolarisation. **(d)** Biphasic coil current which induces a triphasic TMS pulse. **(e)** Capacitor voltage V_C switching between the two polarities. Almost 60 % of the voltage is recovered at the end of the pulse. **(f)** Membrane potential V_m reflecting depolarisation, at first and then hyperpolarisation. Adapted from (Roth and Zangen, 2012).

type of pulse, termed polyphasic, is produced (Rotenberg et al., 2014). Polyphasic pulse is hardly ever used because such waveform is much less suitable for TMS applications since the signal oscillates for many cycles having consecutively lower intensities. Therefore, at the end of the pulse, the energy is totally dissipated provided that it can not return to the capacitor and the second and following cycles are not as effective as the first one (Roth and Zangen, 2012).

Higher initial coil currents will lead to more intense stimulation and the amplitude can be regulated as needed. Regarding the pulse strength, it is normally indicated as a percentage of the maximum stimulator output (MSO) instead of an

absolute current value since the later will vary according to the type of coil used.

Intensity of TMS can also be expressed in terms of the patient motor threshold (MT), as a percentage as well (Rotenberg et al., 2014). The MT refers to the minimum stimulation intensity required to induce a motor response. It can be determined with the target muscle immobile (resting MT) or while the patient is performing a particular task involving the contraction of the target muscle (active MT) (Farzan, 2014). TMS sequences are usually calibrated for each individual MT since this threshold reflects the corticospinal excitability, which differs from patient to patient (Roth and Zangen, 2012).

Additionally, in some studies, the strength of the stimulation is expressed relatively to the individual phosphene threshold, defined as the minimum intensity required to evoke flashes of flickering light, on the subject visual field, in the absence of a visual stimulus (Thut et al., 2003).

Lastly, a new TMS near-rectangular pulse shape with controllable pulse width, known as cTMS, is gaining more and more attention. cTMS technology enables the adjustment of the pulse width, which is non-existent or very limited in standard TMS devices, that only allow for the control of the pulse amplitude. This induced near-rectangular E-field pulse reduces power consumption and coil heating while allowing for the optimisation of the pulse width for different neuronal populations. Therefore, cTMS technology has been improving the efficiency of TMS as a clinical and academic tool (Peterchev et al., 2008).

2.5 TMS protocols

By conjugating different pulse schemes and durations, TMS can be applied as an extremely flexible technique both for clinical and academic practices. In this section, some of the most well established TMS paradigms are described as well as their practical applications.

2.5.1 Single-pulse TMS

Single-pulse TMS (spTMS) consists of applying an unique, separated pulse on a pre-determined cortical area in order to assess cortical reaction. Thus, this protocol is mainly used for diagnostic and research purposes (Rotenberg et al., 2014).

Measure of the resting and active MT is done by means of spTMS, when applied to the primary motor cortex. The lowest pulse intensity to induce contralateral motor-evoked potentials (MEPs) of more than 50 μV in amplitude for muscles at rest or 200 μV for contracted muscles, in 5 out of 10 stimulations, is recorded by electromyography (EMG) and such measure yields important information about neurons located in the muscle representation of the motor cortex. MT is believed to express the excitability of the neuronal membrane and is lower for hand muscles when compared with lower limbs or muscles of the torso (Chen et al., 2008). Detecting and quantifying the latency of MEP can be of vital importance in diagnosing abnormalities of corticospinal tract conduction in pathologic conditions like multiple sclerosis where MEP can be absent or have lower amplitude (Currà et al., 2002).

Apart from the determination of the MT, spTMS can also be used to determine cortical activation threshold by evoking phosphenes when the primary visual cortex is stimulated. Furthermore, it is known that a single magnetic pulse is capable of interfering with functional occipital activity, namely visual perception, when applied during the period of visual suppression, 60-140 ms after the beginning of the visual stimulus. Thut *et al.* studied the effects of spTMS during the evolution of visual-evoked potentials (VEPs) recorded by EEG. Magnetic stimulation was delivered to the left occipital pole of 7 healthy subjects, using a Magstim® Super Rapid stimulator and a 7-cm figure-8 coil with a pulse width of 220 μs and intensity of 120 % of individual phosphene threshold (roughly 80 % of MSO). Authors found significant changes in VEP after TMS, reflecting the interference with functional activity due to an altered visual processing, in which spTMS effects occurred for at least 100 ms within the visual system (Thut et al., 2003).

Following Lipton *et al.* study on the effects of spTMS, the eNeura Spring TMS® portable device received, in 2013, the FDA approval for the treatment of migraine

with aura that is characterised by symptoms like tingling, numbness, regions of visual loss and weakness before the onset of headache. In this study, 164 patients treated at least one migraine attack either with spTMS or sham stimulation (see Section 2.5.4). The results shown that patients treated with spTMS had a much higher pain-free response after 2 hours, relatively to sham group and such absence of pain was sustained 24 hours and 48 hours after treatment (Lipton et al., 2010).

2.5.2 Paired-pulse TMS

The paired-pulse method (ppTMS) is based on the delivery of two isolated, consecutive pulses with variable inter-pulse intervals (IPIs), normally ranging from 1 to 100 ms. The two pulses do not necessarily have the same amplitude and can be applied over the same cortical target or over two different targets thus allowing the study of cortico-cortical connectivity. Normally, this ppTMS methodology evaluates the effects of the initial conditioning stimulus (CS) over the subsequent test stimulus (TS) (Rotenberg et al., 2014, Roth and Zangen, 2012).

The underlying mechanisms of cortical excitability and inhibition have been widely studied using ppTMS based methods. Being one of the first to use ppTMS to asses cortico-cortical inhibition, in 1993, Kujirai *et al.* stimulated 10 normal volunteers with a subthreshold CS, unable to evoke a MEP, followed by a suprathreshold TS, applied over the motor cortex at variable IPIs (Kujirai et al., 1993). The MEP induced by the TS was reduced at IPIs of 2-4 ms and enhanced at IPIs of 7 ms or longer. These phenomena became known as intracortical inhibition and facilitation, respectively (Currà et al., 2002).

Another method using ppTMS at short IPI (1-5 ms) consists of applying a suprathreshold CS followed by a subthreshold TS. This way, intracortical facilitation occurs and 3 MEP peaks are generated. If delivered at long IPI (100-200 ms) and both with suprathreshold intensity, the MEP induced by the TS is inhibited by mechanisms originated in the brain cortex. Finally, ppTMS also provides the ability to understand the connection between hemispheres since it is possible to stimulate one hemisphere with a CS and after an IPI of 5 to 6 ms apply the test pulse on the other hemisphere. The evoked response to this TS is inhibited by the previous

contralateral delivery of the CS. A subcortical pathway is believed to be involved in this inhibitory effect (Currà et al., 2002).

Hence, it is obvious that both the IPI and the stimuli intensity play a decisive role in protocols using the ppTMS sequence. Several neuropathologies, namely epilepsy and stroke, can benefit from methods using ppTMS as it provides new ways to develop a more personalised prognostic and therapeutic optimisation. Equally important is the possibility to combine ppTMS with EEG in order to evaluate TMS-evoked potentials in non-cortical regions. Subsequently, assessing facilitation/inhibition is no longer restricted to the motor cortex opening the window for new protocols with greater clinical value (Vahabzadeh-Hagh, 2014).

Concerning the equipment required for ppTMS, it is very similar to the one used by typical TMS studies, besides the need for two magnetic stimulators providing each one of them monophasic pulses. When the ppTMS must be applied to the same cortical target, the two stimulators must be connected by a BiStim Module from Magstim® allowing the two different outputs to be delivered by the same TMS coil (Vahabzadeh-Hagh, 2014).

2.5.3 Repetitive TMS

rTMS has been explored as a technique with great clinical potential in psychiatric conditions like schizophrenia, obsessive compulsive disorder, post-traumatic stress disorder (PTSD), epilepsy and major depressive disorder (MDD) (Fitzgerald et al., 2006).

As previously mentioned, rTMS is a unique methodology, that unlike spTMS and ppTMS, has the ability to modulate the neural tissue inducing long-lasting effects in the brain, either facilitative or suppressive. These effects can last several minutes after a single rTMS session or even weeks when consecutive sessions are applied. rTMS uses trains of sequential pulses delivered at a determined frequency that typically varies from 1 to 50 Hz. Low-frequency (1 Hz) rTMS (LF-rTMS) is normally applied in a continuous fashion along several minutes whereas high-frequency ($>$ 1 Hz) rTMS (HF-rTMS) is usually delivered in short bursts intercalated by intertrain intervals ranging from a few hundreds of milliseconds to

several seconds (Oberman, 2014). In Figure 2.15, a LF-rTMS protocol is shown along with a 20 Hz rTMS applied in bursts of 2 seconds.

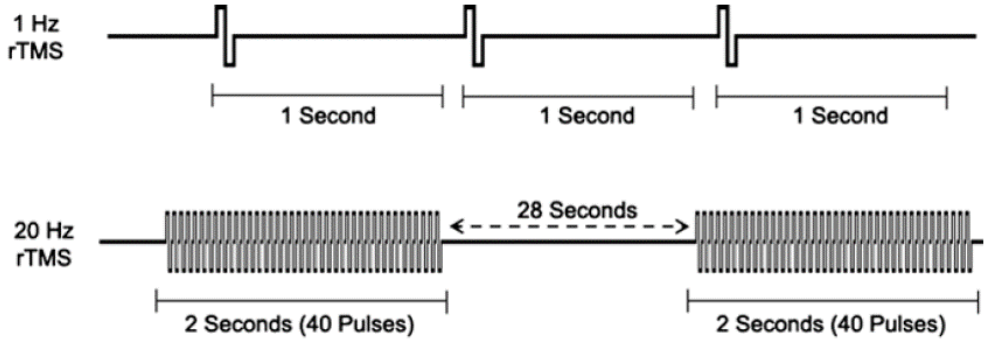

Figure 2.15: Schematic representations of two typical rTMS protocols. **(a)** Low-frequency (1 Hz) rTMS applied continuously. **(b)** High-frequency rTMS applied in 2-second bursts of 40 pulses (20 Hz) in an intermittent way (intertrain interval of 28 seconds). After (Oberman, 2014).

Two main parameters define whether rTMS will induce a facilitative or suppressive effect. First, the frequency of stimulation, reflected on the interpulse interval and second, the structure of the train related with the intertrain interval (Oberman, 2014). Through EMG-rTMS based studies it was shown that following 1-Hz rTMS to the primary motor cortex the MEP of a peripheral muscle is suppressed and the MEP of the same muscle is enhanced after a 20 Hz stimulation (Maeda et al., 2000). Notwithstanding, it is not correct to generalise such findings since the intertrain interval also plays a decisive role in the direction of the rTMS effect (facilitation or inhibition).

The strong influence of the intertrain interval is well evidenced by the contrary effects of two types of Theta Burst Stimulation (TBS), where short bursts of 3 pulses at 50 Hz separated by intervals of 200 ms are applied to the motor cortex (see Figure 2.16). If this TBS is delivered continuously, continuous TBS, a suppressive effect is attained that lasts for about 20 min, resulting in an LTD-like plasticity. Surprisingly, if the same frequency stimulation is applied intermittently, in 2-s bursts with 8-s intertrain interval, the neural activity is facilitated since spTMS-induced MEPs are enhanced during 30 min after TBS, thus occuring an LTP-like effect (Oberman, 2014).

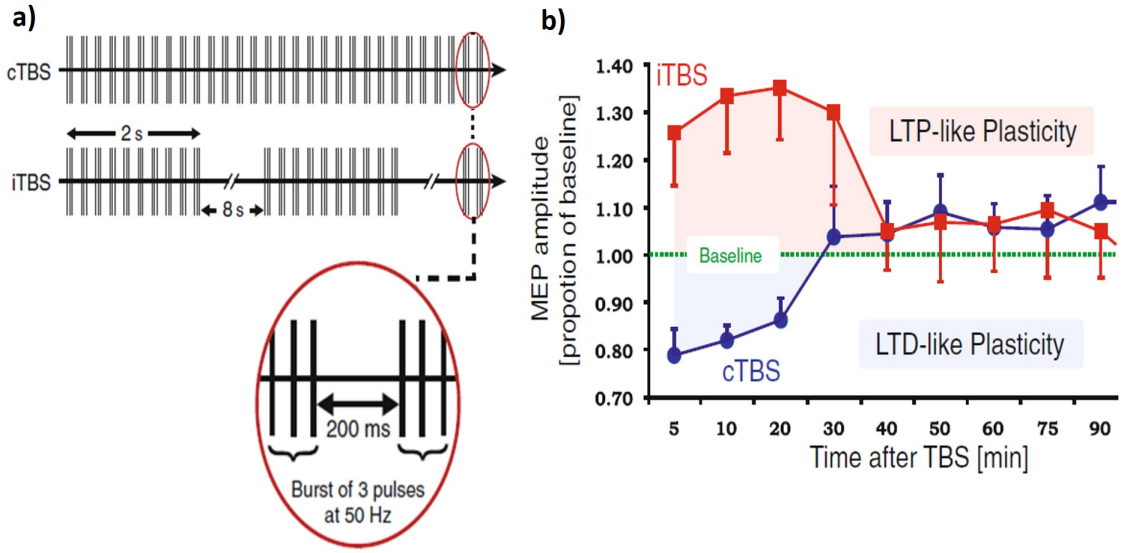

Figure 2.16: **(a)** Schematic representation of theta burst stimulation applied continuously (cTBS) or delivered through 2 s trains intercalated by an 8 s interval (iTBS). Bursts comprised of 3 pulses at 50 Hz. **(b)** After the TBS over the left primary motor cortex, spTMS-induced MEPs amplitude decreased after cTBS and increased after iTBS for a period of 20-30 min. Adapted from (Oberman et al., 2012).

Figure 2.16 shows a proper example of how two protocols using the same pulse frequency (50 Hz) lead to opposite effects, just by having different intertrain interval.

Furthermore, the efficacy of rTMS is not confined to the cortical region directly beneath the TMS coil since a secondary activation can occur at distant brain regions that somehow are interconnected with the stimulated area. Consequently, subcortical structures can also be affected which are usually functionally related to behaviour and emotions (Guse et al., 2010). This repetitive sequence seems to induce effects in the brain, particularly regarding the modification of cerebral blood flow, glucose metabolism and neuronal excitability.

It is also important to highlight the dependence of rTMS effects on the history of the synaptic activity because, for instance, if a HF-rTMS protocol is applied to a target region and then a 1-Hz rTMS is performed on the same region, the inhibitory effect of the later stimulation is enhanced. The opposite situation is also verified (Guse et al., 2010).

In summary, rTMS is capable of modulating cortical excitability, either increasing or decreasing it and such effects remain beyond the period of the

treatment, assuring the therapeutic potential of this technique (Bersani et al., 2013).

2.5.4 Sham stimulation

For the purpose of controlling any possible placebo effects of TMS, an alternative sham stimulation protocol was defined, which has become almost mandatory for every cognitive study and therapeutic application. Sham TMS is intended to mimic a true stimulation by inducing the same peripheral sensations as an effective TMS protocol, so that the subject is not capable to distinguish whether he is receiving a sham stimulation or not (Robertson et al., 2003). In order to do that, one of two methodologies are put into practice.

The first consists of lifting the TMS coil away from the subject head or just tilting it so that it is no longer tangential to the head. This way, the induced E-field strength decreases and the TMS pulse do not significantly stimulates the brain. For instance, just by lifting the coil 2 cm, the pulse strength falls to about one third or less (Ruohonen and Ilmoniemi, 2005). However, this method is found to be less efficient since in some cases it might produce real TMS-like effects on the brain (Robertson et al., 2003).

A more convenient approach makes use of a specific placebo coil, designed for this purpose, comprised of two separated coils in which the current can be switched. When the direction of the current in the coils is opposite, a typical figure-8 coil TMS pulse is produced. If the direction is the same, the B-fields generated will cancel each other, below the coil, delivering placebo stimulation. Since the stimulator discharges in both cases, a loud clicking noise is also produced in the sham protocol and the scalp sensations experienced by the subject would be very similar to normal TMS (Ruohonen and Ilmoniemi, 2005).

2.5.5 TMS safety concerns

Despite being widely recognised as a safe technique, TMS, since its first use in 1985, has been associated with some adverse events. Safe-use recommendations and precautions were established for both clinical and academic TMS.

While exploiting the properties of electromagnetic induction, TMS protocols may induce potentially significant voltages in any type of wires or electronic devices such as cochlear implants and deep brain stimulation systems implanted in brain tissue. This can damage the internal circuitry of such devices leading to malfunction or even complete break down. In addition, the TMS generated B-field can interact with implanted medical devices like aneurysm clips, sensitive to B-fields, potentially causing the movement and or demagnetisation of the devices (Najib and Horvath, 2014). So, subjects with implanted metal and/or electronic devices should not be stimulated by TMS systems, unless the risk/benefit ratio justifies such practice. Nevertheless, TMS holds no risk when applied to individuals with cardiac pacemakers or spinal cord stimulators, the latter used for chronic pain treatment. This peripheral devices shall remain fully functional upon the application of TMS as long as the activation of the TMS coil does not occur near the mentioned equipments.

Brain tissue heating must also be taken into account, particularly when TMS is to be applied next to electrodes or brain implants, since the induction of eddy currents in these conductive materials can cause them to heat up potentially leading to skin burns. Nonetheless, a single TMS pulse is estimated to be only capable of provoking tissue heating of less than 0.1°C. It is, therefore, recommended that *ex vivo* measurements are performed with the proper stimulation parameters before applying the TMS protocol (Rossi et al., 2009).

2.5.6 TMS side effects

Regarding TMS side effects, a classification can be done based on the probability of a particular side effect to occur. More common side effects include headache, neck pain and temporary hearing loss whereas events such as induction of seizures and syncope are much more rare.

Headache and neck pain are the most commonly reported side effects, affecting 20-40 % of subjects undergoing TMS and are related to muscle tension which can be caused either by the stimulation itself or by the steady posture assumed by the patient throughout the TMS protocol. Pain intensity differs from patient to

patient due to individual susceptibility and it is dependent on the coil design and the stimulation location, frequency and intensity (Loo et al., 2008).

When the TMS coil is activated it undergoes a rapid mechanical deformation as a result of the high current flowing through it. This produces a loud clicking noise that may reach 140 dB of sound pressure level which exceeds the auditory safety levels recommended by OSHA (Occupational Safety and Health Administration) of 90 dB for an 8-hour day (Counter and Borg, 1992, Rossi et al., 2009). One case has been reported where a single individual experienced a permanent shift in its auditory threshold after being stimulated with an H-coil without wearing ear plugs (Zangen et al., 2005). In order to prevent an increase in auditory threshold, meaning hearing loss, it is recommended that both patients and operators wear earplugs during the application of TMS.

Table 2.1 points out the different probabilities of TMS side effects according to the stimulation protocol.

Table 2.1: TMS side effects for different protocols. LF: Low Frequency. HF: High Frequency. Adapted from (Najib and Horvath, 2014)

Side effect	**Single-pulse**	**LF-rTMS**	**HF-rTMS**
Headache/neck pain	Possible/rare	20-40 %	20-40 %
Hearing loss	Possible	Possible	Possible
Seizure induction	Rare	Rare	<1 % in healthy subjects
Syncope	Possible as epiphenomenon	Possible as epiphenomenon	Possible as epiphenomenon

In spite of having a much lower incidence, the induction of seizures following TMS is, undoubtedly, the most severe acute adverse effect of such stimulation. Seizures are more likely to be induced by high-frequency rTMS. A conservative estimate sets the risk of seizure at 1 in 1000 applications. Nonetheless a careful methodology must be applied taking into account the maximum stimulation frequency and intensity in order to avoid seizures. Such biological phenomena is caused by highly synchronised discharges of groups of neurons due to a facilitation of excitatory synaptic activity over the inhibitory one. Avoiding such events may

be possible if TMS protocols are applied accordingly to established safety guidelines. Wasserman *et al.*, in 1998, defined a combination of rTMS parameters such as frequency, intensity and duration of trains that should guarantee patients safety (Wassermann, 1998). More recently, Rossi *et al.* published four reported cases of seizures following rTMS and single-pulsed TMS protocols applied with parameters within Wasserman safety guidelines. Nonetheless, three of these four instances of seizures occured in patients taking pro-epileptogenic medications [5] that might have increased the risk of seizure (Rossi et al., 2009).

Another relevant side effect is syncope during the stimulation protocol which can occur due to anxiety and or physical/psychological discomfort in addition to stimulation itself. This fainting events during TMS have been reported even less frequently than seizures as shown in Table 2.1. This effect is regarded as an epiphenomenon, indirectly related to the TMS procedure, being a secondary symptom of the stimulation. Defining it as a TMS side effect must be done with caution realizing the difference between syncope and other direct side effects (*e.g.* seizure induction). Syncopal episodes could be difficult to distinguish from epileptic seizures, so all subjects undergoing TMS must be monitored for any signs related to syncope (*e.g.* dizziness, faint feelings). In the event of syncope and/or seizure, stimulation procedure should be stopped immediately and medical care should be provided (Najib and Horvath, 2014).

2.6 Deep-brain TMS

As seen in Section 2.2.2, the coil-induced B-field decreases exponentially with the distance from the original current. Consequently, the eddy currents in the brain tissue will also drop very quickly towards the brain centre, since the induced E-field also falls dramatically as the distance from the coil surface increases (Maccabee et al., 1990, Tofts and Branston, 1991). Therefore, commonly used TMS coils such as the circular or the figure-8 coil are limited to the superficial layers of the brain cortex, typically 2-3 cm in depth (Deng et al., 2013*a*). Using such coils to effectively

[5] Medications with epileptogenic potential include antidepressants, antipsychotics for the treatment of schizophrenia and analgesics.

stimulate deeper brain regions would imply very high intensities of electrical current which in turn would also stimulate cortical structures and facial nerves potentially causing contraction of facial and cervical muscles leading to discomfort or even pain (Roth, Padberg and Zangen, 2007). The excess of electric charges on the cortical surface, in this hypothetical situation, would also increase the risk of seizure induction (Bersani et al., 2013).

The challenge to activate deep located regions arises from both physical and physiological limitations, namely the induction of an E-field capable of penetrating several centimetres across the brain tissue without overstimulating the more superficial layers. Heller and van Hulsteyn theoretically proved that it is not possible, under any circumstances, to induce a three-dimensional local maximum of the E-field inside the brain. Such maximum will always occur at the brain surface, where the electrical conductivity experiences a significant variation (Heller and van Hulsteyn, 1992). However, new coils and stimulators have been proposed to overcome part of the limitations inherent to deep TMS (dTMS) by attempting to increase the penetration depth and the percentage of E-field intensity in deep-brain areas relatively to the maximum E-field at the surface (Roth, Padberg and Zangen, 2007).

2.6.1 dTMS coils: reaching deep-brain regions

Compared with a standard figure-8 coil, the double-cone coil (Figure 2.11c) is capable of achieving deeper brain structures although it induces a less focal E-field (Deng et al., 2013*a*). The very strong fields produced by this coil decay rather fast with depth and reaching deeper regions involves the induction of much higher fields in cortical areas and facial muscles leading to painful stimulations (Zangen et al., 2005). Yet, double-cone coils have been used for the activation of the pelvic floor[6] and the induction of seizures in magnetic seizure therapy[7] (Deng et al., 2013*a*).

[6]Pelvic floor refers to the muscular base of the abdomen, attached to the pelvis.

[7]Magnetic seizure therapy is a side-effects-free alternative to electroconvulsive therapy for the treatment of depression.

Nevertheless, when it comes to stimulate deep neuronal structures, a family of coils, termed H-coils, has been providing the most promising results.

As it was mentioned before, the neuronal response depends on the E-field intensity, duration but also on the orientation of the induced field, since when the field is aligned with the nerve fibre, the stimulation is more efficient. Therefore, each H-coil coil must be constructed accordingly to the location and size of the deep-brain region(s) of interest in order to produce a significant E-field with the desired orientation(s) to stimulate the neurons under consideration (Zangen et al., 2005).

Regardless of each specific shape, all dTMS coils must follow some basic principles to attain a successful deep-brain stimulation. Firstly, the total induced field must be obtained through the summation of several E-fields produced by each coil element in different brain regions and the non-tangential elements of the coil should be minimised to reduce accumulation of surface charge, particularly around the target region. Secondly, the coil must be flexible providing proper attachment to the patient head and must be oriented in such a way that it will generate an E-field in the optimal stimulation direction. Finally, the return paths (wires leading current in the opposite direction) should be placed as far as possible from the base of the coil and from the brain region to be stimulated to avoid reducing the induced E-field (Roth and Zangen, 2014*a*).

In Figure 2.17 a schematic representation of the H-coil is presented along with the comparison of the E-field profile of five different coils, measured along a line, from the coil surface towards the centre of a phantom head model, filled with saline solution (Roth and Zangen, 2014*a*).

From the plot it is possible to conclude that the H-coil is the most suited for reaching higher depths since at 4 cm from the coil, the E-field suffered an attenuation to 66 % of the E-field measured at 1 cm distance. At the same distance, for the large circular coil, the E-field was attenuated to 52 % and for the remaining coils a stronger field attenuation with depth was observed, to values ranging from 29 to 37 %. Even at only 2 cm deep, the slower rate of field decay of the H-coil is already visible, which allows the activation of deep structures without a much higher

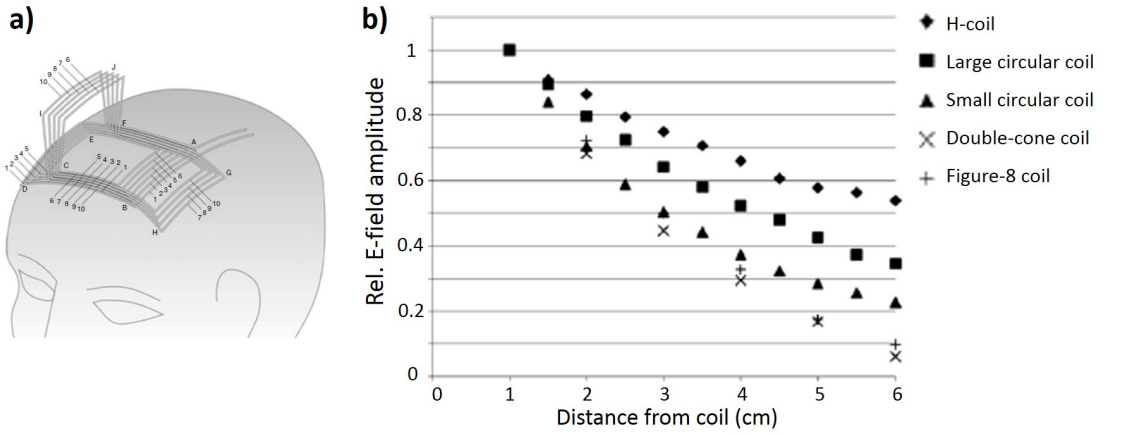

Figure 2.17: **(a)** Schematic representation of the H-coil version used for this comparison. **(b)** E-field amplitude relative to the amplitude at 1 cm from coil surface as a function of distance from the coil. Coils used: H-coil version in **(a)**, 16-cm and 5.5-cm diameter circular coils, 7-cm figure-8 coil and a double-cone coil with 12-cm diameter wings. Adapted from (Roth and Zangen, 2014*a*).

stimulation of cortical regions, although superficial layers close to the coil and above the target deep region will always be stimulated (Roth and Zangen, 2014*a*, Zangen et al., 2005).

The H1 coil, the HLRINS coil, the HAC coil and the H2 coil are four other examples of H-coils (see Figure 2.18). The first has been widely used in clinical trials and already received FDA approval of Deep TMS device, in 2008, for the treatment of drug resistant MDD patients in the USA. Its particular design is intended to target structures located on the left and right lateral and medial prefrontal cortex, preferentially in the anterior-posterior direction of the left hemisphere (Levkovitz et al., 2007). The HLRINS coil, used in clinical studies worldwide, focus on the stimulation of bilaterally neuronal structures on the insular and entorhinal cortex, regions involved in empathy, compassion and memory formation and expression (Izquierdo et al., 1997, Lamm and Singer, 2010, Roth and Zangen, 2014*a*).

The HAC coil is used to activate medial frontal neuronal regions like the anterior cingulate cortex, which is believed to be involved in the regulation of cognitive and emotional processing (Bush et al., 2000, Roth and Zangen, 2014*a*). The principal coil elements are divided into two groups and placed above medial brain regions whereas the return paths are located laterally on both sides of the coil (Roth and Zangen, 2014*a*). Lastly, the H2 coil was designed to stimulate prefrontal regions

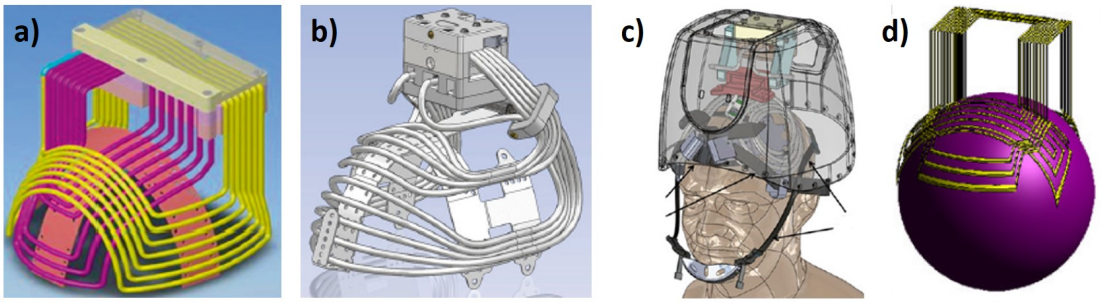

Figure 2.18: Schematic representations of **(a)** the H1 coil , **(b)** the HLRINS coil, **(c)** the HAC coil encased in a typical helmet, positioned over a human head and **(d)** the H2 coil. Adapted from (Deng et al., 2013*b*, Roth and Zangen, 2014*a*).

bilaterally, since the coil elements are oriented in a right-left direction (Levkovitz et al., 2007).

Levkovitz *et al.* published the first study to assess the safety of dTMS, namely by means of the H1 and H2 coils. From 32 healthy subjects, who received dTMS stimulation, figure-8 coil stimulation or sham stimulation, there were no reports concerning adverse physical or neurological outcomes. The H-coils stimulation was well tolerated, and no cognitive impairments were found, neither emotional or mood alterations, thus validating the feasibility and safety of dTMS (Levkovitz et al., 2007). However, more recent studies have reported some side effects, with patients reporting scalp discomfort, migraine, two subjects experiencing insomnia, one patient reporting numbness in the right temporal and right cervical region and three more patients suffering a brief seizure during treatment, although the latter were under high doses of antidepressive drugs that increase the risk of seizure (Bersani et al., 2013).

In conclusion, H-coils are able to effectively stimulate deeply located brain regions (up to 6 cm in depth) without causing pain or discomfort to the patient, at least for the vast majority of cases, since there is no need to induce undesired high field intensities in cortical regions. Nevertheless, this improved penetration depth is achieved at the expense of a reduced focality resulting in a wider E-field distribution along the brain (Roth, Padberg and Zangen, 2007). With H-coils it is possible to simultaneously stimulate several brain regions, controlling the penetration depth in each of them by adjusting the stimulator output and the distance between the coil and the scalp (Roth, Amir, Levkovitz and Zangen, 2007).

Typically and unless stated otherwise, dTMS refers to a repetitive rate stimulation protocol, like rTMS, but intended to stimulate deeply located brain structures.

2.7 Potential applications of deep-brain TMS

dTMS technology has been continuously improved and a significant part of this motivation most certainly comes from the several therapeutic targets located deeply inside the brain that, once activated, help improving symptoms and the overall quality of life of patients suffering from neurological and psychiatric conditions. dTMS is FDA approved for the treatment of pharmacoresistant MDD and several studies have been and still are in progress to assess the efficacy of dTMS in treating conditions like bipolar depression, PTSD, neuropathic pain, schizophrenia, Alzheimer disease and Parkinson disease (Bersani et al., 2013).

Next, some practical putative applications of dTMS protocols are described.

2.7.1 Major depressive disorder

Major depressive disorder also known as clinical depression or unipolar depression is a medical condition related to emotions of sadness and loss that remains long after the causes of these emotions disappear, being also disproportionate to those same causes. Diagnosis of MDD is based on changes of mood along with sadness, irritability and psychophysiological changes like sleep disturbance, loss of appetite, suicidal thoughts and incapability to experience pleasure in work or with friends/family (Belmaker and Agam, 2008). MDD is a common disorder affecting over 350 million people worldwide with a prevalence of 7 % of the European population suffering from MDD each year, according to the World Health Organization (World Health Organization Regional Office for Europe, 2012).

MDD is the psychiatric condition for which dTMS techniques have proven to be more efficient, particularly for patients resistant to antidepressant medication. Neuroimaging studies enabled the identification of the brain regions more involved in the regulation of mood states and emotional behaviour. Such regions belong to

the prefrontal cortex (PFC) or are, somehow, connected to it and include the dorsolateral (dlPFC) and dorsomedial (dmPFC) prefrontal cortices, amygdala, hippocampus and the nucleus accumbens. Several studies using rTMS achieved the most promising results via an excitatory stimulation of the left dlPFC, region characterised by reduced metabolism and blood flow in MDD patients. Another system closely related to the pathophysiology of MDD is the reward circuit comprised of deeply located structures like the nucleus accumbens and the ventral tegmentum area (see Figure 2.19), both related to the dlPFC and vlPFC regions, that contribute to the symptomatology of depression (Bersani et al., 2013). To directly stimulate deeper structures like the reward pathways, standard TMS coils are not suitable and dTMS is a safety and effective alternative .

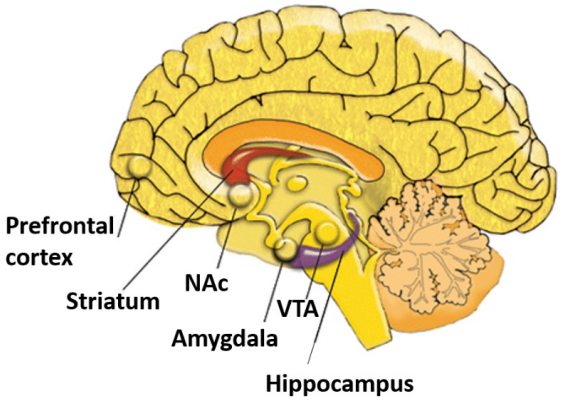

Figure 2.19: Location of several brain regions included in the reward-related pathways that are involved in the pathophysiology of depression. VTA: Ventral tegmental area. NAc: Nucleus accumbens. Adapted from (Clapp et al., 2010).

The first study to use dTMS for the treatment of pharmacoresistant MDD was published by Levkovitz *et al.* in 2009, in which 65 patients, who failed to respond to prior antidepressant medication, were treated with three different H-coils (H1, H2 and H1L) and four different stimulation protocols as seen in Figure 2.20. Three groups differed in stimulation laterality (H2 induces bilateral stimulation, H1 preferentially stimulates the left PFC and H1L induces stimulation only over the left PFC) and to the last group was delivered dTMS with the H1L-coil but only at 110 % MT rather than 120 % MT. All subjects were submitted to 20 daily sessions of high-frequency (20 Hz) stimulation, delivered in 42 trains of 2 seconds with an intertrain interval of 20 seconds, resulting in a total of 1680 pulses applied during

15 minutes per session. The complete treatment consisted of 5 daily sessions per week over 4 consecutive weeks (Levkovitz et al., 2009).

The response to the treatment was assessed on a weekly basis, using the 24-item Hamilton Depression Rating Scale (HDRS-24). Response was defined as a decrease of at least 50 % in the HDRS-24 score and the remission state was defined when the absolute HDRS-24 score was 10 or less (Levkovitz et al., 2009). As demonstrated

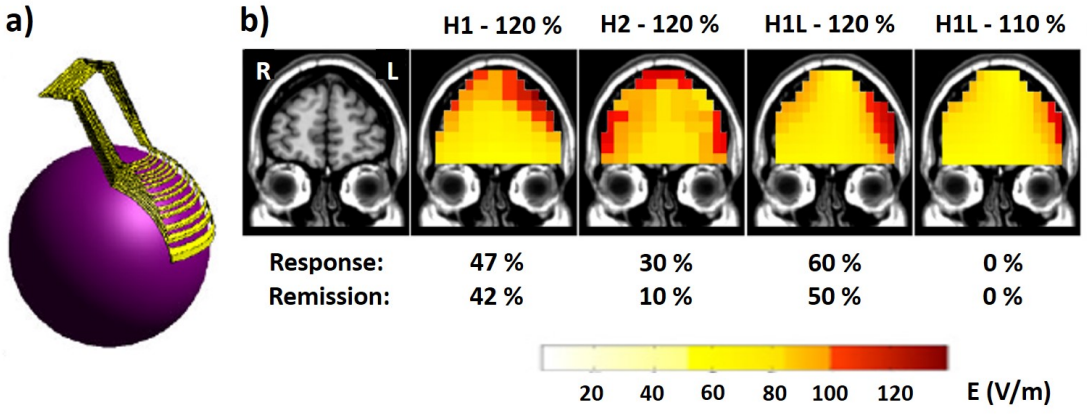

Figure 2.20: **(a)** Schematic representation of the H1L-coil. **(b)** Differential outcomes of four different dTMS protocols. E-field distributions, for all the paradigms tested, were measured in a phantom brain and are presented in a representative coronal slice including the prefrontal cortex. Response and remission rates induced in each group are also presented. Adapted from (Deng et al., 2013*b*, Levkovitz et al., 2009).

in Figure 2.20b, 47 % of the patients treated with the H1-coil, 30 % of the patients treated with the H2-coil and 60 % of the patients stimulated with the H1L-coil at 120 % of MT have responded to the treatment. As for the remission rates, 42 % of the H1-coil group, 10 % of the H2-coil group and 50 % of the patients treated with the H1L-120 % coil have attained the remission status. When the stimulation intensity is lower, 110 % of MT, no response or remission is achieved.

Through this results, the efficacy of dTMS in the treatment of depression was evaluated. It was concluded that unilateral left stimulation of the PFC yielded higher response and remission rates than the bilateral H2-coil stimulation. Additionally, higher stimulation intensity seems to be more effective validating the therapeutic benefits of reaching deep-brain regions like the reward-related pathways (Levkovitz et al., 2009).

Rosenberg *et al.* also verified the efficacy of dTMS, particularly the H1-coil, as an alternative therapeutic tool for treating MDD patients. In his study, seven patients were treated with 20 sessions of 20 Hz dTMS for 4 weeks at 120 % MT. From the 5 subjects who completed the treatment, all of them reached a significant decrease in their HDRS scores, with one achieving remission (Rosenberg et al., 2010). dTMS can also be used as an add-on to medications instead of its use as monotherapy, preferably when antidepressant drugs are partially effective, as published by Isserles *et al.* in 2011. In this study, 20 Hz H1-coil dTMS was also delivered on a daily basis to 57 patients. Again, the HDRS scores were significantly improved although caution was advised regarding the increased risk of seizure induction by magnetic stimulation in patients on high dosages of antidepressant drugs (Isserles et al., 2011).

Electroconvulsive therapy (ECT) is widely used for the treatment of MDD and consists on the induction of a brief seizure by means of the application of electrodes in the scalp through which an electrical current is applied to the brain. With proper duration, such induced seizures are sufficient to lead to antidepressant effects (Sackeim et al., 1993). Minichino *et al.* compared the efficacy and safety of ECT, standard TMS and dTMS protocols on MDD patients. They found that the percentage of remitted patients was the same for ECT and dTMS techniques and the double of that obtained for standard TMS. Therefore, dTMS provides an improved alternative to ECT since the latter requires administration of anaesthetics, induction of seizures and potentially causes memory and cognitive impairments (Bersani et al., 2013).

The Brainsway^{TM} Ltd. dTMS device has received, in 2013, the FDA approval for the treatment of depression in refractory patients (Brainsway, 2013*b*).

2.7.2 Schizophrenia

Schizophrenia is a severe mental disorder and despite not being the most common psychiatric disorder it affects more than 21 million people worldwide (World Health Organization, 2014). It can lead to several disabling symptoms like stress, anxiety, delusions, depression and violent behaviour. Typically, schizophrenia symptoms are

referred to as positive symptoms like hallucinations or negative symptoms which include lack of interest (apathia), emotional and affective flattening and anhedonia (incapability to feel pleasure from enjoyable and social activities) (Bersani et al., 2013). Standard rTMS has already been used and studied as a potential therapeutic tool for the treatment of both positive and negative symptoms of schizophrenia. Low-frequency rTMS have shown to be effective in reducing intensity of positive symptoms like auditory hallucinations (AHs) while high-frequency rTMS has been used to target frontal cortical regions to reduce negative symptoms (Stanford et al., 2008). Such interesting findings clear the way for the potentially more effective stimulation of deeply located regions using dTMS technology, due to its wider and deeper distribution of the induced E-field.

Treatment of auditory hallucinations with dTMS

AHs are present in 50-70 % of schizophrenic patients and are normally expressed as voices speaking to or about the patient. Nonetheless, it is also known that 25-30 % of hallucinating schizophrenic patients are resistant to antipsychotic medications (Rosenberg et al., 2011). Subsequently, low-frequency inhibitory dTMS might have significant potential in improving such symptoms. Functional imaging studies have shown that AHs are associated with episodes of hyperactivity in brain regions like the anterior cingulate cortex, inferior parietal cortex, amygdalae, and structures related to the perception of speech and sound of the temporal, frontal and parietal lobes (Bersani et al., 2013).

After previous studies demonstrated the efficacy of standard rTMS in improving AH severity, when applied over the left temporoparietal cortex, Rosenberg *et al.* were the first to explore the effect of dTMS over the same brain region for the treatment of AHs. Despite the physiological basis of the effects of rTMS on AHs remains not well understood, it seems to be related to a reduced neuron excitability or LTD-like changes in synaptic plasticity (Rosenberg et al., 2011).

The study was performed using the H1-coil for daily sessions on 8 schizophrenic patients, experiencing refractory AHs at least five times a day. All subjects were on antipsychotic medication. The stimulation was applied during 10 minutes per

session at a frequency of 1 Hz (600 pulses) and intensity of 110 % of MT for either 10 ($n = 5$) or 20 ($n = 3$) working days. The symptoms were evaluated using the Auditory Hallucinations Rating Scale (AHRS) and the Scale for Assessment of Positive Symptoms (SAPS). In the first 5 patients, treated with 10 sessions, both the AHRS and SAPS scores improved by 35.5 % and 23.1 %, respectively, but such effects were only temporarily since these results return to the baseline accompanied by a gradual symptomatic deterioration. The last three patients, submitted to 20 sessions, also reduced the AHRS and SAPS scores and two of them maintained such improvement, reflected by a reduction of 42.6 % and 17.9 % on the respective scales, one month after the treatment. From this study, seven out of eight patients improved with the dTMS protocol as an add-on treatment for AHs, and for one patient, the AHs completely stopped (Rosenberg et al., 2011).

More recently, the same authors published a double-blind study, using sham stimulation and real H1-coil stimulation over the aforementioned brain region on 18 schizophrenic patients with AHs. The stimulation protocol was similar to the previous study. However, from the 10 patients that completed the treatment of 10 daily sessions, there was no statistically significant difference between the two groups. Thus, low-frequency dTMS delivered in 10 sessions seems to be insufficient to ameliorate AHs in patients with schizophrenia, although, provided the small sample size, larger studies are needed to validate such conclusions (Rosenberg et al., 2012). Additionally, there is a possibility of the pathophysiology of AHs involving not only the left but also the right hemisphere and that the stimulation of different areas, like the left superior parietal cortex or the right temporal cortex might be beneficial for the clinical improvement of hallucinating patients (Rosenberg et al., 2011).

Treatment of negative schizophrenic symptoms with dTMS

Although the positive symptoms are more frequent in schizophrenia, the negative symptoms are believed to be more decisive regarding the social and functional disability of patients. Moreover, negative symptoms tend to be more refractory to medications, enhancing the need for alternative therapeutic solutions (Bersani

et al., 2013). There has been enough evidence demonstrating that negative symptoms and also cognitive deficits in schizophrenia can be alleviated via excitatory stimulation of the frontal cortex, particularly the dlPFC. Levkovitz *et al.* were the first to study the potentially improved effects of dTMS as an add-on treatment of the aforementioned symptoms (Levkovitz et al., 2011). The excitatory bilateral stimulation protocol was applied on 15 patients, using the H1-coil, at a frequency of 20 Hz and intensity of 120 % of MT. The findings of this study suggested that dTMS in prefrontal regions can induce a beneficial therapeutic outcome for both cognitive deficits and negative symptoms, provided that the dTMS treatment is accompanied by antipsychotic medications. From the 10 patients who completed the 4-week treatment, 70 % respond to the stimulation, having attained $\geq$ 20 % improvement in negative symptoms. In addition, this study also concluded that excitatory dTMS, over the PFC, might enhance frontal lobe-related cognitive functions. Both therapeutic effects were maintained at 2-week post-treatment follow-up (Levkovitz et al., 2011).

2.7.3 Autism spectrum disorder

Autism spectrum disorder (ASD) is a condition that encompasses the more commonly known diagnoses of autism or Asperger syndrome and is characterised by abnormal patterns of cortical excitability and social, communicative and behavioural impairments. (Bersani et al., 2013, Enticott et al., 2014). ASD patients are unable to infer other people thoughts, intentions and feelings leading to defective social skills. The dmPFC was demonstrated to be one of the brain regions that contribute to this process of mentalising or "theory of mind" (*i.e.* the ability to predict what others are thinking) (Enticott et al., 2014). From neuroimaging studies, it was shown that ASD patients present a significantly reduced bilateral activation of the medial PFC (Bersani et al., 2013). Since ASD has very limited therapeutic options, the dmPFC has been considered a potentially fruitful target for the reduction of social deficits. Activation of a larger volume like the dmPFC (see Figure 2.21a) is much more effective when using a

dTMS-like coil since standard rTMS coils induce E-field in a much narrow region and with less penetration depth (Enticott et al., 2014).

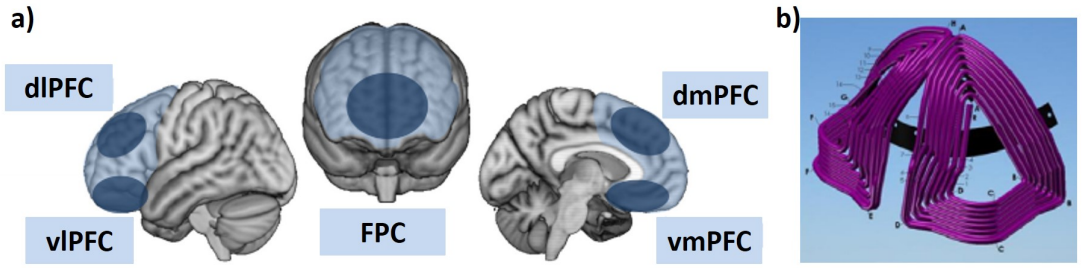

Figure 2.21: **(a)** Regions involved in the pathophysiology of different mental conditions like major depressive disorder, autism spectrum disorder or schizophrenia. Sagittal 3D view of the dorsolateral prefrontal cortex (dlPFC) and ventrolateral prefrontal cortex (vlPFC) represented on the brain surface (left). Coronal 3D view of the frontopolar cortex (FPC) (middle). Sagittal view of the dorsomedial prefrontal cortex (dmPFC) and ventromedial prefrontal cortex (vmPFC) (right). The largest light-blue shaded region corresponds to the prefrontal cortex. **(b)** HAUT-coil used for dTMS. Adapted from (Downar and Daskalakis, 2013) and (Enticott et al., 2014).

Through a double-blind study, Enticott *et al.* investigate the effects of bilateral dTMS over the dmPFC in the improvement of social relating in ASD patients. The daily sessions were performed using the HAUT-coil (see Figure 2.21b) on 28 patients suffering from autism or Asperger syndrome. The real excitatory dTMS was delivered by 10-second trains at 5 Hz for 15 minutes per session, on 15 patients. The sham coil was encased in the same helmet as the real dTMS coil and this sham protocol was applied to 13 patients.

Therapeutic outcomes were evaluated before, after and 1 month following treatment. Patients in the real dTMS group showed a significant reduction in social relating symptoms when compared to the sham group in both post-treatment assessments. Moreover, the active condition patients also reported a decrease in anxiety during emotional social situations whereas no changes were observed for the sham group. In summary, dTMS has the potential to improve social relating impairments and social anxiety, validating the clinical importance of the dmPFC in ASD (Enticott et al., 2014).

2.7.4 Post-stroke rehabilitation

According to the National Institute of Neurological Disorders and Stroke of the USA, the also called brain attack or cerebrovascular accident is the third leading cause of death in the USA, with 600,000 new strokes occurring every year (National Institute of Neurological Disorders and Stroke, 2008). Strokes are a result of a sudden interruption in the blood supply of the brain, commonly caused by a blood clot blocking a blood vessel inside the brain (ischemic stroke). The other main kind of stroke is the haemorrhagic stroke, caused by the disruption of a blood vessel inside (intracerebral) or outside (subarachnoid) the brain, resulting in a haemorrhage that compresses and damages the brain tissue (The Internet Stroke Center: National Institute of Neurological Disorders and Stroke, 2015).

More than 80 % of post-stroke patients experienced an impairment regarding their ability to walk, which contributes for stroke to be a leading cause of long-term disability. Functional imaging studies showed that the motor cortical areas, particularly those associated with the lower limbs, are more activated in the unaffected hemisphere comparatively to the affected one. By reducing this interhemispheric asymmetry of the lower limb motor cortex, via low-frequency rTMS delivered on the unaffected hemisphere, it is possible to improve motor deficits enabling a more symmetric gait (Chieffo, De Prezzo and Leocani, 2014).

Nonetheless, in the chronic phase ($>$ 6 months after) of stroke, the interhemispheric competition is much less pronounced and a bilateral excitatory stimulation over the lower limb cortical motor representation has shown promising results as reported by Chieffo *et al.*. The authors stimulated the deeply located lower limb cortical motor areas of 10 subjects affected by a subcortical stroke, using the H-coil, since standard rTMS coils have difficulties reaching such structures. Each patient received real dTMS and sham stimulation in a random sequence for 3 weeks with an one month interval between protocols.

From the 9 patients who completed the study, it was found that real dTMS is associated with a statistically significant improvement in lower limb function when compared with sham stimulation. The authors concluded that 3 weeks of high-frequency dTMS can induce long-term amelioration of lower limb motor function

lasting at least 1 month after the treatment. Such findings can be explained through the long-term modulatory effects of dTMS potentiated by the daily use of the paretic lower limb, hypothesis validated by the larger difference between the real group and the sham group mainly seen 1 month after the treatment (Chieffo, De Prezzo and Leocani, 2014). Stimulation parameters as well as the main results of this study are summarised in Table 2.2.

Table 2.2: Studies of the effects of dTMS protocols on chronic post-stroke rehabilitation. MT: Motor threshold.

Authors (Year)	**Stimulation protocol**	**Stimulated brain region**	**Main results**
Chieffo *et al.* (2014a)	Two cycles (sham and real), 11 sessions each (30 min) with 1-month wash-out period; 20 Hz; 90 % MT; 1500 pulses/session	Lower limb cortical motor areas	Long-term improvements of lower limb motor function
Chieffo *et al.* (2014)	3 sessions of 10 Hz (800 pulses), 1 Hz (900 pulses) and sham (high or low frequency) with 6-days wash-out period; 100 % MT	Homologous Broca region	Excitatory dTMS improved naming performance

Another frequent consequence of stroke is aphasia which results from the impairment of language functions associated with the Broca region located at the inferior frontal gyrus of the dominant hemisphere. Recently, a study has been published concerning the potential therapeutic effect of dTMS in aphasia recovery (Chieffo, Ferrari and Leocani, 2014). The role of the homologous Broca region located on the non-dominant hemisphere still remains controversial since both excitation and inhibition of this regions seems to improve language performance.

Therefore, Chieffo *et al.* evaluated the effects of dTMS on a picture naming task. Excitatory (10 Hz), inhibitory (1 Hz) and sham dTMS was delivered with 1-week interval, via the H-coil over the right inferior frontal gyrus of 5 right-handed post-stroke aphasic patients. All the patients underwent the referred naming task after each one of the 3 sessions (10 Hz, 1 Hz and sham). Further details of the stimulation parameters are described in Table 2.2.

It was concluded that only the high-frequency dTMS protocol was capable of significantly improve the naming performance, being more effective than the inhibitory dTMS protocol. Consequently, these results further reinforced the

hypothesis that the activation of the non-dominant hemisphere compensates for the loss of language function in chronic aphasia, due to a dominant-hemispheric stroke (Chieffo, Ferrari and Leocani, 2014).

In conclusion, dTMS protocols have several therapeutic applications which can significantly benefit from the deeper and wider E-field distribution induced by the dTMS coil. The slower decay of the E-field with depth of the H-coils allows the direct stimulation of larger and deeper brain volumes, thus being more effective in activating a higher number of networks involved in the pathophysiology of a particular condition.

The Brainsway^{TM} Ltd received a CE (Conformité Européene) Marketing Approval, allowing the marketing and distribution of dTMS devices, in the European Economic Area for the treatment of autism, schizophrenia, Parkinson Disease, Alzheimer Disease and post-stroke rehabilitation (Brainsway, 2013*a*, 2014*b*, 2015). In 2014, the Brainsway^{TM} dTMS therapy was also approved by the Brazilian Health Surveillance Agency (ANVISA) for the treatment of depression, schizophrenia and Parkinson disease (Brainsway, 2014*a*).

Chapter 3

Surpassing the limitations of a whole-brain deep TMS system (Orthogonal Configuration)

3.1 Introduction

Starting from the deep TMS (dTMS) system, developed in previous collaborative work, initial simulations studies performed in the scope of this dissertation yielded unexpected results regarding the safety of the patient. After simulating both the dTMS system and the human model within a surrounding spherical volume of air, the current density induced in the heart of the patient attained prohibitive values, therefore compromising the previously proposed dTMS system.

In the present chapter, the optimisation process is described, which by means of shielding, enabled to reach an alternative and improved solution that not only guarantees the safety of the patient but also the safety of any system operator or nursing staff. Additionally, the new proposed 5-coil system allows for an unprecedented deep-brain stimulation capability, surpassing the standard TMS coils used in clinical practice.

3.2 Human head and torso models considered for the COMSOL Multiphysics® AC/DC-based simulations

The simulation work described in the following sections was performed via the COMSOL Multiphysics® AC/DC Module software (COMSOL Inc., 2015), which is based on the finite element method. Both the software and the numerical method are described in more detail in Appendix I.

In order to assess the effect of the proposed new 5-coil configuration on both the stimulation intensity and penetration power with depth, a spherical human head model and an ellipsoidal torso model were used for the COMSOL Multiphysics® AC/DC simulations.

Stimulation pulse frequency and duration were kept constant throughout the simulations to 5 kHz and 200 μs, respectively.

The head model was comprised of four concentric layers, brain, cerebrospinal fluid (CSF), skull and skin, when considered from the centre of the head model towards its surface (see Figure 3.1). The total radius of the head model was set to

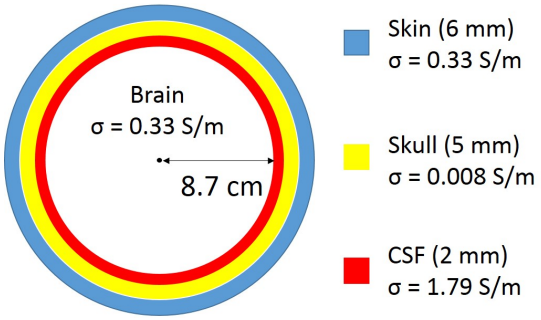

Figure 3.1: Schematic representation of the four-layer spherical human head model used for simulations (axial view). The electrical conductivity, σ, of each layer is also indicated as well as its thickness. The four layers are not shown to scale.

10 cm divided by the 6-mm thick skin layer, the 5-mm thick skull, the 2-mm thick CSF layer and finally the brain volume with an 8.7-cm radius. Each layer considered for the head model was defined according to its particular dielectric properties, namely its electrical conductivity and relative permittivity, although, as detailed in Section 2.2.3, the contribution of the relative permittivity to the induced current

density ($\vec{J}$) can be neglected. Nonetheless, the simulation software demanded that such values were provided, along with the relative permeability ($\mu_r = \mu/\mu_0$) to fully characterise each layer corresponding to an unique domain, as explained in Appendix II. The μ_r for all these biological tissues is equal to 1, as explained in Section 2.2.1.

For the skin, the conductivity value adopted was 0.33 S/m, although the superficial layer of the skin typically has a much lower conductivity, of the order of 10^{-5} S/m, especially when dry (Miranda, 2013). The influence of this micrometer-deep resistive layer must be analysed in future studies. The scalp is made up of skin, fat and muscle which reflects its heterogeneity and anisotropy leading to variations of the conductivity within the scalp by a factor of 20. Nevertheless, it has been often modelled as a single homogeneous tissue with the same conductivity as the skin (Gonçalves et al., 2003, Miranda, 2013).

Brain tissue conductivity largely depends on whether one is referring to the gray matter or white matter. While the gray matter is regarded as an isotropic medium, the white matter is anisotropic with a longitudinal conductivity that can be 10 times greater than the transverse conductivity. However, a simplification can be made when spherical and simpler brain volumes are modelled, like the one used for this work, considering for these cases a single conductivity value of 0.33 S/m, as measured by Gonçalves *et al.* (Gonçalves et al., 2003, Miranda, 2013).

As for the skull, and despite having an anisotropic conductivity resulting from its three different layers and the existence of sutures and natural openings, the average brain to skull conductivity ratio was found to be 40:1, yielding an electrical conductivity of 0.008 S/m for the skull layer.

Baumann *et al.* measured the conductivity of the CSF at 37°C reporting a value of 1.79 S/m, which is constant in the frequency range between 10 Hz and 10 kHz (Baumann et al., 1997, Miranda, 2013).

Spherical head models, such as the one depicted in Figure 3.1, allow for the simulation results, about the effect of the coil characteristics, to be generalised to the overall population, since they are not limited to a particular patient head anatomy or coil position. These simpler models provide a standardised platform,

to assess the influence of different coil geometries and stimulation parameters on the distribution of the induced electric field (E-field), which can be replicated by various researchers among the scientific community (Deng et al., 2013*a*).

In order to mimic the human torso, an ellipsoidal model was defined, for which the conductivity of the skin (σ=0.33 S/m) was considered for the whole volume of the torso. The modelling of the torso emerged from the need to evaluate the induced $\vec{J}$ in the heart tissue, in order to guarantee that a certain safety threshold was not surpassed. Reilly *et al.* studied the induced currents in the heart when the subject was exposed to transient B-fields and also approximated the human torso to an ellipsoidal shape, thus proving the validation of the torso model adopted for this study (Reilly, 1991). Figure 3.2 illustrates the ellipsoidal torso model with the respective dimensions and the estimated position for the heart. The induced $\vec{J}$ value in the heart tissue was calculated as an average of ten point values taken from the central axis of the torso, between the two white lines depicted in Figure 3.2.

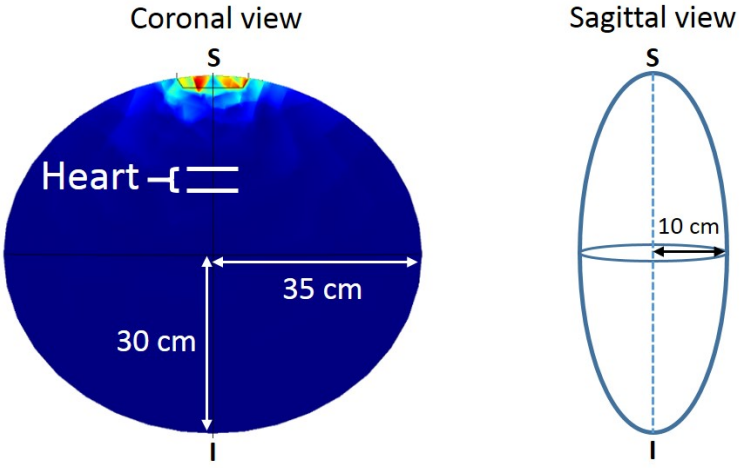

Figure 3.2: Left: Coronal view of the ellipsoidal human torso model used for simulations. The two white lines delimit the estimated position of the heart. **Right:** Sagittal view of the torso model with the third axis dimension. S: superior. I: inferior.

Table 3.1 summarises the dielectric properties for all the tissues considered in the simulation model, head and torso.

Table 3.1: Dielectric properties of the tissues considered for the head and torso models. σ: electrical conductivity. ε_r: relative permittivity.

Tissue	$\boldsymbol{\sigma}$**(S/m)**	$\boldsymbol{\varepsilon_r}$	Reference
Cerebrospinal fluid	1.79	109	Baumann et al. (1997)
Skin (scalp and torso)	0.33	1135	Gonçalves et al. (2003), Miranda (2013)
Skull	0.008	2989	Miranda (2013)
Brain	0.33	42317	Gonçalves et al. (2003)

3.3 The previous orthogonal configuration: safety issues

As it becomes clear to understand, both TMS patients and operators are exposed to time-varying electromagnetic fields (EMFs) and such exposure must be limited. The magnetic pulses produced in TMS can be of the order of a few tesla, lasting only about 0.05-0.2 ms which results in a time derivative of B-field of tens of kT/s (Karlström et al., 2006). Such magnetic pulses can, not only depolarise nerve cells in the brain, but also lead to direct peripheral nerve and muscle stimulation. Therefore, caution must be taken provided the potential adverse health effects that may result from careless exposures to transient electric and magnetic fields.

Previous collaborative work yielded a dTMS system comprised of 5 coils, termed orthogonal configuration (OC), capable of stimulating deeply located brain regions as confirmed via simulation. Such configuration was able to attain more than 50 % relative $\vec{J}$ induction (RI) at the centre of the brain (10-cm depth) in respect to the surface maximum, which represented an unprecedented penetration power with depth.

However, despite initially being thought to be safe to the patient, it was found within the scope of the present work that the previously proposed 5-coil dTMS system was not capable of guaranteeing the safety of the patient after all, since the considered safety thresholds were surpassed. These findings were observed after enclosing the proposed configuration in a surrounding spherical volume of air in order to more accurately replicate real world conditions.

Such discovery was of vital importance because once the proposed configuration was no longer safe to patient, the whole project was compromised.

In addition, the previous OC had not been tested yet regarding the operators safety, which depends on the EMF intensity outside the fibreglass container, in which the 5-coil system will be assembled. Such testing is essential, firstly, because in order to validate the proposed configuration, experimental tests are required and need to be done in the container surroundings. Secondly, the safety of future operators and nursing staff must be guaranteed so that the proposed 5-coil dTMS device can be approved for both academic and clinical practice.

In this section, the adopted stimulation thresholds that assure the safety of the patient and operator are described as well as the specifications of the previous OC. Simulation results reflecting the induction capability of the previous system both in the patient and in the operator are also discussed.

3.3.1 Stimulation thresholds

For the purpose of defining the exposure limits to low-frequency [1] EMFs, several guidelines have been established to provide proper protection against all known adverse effects. One of the organisations responsible for the publication of such guidelines is the International Commission on Non-Ionizing Radiation Protection (ICNIRP).

As stated in Chapter 2, in free space, vacuum and air, as well as in non-magnetic materials, including biological tissues, the magnetic flux density, B, and the magnetic field strength, H, are related by the same constant of proportionality defined as the magnetic permeability, μ equal to $4\pi \cdot 10^{-7}$ H/m (ICNIRP, 2010, Parlamento Europeu and Conselho da União Europeia, 2013). Hence, the human body does not perturb the B-field. It is, in fact, the Faraday induction of E-fields within the tissues that constitutes the main interaction of transient B-fields with biological structures. The distribution of such E-fields and resulting currents is quite dependent upon the electrical conductivity of the different organs (Nowak et al., 2011).

[1] Low-frequency range extends from 1 Hz to 100 kHz as stated by ICNIRP.

Heart fibrillation threshold

Myelinated nerve fibres and muscle tissue are particularly excitable and their responsiveness to electrical stimuli has been well known. Pulsed fields induced in brain tissue during the application of TMS can be as high as 100 V/m (peak value) even though some theoretical work suggests that central nervous system (CNS) minimum stimulation threshold can be of about 10 times lower, *i.e.* 10 V/m (peak value), whereas peripheral nervous system has a minimum stimulation threshold of about 4-6 V/m (peak value) (Reilly, 2002). Furthermore, such stimulation thresholds rise for higher frequencies, of the order of kHz, mainly because the period of the pulse gets shorter leading to less time available for charge accumulation to occur at the nerve membrane.

Even though muscle fibres are more difficult to stimulate, when compared to nerve tissue, cardiac muscle stands as a particular case, requiring special attention. When the heart is electrically stimulated, potentially life-threatening events can occur, like ventricular fibrillation. Cardiac fibrillation is a condition where the heart electrical activity becomes disordered leading to an unsynchronized contraction of the ventricles. Consequently, the heart will no longer be able to pump the required amount of blood for the entire organism. Such heart malfunctions are more likely to be triggered when the stimuli is applied during the vulnerable period of the heart cycle, *i.e.* during the portion of cardiac cycle when ventricles are recovering to it resting state (ventricular repolarisation) (American Heart Association, 2014).

It is important, though, to acknowledge the difference between cardiac tissue stimulation and the induction of heart fibrillation. The first does not necessarily implies the second, as the ventricular fibrillation thresholds can be 50 times higher than those required to stimulate cardiac muscle fibres (Reilly, 2002).

As demonstrated in 1998, volunteers exposed to approximately 1 kHz B-fields, from an experimental magnetic resonance imaging system have experienced both peripheral nerve and muscle stimulation. This pulsed B-fields induced currents in peripheral tissues with a $\vec{J}$ of about 1 A/m^2. ICNIRP then claimed that transient EMF inducing such currents, with $\vec{J}$ above 1 A/m^2, can lead to adverse health effects such as cardiac fibrillation which remain after the application of the stimuli

(ICNIRP, 1998). Bailey *et al.* also considered the nominal minimum thresholds for cardiac stimulation and ventricular fibrillation to be 1 A/m^2 and 2 A/m^2, respectively (Bailey et al., 1997). As for the 2010 guidelines, the ICNIRP establishes that, above 400 Hz, limits on peripheral nerve stimulation should apply in all parts of the body, resulting in a heart stimulation threshold of 4 V/m (1.32 A/m^2, calculated for a tissue conductivity of 0.33 S/m). A more conservative exposure limit is adopted by these recommendations, which set the limits for occupational exposure as 0.45 A/m^2 for a stimulation frequency of 5 kHz. When compared with the previous 1998 guidelines, one of the main changes introduced in 2010 was the use of a different physical quantity, the induced internal E-field, instead of the induced $\vec{J}$, as the principal factor to determine the biological effect (ICNIRP, 2010).

Nonetheless, restrictions on exposure to EMF can still be expressed as induced current density since the internal E-field, $\vec{E}_i$, and current density, $\vec{J}$, are related by Ohm Law as it was previously explained in Section 2.2.3.

There has been, however, some speculation and controversy regarding the specific value for the heart fibrillation threshold. Following the more recent ICNIRP guidelines (2010), Bakker *et al.* found a strongly dependence of the ICNIRP 2010 results on the grid discretisation step and the number of distinguished tissues in the anatomical models used. It is the author belief that different research institutes should improve their protocols and methodology in order to achieve more consistent results. Consequently, the uncertainties related to discretisation settings and different anatomical models can be mitigated (Bakker et al., 2012). Such guidelines were derived from computational simulations using only two anatomical models (adult male and female). Thus, it is understandable that in face of the highly diversity of individual anatomy, this simulation results can not be generalised to the entire population. The limitations of exposure to transient EMF set by the ICNIRP at higher frequencies (above 400 Hz) are a result of an extrapolation of experimental data obtained for much lower frequencies (20 Hz) (Bakker et al., 2012).

Additionally, the biological significance of such restrictions remains unclear for

higher frequencies, which is the case of the 5 kHz pulsed B-fields used in this work. Loo *et al.*, also state that further studies are necessary to understand if occupational, low-intensity and continuous exposure has the same effects that high intensity, pulsed, TMS-like stimulation (Loo et al., 2008).

Nevertheless, an exposure limit, concerning the protection against the induction of heart fibrillation, must be considered in the scope of this work. The fibrillation threshold of 1 A/m^2 was adopted, since it is considered to be a conservative value and it is in compliance with previous collaborative work (Silva et al., 2012, Sousa et al., 2014). However, the more recent and conservative exposure limit of 0.45 A/m^2, set for frequencies of 5 kHz, will also be taken into account, despite not having been specifically established for preventing heart fibrillation[2].

With this in mind, in the following simulation studies, for a particular configuration to be considered safe it must induce a current density value in the heart that lies below 4.5 mA/m^2. Such value was defined as the safety threshold since it is 100 times inferior to the 2010 exposure limit and almost three orders of magnitude smaller than the previously adopted 1 A/m^2 limit.

Magnetophosphenes threshold

Apart from direct nerve and muscle stimulation, exposure to time-varying EMF can lead to an also well established effect which is the induction of retinal phosphenes, also known as magnetic or magnetophosphenes. This is nothing more than the perception of faint flickering light in the peripheral visual field caused by the induced electrical currents that stimulate the retina and perhaps the optic nerve. This structure, located at the posterior inside region of the eye, is the light-sensitive tissue, part of the CNS, considered to be a proper and conservative model of the electrostimulation responses that occur in CNS neuronal circuitry. The induction of magnetophosphenes occurs at the lowest electromagnetic stimulation threshold, regarding all the established effects of exposure to low-frequency EMF. With this

[2]The exposure limit of 0.45 A/m^2 was defined regarding all the tissues of the human body.

in mind, avoiding magnetophosphenes should protect against any possible adverse effects on brain tissue (Hirata et al., 2011, ICNIRP, 2010).

As demonstrated by Lövsund *et al.*, in 1980, the maximum sensitivity to this light sensations occurs at approximately 20 Hz, where EMFs of very low frequency (10-50 Hz) and moderate flux density (0-40 mT) were used to generate retinal phosphenes. Threshold values were obtained from three test groups with healthy subjects and one last group with colour defective subjects, which exposed their heads to a transient B-field generated between the poles of an electromagnet. The threshold magnetic flux density was found to be about 10-12 mT and dependent of the background light intensity (Lövsund et al., 1980). Based on Lövsund study, Laakso *et al.* conducted a computational analysis to determine the retinal threshold E-field and $\vec{J}$ capable of inducing magnetophosphenes. Although magnetic phosphenes can be generated in the brain, more specifically in the occipital cortex, by either electrical stimulation or TMS, the threshold E-field for inducing phosphenes in the brain is significantly higher than that required for the retina. Therefore, considering the retinal phospenes over the ones generated in the occipital cortex is a more conservative and reliable approach. Five anatomical models of the head were used and the exposure conditions of Lövsund*et al.* study were reproduced, using two spherical magnetic poles, one on each side of the head (Laakso and Hirata, 2012).

As shown in Figure 3.3 the threshold $\vec{J}$ for retinal phosphenes was determined as 10 mA/m^2 at 20 Hz for a background luminance [3] of 1.2 cd/m^2. These results are in agreement with Lövsund conclusions that the magnetophosphenes threshold depends on the background light intensity and on the stimulation frequency. Maximum sensitivity to phosphenes occurs at 20 Hz, where a higher luminance decreases the sensitivity. The $\vec{J}$ value of 10 mA/m^2 also matches with the exposure limit established by the 1998 and 2010 ICNIRP guidelines (ICNIRP, 1998, 2010). Furthermore, it is important to emphasise that phosphenes threshold rapidly rises at lower and higher frequencies, as can be seen by the increase observed in Figure 3.3 when going from 20 Hz to 45 Hz.

[3] Candela per square meter (cd/m^2) is the SI unit for luminance. A commom computer screen emits up to 300 cd/m^2.

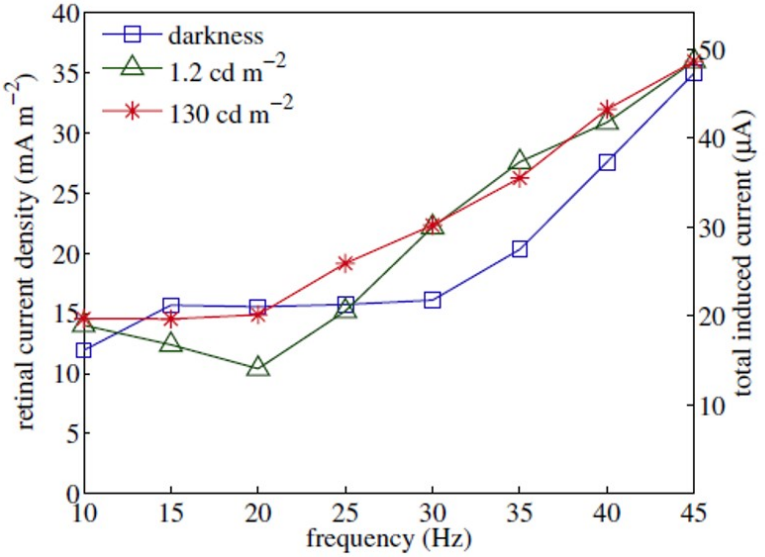

Figure 3.3: Retinal current density and total induced current as a function of the EMF frequency and background light intensity. After (Laakso and Hirata, 2012).

Provided that, a gap was identified, since no conclusive studies were found regarding the definition of exposure restrictions in order to avoid the induction of retinal phosphenes for higher stimulation frequencies, particularly at the kHz range. From an extrapolation exercise applied to the data presented in Figure 3.3, it is observed that for an increment of just 25 Hz, the limit value goes from 10 mA/m^2 up to 35 mA/m^2 (a 3.5-fold increase). As the TMS pulse frequency used was 5 kHz (250 times greater than 20 Hz) it was a conservative estimate to adopt a $\vec{J}$ value of 1 A/m^2, which is only 100 times greater than the limit determined at 20 Hz. Once again this adopted threshold is in compliance with previous work (Silva et al., 2012, Sousa et al., 2014).

3.3.2 Specifications of the previous orthogonal configuration

The previous optimised OC included five large rectangular coils positioned perpendicular to each other, around the head model, one on each side of the head, one anteriorly located and the remaining two were placed behind the patient head, on a posterior location. Henceforth, these coils will be addressed by the letters A to E as shown in Figure 3.4.

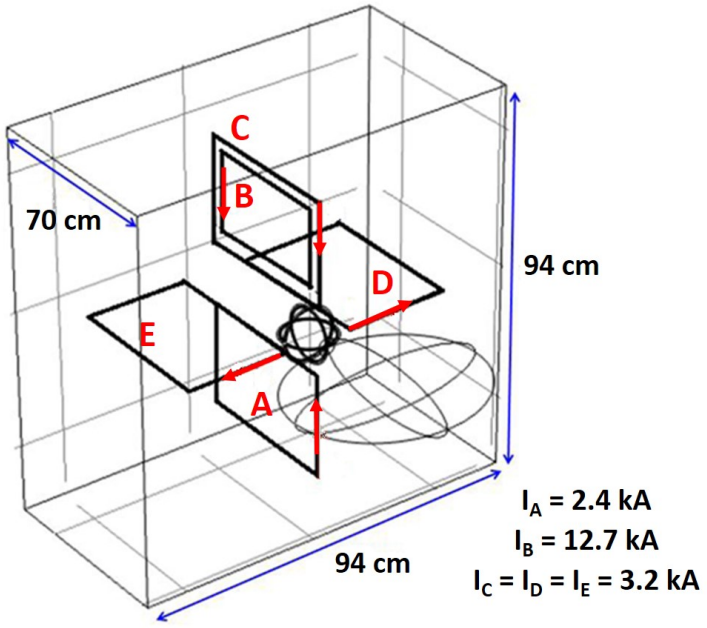

Figure 3.4: Schematic representation of the previous orthogonal configuration. The five coils surrounding the head model are placed anteriorly (A), posteriorly (B and C) and laterally (D on the right side and E on the left side). All the coils have approximately the same dimensions except for the smaller coil (B) which is placed within the coil C. The red arrows indicate the direction of the current passing through each coil and their absolute maximum values, in kA, are indicated below. Image is not shown to scale.

All the 5 coils and the most part of the head model are immersed in a conducting liquid ($\sigma = 10$ S/m), held by an 94×94×70 cm^3 fibreglass container, also depicted in Figure 3.4. The reasons behind the implementation of a conducting liquid, which can be a saline solution, are explained further in Chapter 4.

As for the current flowing in each coil, its direction is indicated by the respective red arrow in Figure 3.4. Regarding the value of the current in each coil, the decisive factor that influences the E-field distribution and the relative induction at the centre of the brain is the ratio between currents rather than their absolute values. After determining the most suitable proportion between the five currents ($I_i, i = A, B, C, D, E$), it is relatively straightforward to increase/decrease the induced $\vec{J}$ in the brain volume by increasing/decreasing the current value in all the coils, simultaneously, by the same amount. For the aforementioned configuration, the most advantageous current ratio was found to be $I_A = 0.75I_0$, $I_B = -4I_0$, $I_C = I_0$, $I_D = I_E = -I_0$, where $I_0 = 3184$ A, which is the current delivered by the available, built in-house magnetic stimulator (Simões et al., 2013).

Lastly, Figure 3.5 illustrates the coils used in the OC as well as their respective dimensions.

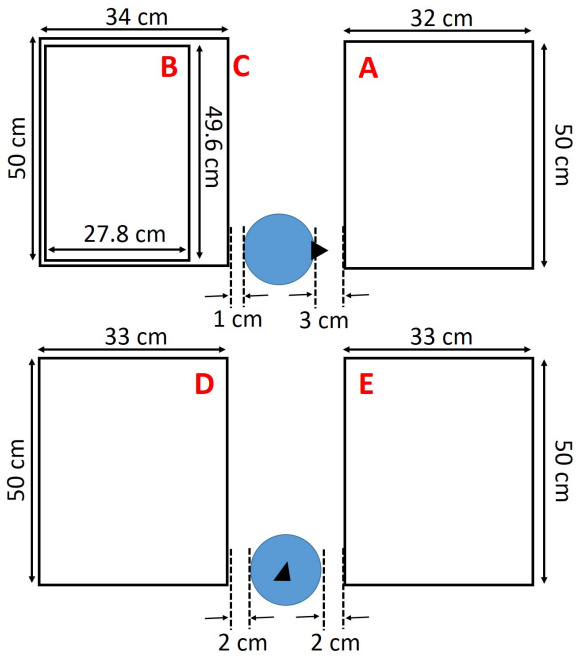

Figure 3.5: Schematic representation of the 5 coils used in the previous orthogonal configuration and their respective dimensions (width and height). The blue circle represents the 10-cm radius head model (scalp domain). Image is not shown to scale.

Until this point, the specifications indicated for the previous OC resulted from optimisation studies carried out in previous collaborative work.

All the results presented in the following sections were obtained either from simulation or experimental studies performed in the scope of the present work.

3.3.3 Patient safety

After surrounding the whole dTMS device (coils and conducting liquid) as well as the patient (head and torso) with a spherical volume of air, the stimulation capability of the previous OC significantly changed in respect to the results reported by Sousa *et al.* (Sousa et al., 2014).

This volume of air was implemented as a consequence of the need to investigate the stimulation power outside the fibreglass container, as seen by the study presented in the next section. Additionally, this implementation also

allowed to replicate a realistic medium around the simulation apparatus (see Figure 3.6). Such domain was defined in COMSOL Multiphysics® AC/DC as a sphere with a few-meter radius and the dielectric/magnetic properties of air ($\sigma = 3 \cdot 10^{-15}$ S/m (Pawar et al., 2009), $\varepsilon_r = 1$ and $\mu_r = 1$).

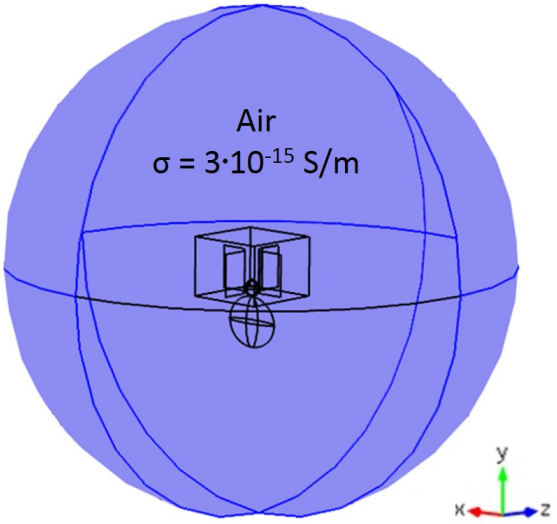

Figure 3.6: Volume of air as a spherical domain with a 3-m radius considered for the COMSOL Multiphysics® AC/DC simulations, mimicking the world of air surrounding both the 5-coil system and the patient.

Considering the spherical surface of this "world" of air as an independent domain in COMSOL Multiphysics® AC/DC, it was possible to set the boundary condition in which the potential is zero at the surface of the volume of air. This way, the spherical surface was imposed to be the infinity in which the E-field approaches zero. The steps required to set this zero of potencial at infinity are explained in Appendix IV.

The distribution of the induced $\vec{J}$ obtained after simulating the previous OC surrounded by a 2-m radius sphere of air is illustrated in Figure 3.7. A three-dimensional view of the brain volume as well as the three central slices (axial, coronal and sagittal) are depicted.

From the results presented in Figure 3.7, one can see that the penetration power with depth is quite significant with an induced $\vec{J}$ of about 7 A/m^2 at the centre of the brain. The minimum $\vec{J}$ profile still remains anteriorly located, although it has shifted to a more inferior location when compared to the results obtained with no volume of air surrounding the dTMS device and the patient.

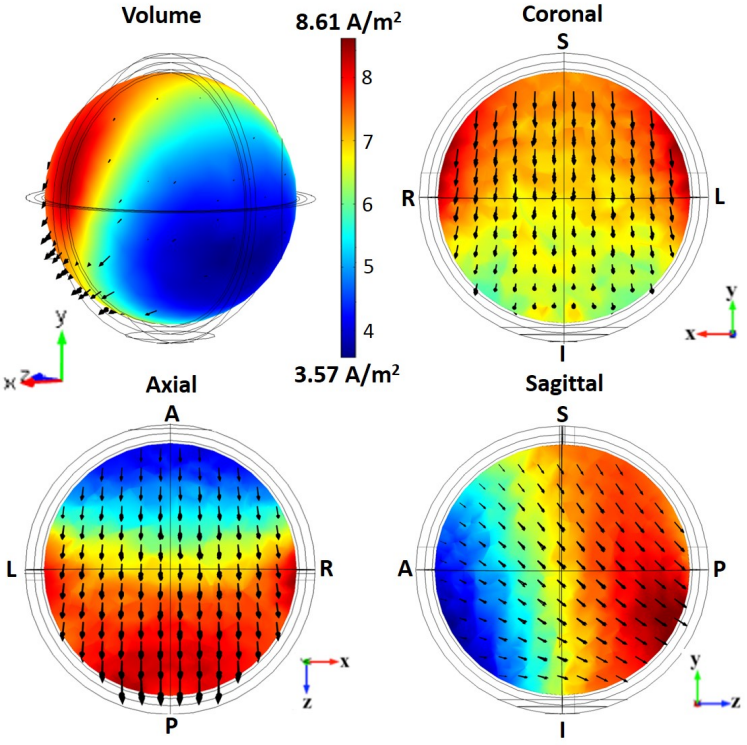

Figure 3.7: Distribution (colour scale) and direction (arrows) of the induced current density represented in a three-dimensional view and central slices (coronal, axial and sagittal) of the brain volume, obtained with the setup of Figure 3.4. The illustrated stimulation was performed having the 5-coils and the head model immersed in conducting liquid and the whole system surrounded by a 2-m radius spherical volume of air. A: anterior. P: posterior. L: left. R: right. S: superior. I: inferior.

In order to, clearly, evaluate the influence of having the surrounding world of air, another simulation was performed with exactly the same parameters as the simulation illustrated in Figure 3.7, but this time with the previous OC and the patient not enclosed by a spherical medium of air. The results of both simulations are presented in Table 3.2.

Table 3.2: Induced current density values in the brain and torso of the patient, when the whole system is surrounded by a spherical medium of air (Simulation A) and when neither the system of coils nor the patient are enclosed in a volume of air (Simulation B). RI: relative induction in respect to the surface maximum.

Simulation	**Brain Volume (A/m²)**			**Torso Volume (A/m²)**		
	Max	**Min**	**Centre | RI (%)**	**Max**	**Min**	**Heart**
A	8.611	3.573	6.822 | 79.2	2.013	0.116	0.466
B	7.383	0.232	3.785 | 51.2	$1.838 \cdot 10^{-3}$	$4.278 \cdot 10^{-8}$	$3.419 \cdot 10^{-6}$

Although the enclosure of the whole system in a medium of air significantly increased the RI at the centre of the brain, going from about 50 % to almost 80 %, the minimum induced $\vec{J}$ also grew over three times, up to 40 % of the surface maximum, thus, the induced $\vec{J}$ surpasses the magnetophosphenes threshold.

Nevertheless, the implementation of this world of air seemed to have greater influence over the induced $\vec{J}$ values in the patient torso. Such results are not surprising, since the induced $\vec{J}$ in the brain volume is mainly determined by the conducting liquid in which both the head and the coils were immersed. For the patient torso, however, which was not immersed in conducting liquid, the effect of considering a volume of air surrounding the whole apparatus is expected to be much more significant.

Subsequently, the induced $\vec{J}$ in the patient heart increased over five orders of magnitude to a prohibitive value of 0.47 A/m^2 when the simulation apparatus is surrounded by air. Such induced current in the heart tissue clearly surpasses the adopted safety threshold of 4.5 mA/m^2 (see Section 3.3.1) , thus compromising the safety of the patient.

3.3.4 Operator safety

As mentioned before, in Section 2.5.6, conventional TMS equipments have well documented side effects, although it is commonly accepted that TMS is a safe technique.

From the patient point of view, standard TMS/rTMS protocols do not represent significant exposure to B-fields since the total procedure time is too short. There are reported cases where patients who received very prolonged treatments, up to 12 months, and several hundreds of pulses/stimuli experienced no side effects whatsoever. Still, all these statements were based on clinical studies performed with standard TMS equipments, like the figure-8 coil (Di Lazzaro et al., 2010, Rossi et al., 2009).

However, studies regarding the safety of operators that undergo a continuous and long exposure, several hours every day, to B-fields are much less frequent.

Concerning TMS system operators, only one study was carried out, using a standard stimulator and figure-8 coil (Karlström et al., 2006). In this study, the time derivative of the B-field, dB/dt, was measured at distances ranging from 0.1 m to 0.5 m in 10 cm intervals, at the operator side of the coil. The dB/dt scans were taken along the field symmetry axis of the figure-8 coil, *i.e.* a vertical axis at the coils intersection point, perpendicular to the surface of the two coil transducer. The dB/dt signal is depicted in Figure 3.8 as well as the variation of dB/dt with distance.

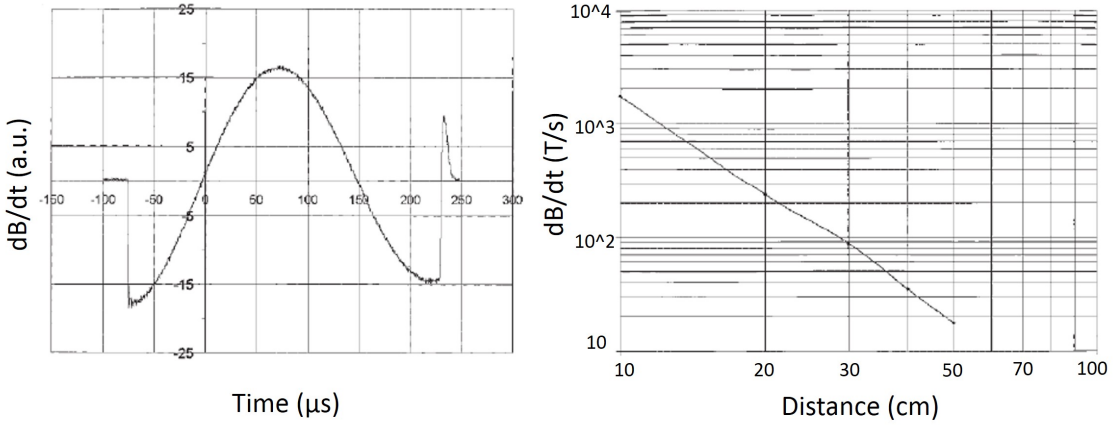

Figure 3.8: a) dB/dt signal measured at 10 cm apart from the coil along the central axis and at the operator side of the coil. **b)** Logarithmic graph of peak dB/dt *versus* distance. After (Karlström et al., 2006).

The rTMS pulses used in this study have a period of about 300 μs as can be seen from Figure 3.8a. The log plot to the right shows the intensity decrease of the B-field with distance, proportional to $1/r^3$ (r = distance from the coil).

Karlström *et al.* found that the worker exposure limits to magnetic pulses were exceeded at distances less than or equal to 0.7 m from the coil. For the frequency used in this study, 3.5 kHz, the limit value for dB/dt, according to the ICNIRP guidelines, is about 1 T/s (ICNIRP, 2003). The TMS coil can be seen as a single dipole producing a symmetric B-field in cylindrical coordinates and decreasing exponentially with $1/r^3$.

Such observation underlines the need to establish the potential long-term adverse effects for TMS operators, determining safety parameters such as the distance to the coil depending on the type of TMS protocol. Karlström *et al.* also

highlighted the necessity of further studies using different TMS devices, coils and configurations in order to achieve deeper understanding regarding the protection of TMS nursing staff from unnecessary exposures.

Regarding the OC and due to the high currents, of the order of a few tens of kA (kiloampere), flowing through the five coils, it is expected that the induced B-field near the fibreglass container will lead to excessive $\vec{J}$ values in the operator torso, going close or even surpassing the heart fibrillation threshold of 1 A/m^2.

Consequently, a simulation study was carried out with two main objectives. Firstly, to evaluate the safety of the previous OC in respect to the future operators and/or nursing staff and secondly, to understand whether the presence of the conducting liquid has a significant effect in the distribution and intensity of the induced $\vec{J}$ in the operator torso.

As seen in Figure 3.9, three ellipsoidal torsos were placed alongside the fibreglass container (represented by the conducting liquid domain) at 10 cm apart. One was located behind coils B and C (posterior position), the second, behind coil D (lateral position) and the third, behind coil A (anterior position). The simulations were done considering, first, the coils and the head model immersed in conducting liquid and then surrounded by air.

As seen by the colour scale in Figure 3.9, the most dangerous location for the operator is, as expected, behind the coils B and C, since the current in the smaller coil B is at least 4 times higher than the current in the remaining coils. Therefore, the intensity of the induced B-field and consequently the current density induced in the operator torso is higher when the operator is positioned posteriorly to the patient.

If the system of coils and the head model were surrounded by air, instead of a conducting solution, the distribution and magnitude of the induced $\vec{J}$, in the operator torso, is quite similar as illustrated in Figure 3.10.

The only major difference observed was associated with the direction of the induced currents which are opposite when the coils are surrounded by conducting liquid or air. Such effect was also expected since, according to the Lenz law the magnetically induced currents flow in the opposite direction to that of the primary

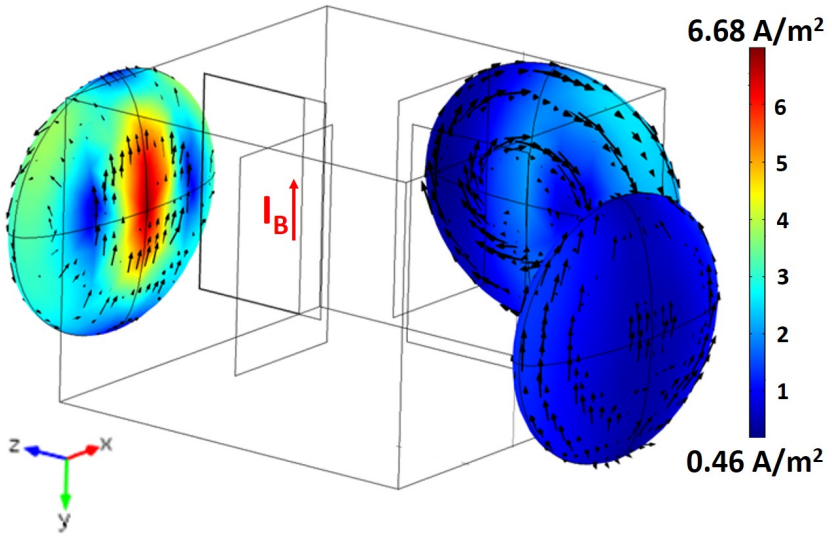

Figure 3.9: Three-dimensional view of the three ellipsoidal torsos anteriorly, posteriorly and laterally located. Torsos are positioned 10 cm away from the container. The distribution (colour scale) and direction (arrows) of the induced current density in all three torsos is also illustrated as well as the direction of the current in coil B. Both the 5 coils and the patient head were immersed in conducting liquid. Arrows are represented in logarithmic scale.

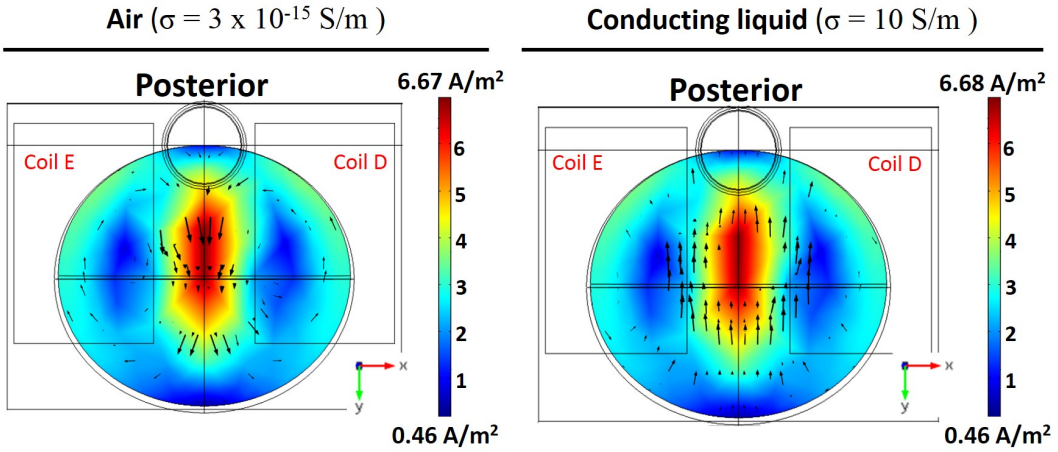

Figure 3.10: Distribution (colour scale) and direction (arrows) of the induced current density in a coronal view of the operator torso located in a posterior position, behind coils B and C (not shown), with the 5 coils surrounded by air (left) and conducting liquid (right). Patient torso is not shown.

increasing current passing through the coils, which is the case when the coils are surrounded by air. When considering the conducting liquid, the currents induced in the operator torso are influenced not only by the transient current in the coils but also by the currents induced within the conducting liquid which, in turn, will induce the currents in the operator torso. As a result the currents in the torso will

flow in the same direction as the current in the coils and in the opposite direction of the currents induced within the solution. This topic will be discussed further in Chapter 4. The results obtained for the torsos placed on the anterior and lateral positions are presented in Appendix V, as well as the results from the simulation with the three torsos, similar to Figure 3.9 but with the 5-coil system surrounded by air.

In order to assess the magnitude of the $\vec{J}$ induced in the heart of the operator, the posteriorly located torso (representing the worst case scenario) was simulated at variable distances from the container, first with the coils surrounded by conducting liquid and then by air. The results obtained are presented in Table 3.3.

Table 3.3: Current density (A/m^2) induced in the heart of the operator located posteriorly to the patient, at variable distances from the container. The percentage values reflect the difference in having air or conducting liquid surrounding the 5 coils and the head model.

Distance (cm)	**Operator heart (A/m^2)**		**Relative difference (%)**
	Air	**Conducting liquid**	
0	4.654	4.511	3.1
10	1.830	1.876	2.4
40	0.190	0.192	0.2
70	$8.542 \cdot 10^{-2}$	$8.536 \cdot 10^{-2}$	0.1
130	$1.830 \cdot 10^{-2}$	$1.826 \cdot 10^{-2}$	0.5
200	$9.394 \cdot 10^{-3}$	$1.891 \cdot 10^{-2}$	0.2
260	$4.441 \cdot 10^{-3}$	$4.319 \cdot 10^{-3}$	2.7

Once again, it was demonstrated that the difference in having conducting solution or air surrounding the 5-coil system is not significant, with the major relative difference lying in the 3 % range (the reference value was considered to be the maximum between the two values).

Furthermore, it can be seen that the induced $\vec{J}$ in the heart of an operator located behind the patient is clearly not acceptable regarding the heart fibrillation threshold, particularly when the torso is placed right next to the container in which the induced $\vec{J}$ distinctively surpasses the adopted threshold. Only for distances equal or greater than 2.6 m the $\vec{J}$ induced in the heart drops below the safety threshold of 4.5 mA/m^2.

Influence of the size of the surrounding volume of air over the simulation results

With the introduction of the world of air as a part of the simulation model, it was necessary to investigate if changing the size of the surrounding volume affects the simulation results, namely the induced $\vec{J}$ in the patient brain and torso.

Subsequently, the previous OC was simulated while surrounded by a volume of air with different sizes. Additionally, the simulations in this study were performed using the same predefined mesh size: *Finer*, with first order tetrahedral elements (for more details on mesh refinement see Appendix I). The currents were also slightly altered to the following values: $I_A = I_0$, $I_C = I_D = I_E = 2I_0$, and $I_B = 8I_0$, with $I_0 = 3184$ A. The results obtained for each radius of the air volume are presented in Table 3.4.

Table 3.4: Current density (A/m^2) induced in the patient brain and torso. The radius of the sphere surrounding the 5-coil system and the patient was altered. All the remaining simulation parameters were kept constant. The number of elements in the mesh is also indicated. RI: relative induction in respect to the surface maximum.

Radius (m)	**No. elements**	**Brain volume (A/m²)**		**Torso volume (A/m²)**
		Max	**Centre | RI (%)**	**Max**
1.5	174,228	17.305	13.626 | 78.7	3.993
2.0	143,247	17.086	13.652 | 79.9	3.898
2.5	123,384	17.182	13.819 | 80.4	3.918
3.0	113,960	17.564	13.589 | 77.4	3.787
3.5	106,172	17.134	13.182 | 76.9	3.779
4.0	98,474	18.162	13.350 | 73.5	3.599
4.5	92,729	17.645	13.485 | 76.4	3.860
5.0	88,148	17.566	14.249 | 81.1	3.921
6.5	80,116	17.321	13.692 | 79.0	4.055
8.0	74,766	17.942	14.160 | 78.9	3.827

Throughout this work, several comparisons between simulation results are presented and the metric used for such comparison was the percentage relative error:

$$\delta x = \frac{|x_0 - x|}{x} \times 100\ \% \tag{3.1}$$

The reference value x was considered as the value obtained from the solution calculated from a more refined mesh, with a higher number of elements, which reflects the most accurate solution. For a difference between two given results to be considered significant, the δx must be higher than 10 %.

From Table 3.4 and according to this criterion, it can be seen that varying the radius of the spherical volume of air does not significantly affect the simulation results. Considering the reference values as the ones obtained with the 1.5-m radius sphere, the δx remains below the 10 % limit, both for the $\vec{J}$ values in the brain and in the torso volume (see Table 3.5).

Table 3.5: Maximum values of the percentage relative error (δx) in respect to the current density induced in the brain and torso volumes. The values of (δx) were calculated for the cases where the difference $|x_0 - x|$ was higher. RI: relative induction.

	Brain volume			**Torso volume**
	Max	**Centre**	**RI**	**Max**
δx (%)	5.0	4.6	6.6	9.9

In addition, an extra simulation was performed in the same conditions, with an 8-m radius surrounding sphere of air but with the more refined mesh *Extra Fine*, using 294,682 tetrahedral first order elements. The results were very similar to the ones obtained with the mesh size *Finer*, yielding a maximum $\vec{J}$ of 17.34 A/m^2 and 3.79 A/m^2 in the brain and torso volumes, respectively. The RI at the brain centre was also quite identical reaching 80.5 %. Such result supports the validity of the aforementioned study since the values of the induced $\vec{J}$ remained constant even when considering a more refined mesh.

Therefore, it was proved that all the tested sizes of the surrounding volume of air do not have any influence over the simulation results for the considered geometry model. The most suitable radius for the sphere, along with the proper mesh, must be chosen according to the geometry and number of elements required for each particular problem, to assure that the simulation error falls within the accepted range (*i.e.* below 10 %).

3.4 Solving safety issues by means of shielding, distance and coil geometry

As demonstrated by the simulation results, in Section 3.3.3, the previous OC was not capable of guaranteeing the safety of the patient, since the stimulation induced in the heart might potentially lead to ventricular fibrillation.

Therefore, it was imperative to find a relatively simple solution that would allow the stimulation of deeper brain regions while keeping the system operator and most importantly, the patient, safe.

By adapting the existing configuration it was possible to find a new, reliable and safe design, capable of achieving unprecedented deep-brain stimulation, overcoming the RI at the centre of the brain attained by the previous OC. All this, without compromising the safety of the patient and of the operator.

3.4.1 The new, improved orthogonal configuration

After redesigning the coil geometry, adjusting the ratio between currents and implementing a proper shielding structure enclosing the system of coils, a new orthogonal configuration was put forward.

The new system also includes 5 coils, placed perpendicularly in respect to the patient head, which are arranged in the same way as the previous OC. All the coils as well the head model were immersed in conducting liquid, comprised by the same fibreglass container described for the previous OC. Figure 3.11 illustrates the new OC, now comprised of three triangular coils and just two rectangular coils. The magnitude of the current flowing through each coil is also indicated.

The dimensions of the fibreglass container, represented by the conducting solution domain in COMSOL® AC/DC, were kept constant from the previous OC as well as the electrical conductivity of the conducting liquid (10 S/m). As seen in Figure 3.12, the coils of the new system have similar dimensions to the ones on the previous OC except for the shape of coils A, D and E. The value of the current passing through coil A was also decreased to $I_A = 0.3I_0$, whereas for the other coils, the current remain unchanged.

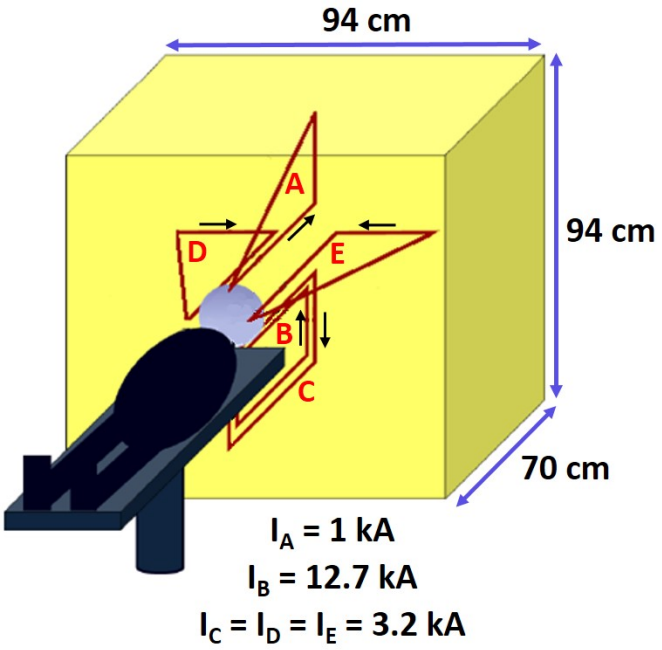

Figure 3.11: Schematics for the new orthogonal configuration. The 3 triangular coils are placed anteriorly (A) and laterally (D and E) while the rectangular smaller coil B is placed within the larger rectangular coil C. The black arrows indicate the direction of the current passing through each coil and their absolute volutes, in kA, are indicated below. The dimensions of the fibreglass container, in yellow, are also indicated. Image is not shown to scale.

However, the most significant modification was the implementation of a highly conductive metal cage around the fibreglass container to shield the B-field lines, preventing them from escaping the source volume. Part of this shielding structure can be seen in Figure 3.13, enclosing the 5-coil system, the patient head and the conducting liquid (not shown).

This 3-cm thick metal frame has a small opening for the patient head to get through the structure, which then closes around the neck, with a minimum distance of 2 cm. This way the patient is never in direct contact with the metal.

As explained further on, the results obtained with the shielding structure, illustrated in Figure 3.13, were of vital importance regarding the continuity of the Deep-Brain TMS project, since this new proposed configuration guarantees not only the safety of the patient but also the safety of any system operator and/or nursing staff.

In the next sections, all the optimisation processes leading to the new, improved orthogonal configuration are described.

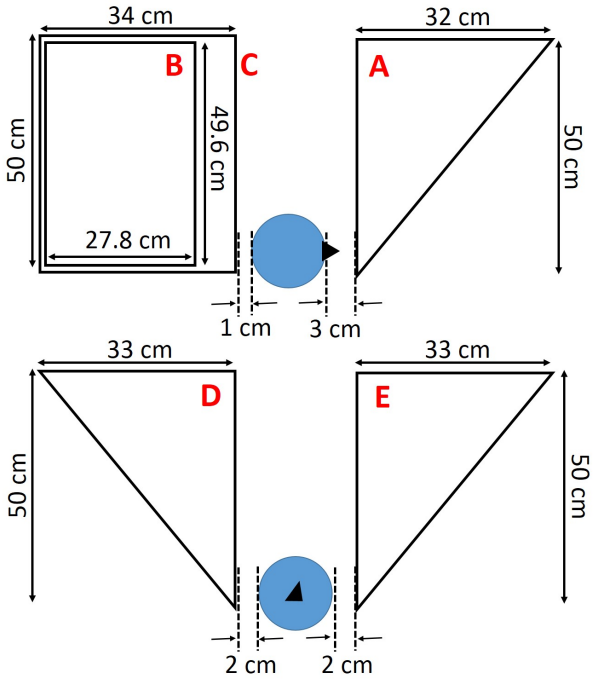

Figure 3.12: Schematic representation of the rectangular coils B and C and the triangular coils A, D and E, implemented in the new configuration, and their respective dimensions (width and height). The blue circle represents the 10-cm radius head model (scalp domain). Image is not shown to scale.

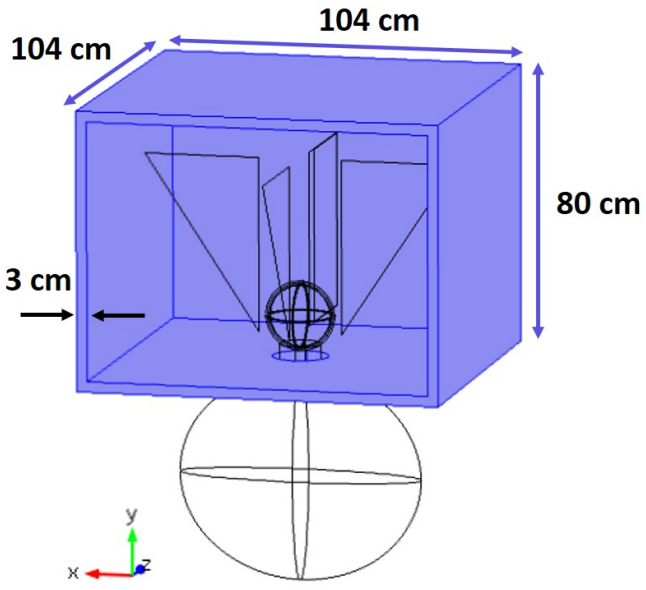

Figure 3.13: Schematics of the shielding structure surrounding the 5-coil system and the patient head. The 3-cm thick metal cage is positioned all around the conducting liquid container (not shown) at a distance of 2 cm.

3.4.2 Patient safety

Throughout the several steps required to find a new and safe OC, particular attention was paid not only to the induced $\vec{J}$ in the heart of the patient but also to the RI at the centre of the brain, since the goal was to keep the deep-brain stimulation capability of the OC while guaranteeing the patient safety.

Optimising coil design and currents

The first attempt to reduce the induction in the heart tissue was by redesigning the coils, increasing the distance between the patient torso and the coils. Four different configurations (Test i, i=1,2,3,4) were simulated in a 2-m radius world of air, combining rectangular and triangular coils with identical size to the coils presented in Figure 3.12. The currents used were similar to the ones used in the previous OC, indicated in Figure 3.4. All the simulations were performed using the same mesh size *Finer*.

The images below illustrate each coil geometry tested, except the last design (Test 4) which was adopted as the new OC and is already depicted in Figures 3.11 and 3.12. The respective results, of all the four geometries, are presented in Table 3.6.

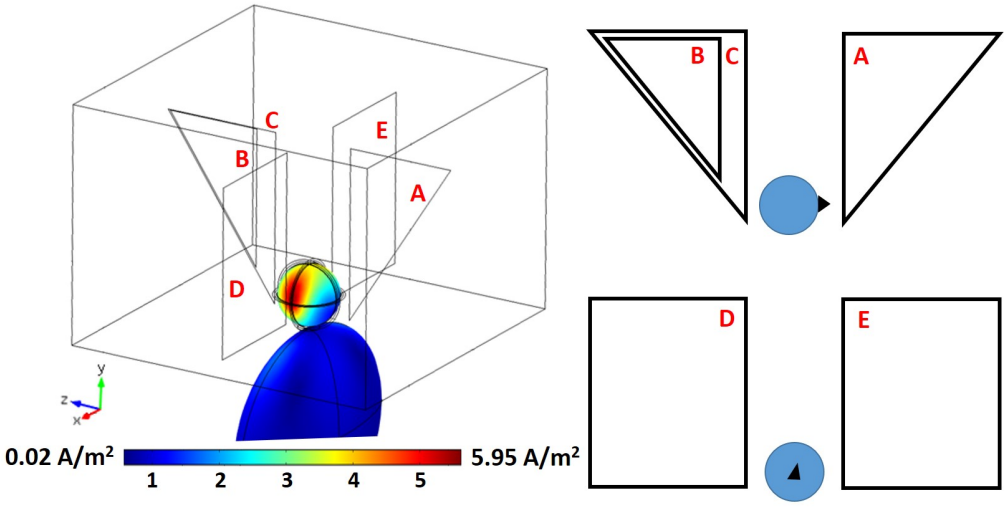

Figure 3.14: Test 1: three triangular coils positioned posteriorly (B and C) and anteriorly (A) in respect to the patient and two rectangular coils located on each side of the patient head (D and E). On the left image, the 5 coils are placed within the conducting liquid container around the patient head. Distribution (colour scale) of the induced current density in the brain and torso is also presented.

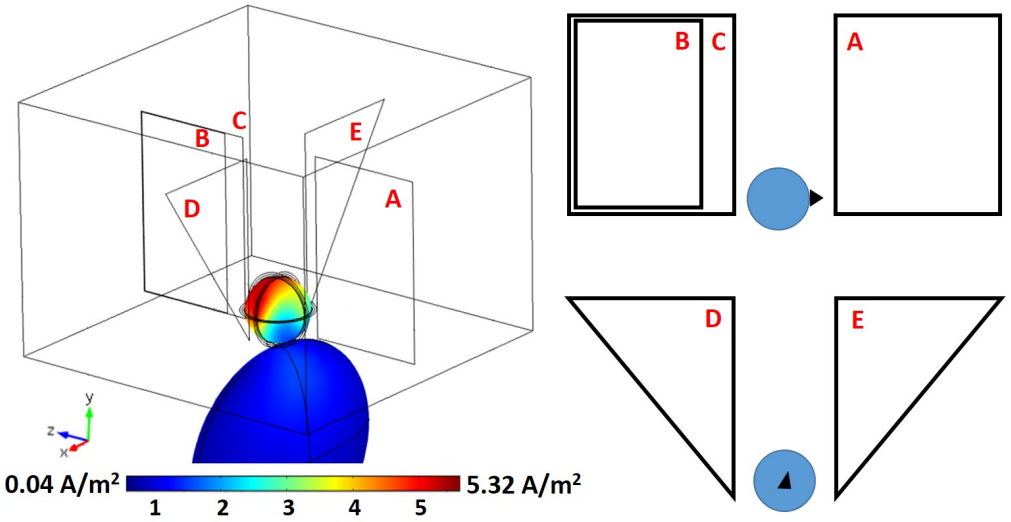

Figure 3.15: Test 2: three rectangular coils positioned posteriorly (B and C) and anteriorly (A) in respect to the patient. Two triangular coils placed on each side of the patient head (D and E). On the left image, the 5 coils are placed within the conducting liquid container around the patient head. Distribution (colour scale) of the induced current density in the brain and torso is also presented.

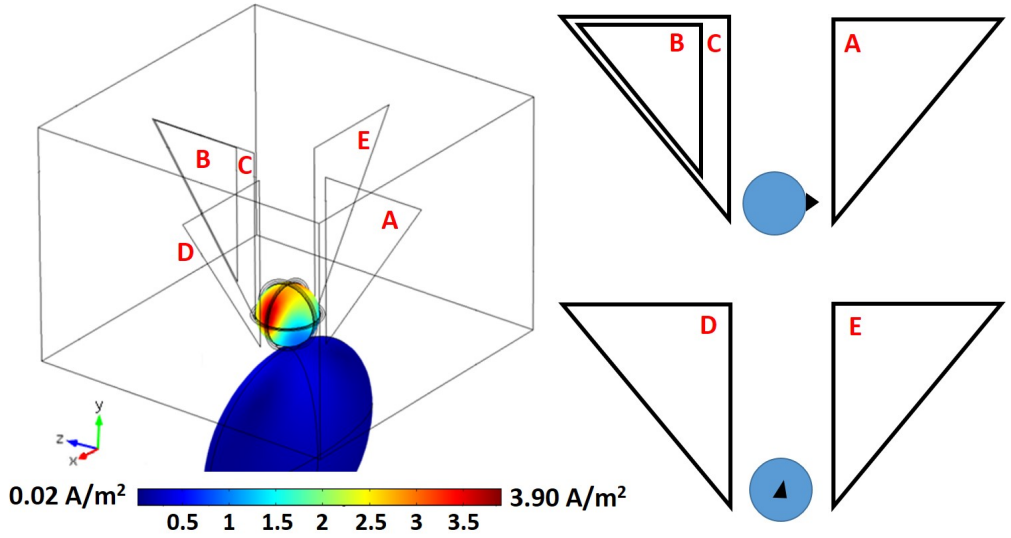

Figure 3.16: Test 3: all the five triangular coils placed perpendicularly around the head model. On the left image, the 5 coils are placed within the conducting liquid container. Distribution (colour scale) of the induced current density in the brain and torso is also presented.

As expected, the configuration Test 3 allows for the minimum induced $\vec{J}$ value in the heart, because all the 5 coils are triangular and thus the distance between the current sources and the torso is maximised, leading to inferior induction power in the patient torso. However, the RI at the brain centre for this geometry is rather inferior when compared to the RI of the last tested design (Test 4).

Table 3.6: Current density values (A/m^2) in the patient brain and torso by four different configurations. RI: relative induction in respect to the surface maximum.

Configuration	Brain volume (A/m^2)			Torso volume (A/m^2)		
	Max	**Min**	**Centre | RI (%)**	**Max**	**Min**	**Heart**
Test 1	5.948	0.766	2.624 | 44.1	1.403	0.021	0.215
Test 2	5.320	1.011	2.970 | 55.8	1.216	0.044	0.227
Test 3	3.902	0.877	1.740 | 44.6	0.410	0.022	0.072
Test 4	5.402	1.087	3.197 | 59.2	1.111	0.059	0.199

Consequently, the Test 4 design was chosen since it yields the best compromise between the currents induced in the brain centre and in the heart. When compared with the previous OC, which had only rectangular coils, the $\vec{J}$ induced in the heart by this new design, is reduced almost 60 % in respect to the 0.47 A/m^2, induced by the former configuration. Nonetheless, such reduction is still not sufficient to attain the safety threshold of 4.5 mA/m^2.

With the modification of the system geometry, the preceding ratio between the currents on each coil might no longer be the most appropriate. Therefore, a study was carried out in order to optimise the currents on each coil, taking as a starting point the currents used in the previous OC, ($I_A = 0.75I_0$, $I_B = -4I_0$, $I_C = I_0$, $I_D = I_E = -I_0$), defined in Section 3.3.2. The simulation results are presented in Table 3.7

From the results it was seen that altering the currents of the rectangular coils (B and C) does not improve the RI at the brain centre. In addition, changing the current of the lateral coils (D and E) was already proved, by previous collaborative work, to have a minor effect over the distribution of the $\vec{J}$ in the brain volume.

However, by decreasing the current passing through the coil A from $0.75I_0$ to $0.3I_0$, keeping the other currents unchanged, it was possible not only to increase the RI at the centre of the brain to an unprecedented value of above 60 %, but also to reduce even further the $\vec{J}$ value in the patient heart, which was decreased by 32 % in respect to the previous optimisation step.

Thus, the optimised current ratio for the new OC was set as follows: $I_A = 0.3I_0$, $I_B = -4I_0$, $I_C = I_0$, $I_D = I_E = -I_0$, which corresponds to the values indicated in

Table 3.7: Current density (A/m^2) induced in the patient brain and torso by different current ratios. For each case, the modification made to the previous current ratio is indicated in the first column. RI: relative induction in respect to the surface maximum. I_i : current passing through coil i.

Modification	Brain volume (A/m^2)			Torso volume (A/m^2)		
	Max	Min	Centre | RI (%)	Max	Min	Heart
$I_A = 0.5I_0$	5.397	1.022	3.223 | 59.7	1.080	0.057	0.197
$I_A = 0.3I_0$	5.397	1.039	3.254 | 60.3	0.948	0.034	0.135
$I_A = 0.5I_0$; $I_B = -2I_0$	3.702	0.279	1.286 | 34.7	0.3142	0.020	0.059
$I_{A,C} = 0.5I_0$; $I_B = -2I_0$	4.249	0.652	2.206 | 51.9	0.5193	0.014	0.088
$I_{A,C} = 0.5I_0$; $I_B = -2.5I_0$	4.646	0.840	2.695 | 58.0	0.744	0.042	0.146
$I_C = 0.75I_0$; $I_B = -2.5I_0$	4.262	0.740	2.192 | 51.4	0.6058	0.015	0.121
$I_A = 0.5I_0$; $I_B = -2.5I_0$ $I_C = 0.75I_0$	4.320	0.653	2.224 | 51.5	0.575	0.026	0.114
$I_C = 0.5I_0$; $I_B = -2.5I_0$	4.594	0.922	2.664 | 58.0	0.7758	0.027	0.144
$I_A = 0.25I_0$; $I_B = -2.5I_0$ $I_C = 0.5I_0$	4.711	0.889	2.748 | 58.3	0.713	0.043	0.135
$I_A = 0.5I_0$; $I_B = -3I_0$ $I_C = 0.8I_0$	4.653	0.803	2.618 | 56.3	0.766	0.049	0.140
$I_A = 0.5I_0$; $I_B = -3.5I_0$	4.796	0.841	2.732 | 57.0	0.855	0.054	0.174
$I_A = 0.5I_0$; $I_B = -3.5I_0$ $I_C = 0.75I_0$	5.428	1.024	3.203 | 59.0	1.025	0.049	0.190

Figure 3.11, where I_0 was considered as 3184 A.

The influence of the size of the fibreglass container was also investigated. Reducing the size of the container worsened the RI at the centre of the brain. Increasing the volume of the conducting liquid from the current 618 L to 1575 L only allowed for an increase of about 1 % in the RI at the brain centre. It is believed, however, that such small increment does not compensate the significantly increased cost associated with the amount of conducting liquid necessary and the much larger space required to install the proposed system, intended for clinical environments where the lack of available spaces is quite common.

Consequently, the dimensions of the fibreglass container used for the new OC remain unchanged.

Implementing a shielding structure

As seen by the aforementioned optimisation studies, and despite the induced $\vec{J}$ in the heart having decreased (71 % in respect to the value obtained with the previous OC), such reduction was insufficient in order to attain the safety threshold of 4.5 mA/m^2.

Consequently, a shielding barrier was proposed, to be located between the 5-coil system and the patient torso in order to significantly decrease the induction power of the new OC in the patient heart tissue.

The attenuation of the B-field is related with the properties of the barrier material such as its electrical conductivity, thickness, size and distance from the source of the B-field (Čuntala, 2006). Increasing the distance between the EMF source and the sensitive volume can be a good shielding method as seen by the results presented in Table 3.3. Nevertheless, it is not a valid alternative for the patient which can not be moved away from the 5-coil system.

For static or slowly varying ($<$ 100 kHz) B-fields, passive magnetic shielding can be attained by a conductive, high-permeability metal or alloy, such as iron. This type of shielding, however, does not block or stop the B-field, since B-field lines can only be redirected, not created or removed, by the ferromagnetic material. Such barrier rather draws the B-field into itself, providing a least magnetic reluctance path for the B-field lines, thus diverting the magnetic energy through itself (Magnetic Shield Corporation, 2014). As a result the B-field is attenuated around the shield, since the B-field lines become less concentrated in the surrounding area (Less EMF Inc., 2015).

With this in mind, and in order to place the metal slab between the coils and the torso, it was necessary to consider a neck for the patient model. This extra domain enabled a simulation of a more realistic human model with the shielding barrier closing around the neck, as seen in Figure 3.17. The minimum distance between the neck and the metal was defined as 2 cm, to avoid direct contact between the skin and the highly conductive material, in which the induced $\vec{J}$ can go up to 10^6 A/m^2. A more detailed view of the neck domain can be seen in Appendix VI as well as the

simulation results proving that the implementation of such domain does not affect the induced $\vec{J}$ distribution in the brain volume.

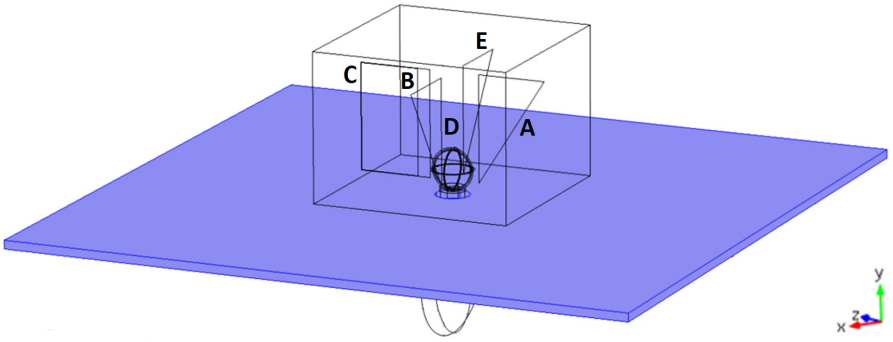

Figure 3.17: Schematic representation of a 4-cm thick metal slab (3×3 m^2), positioned above the patient torso, 2 cm below the fibreglass container. The shield has a circular opening allowing for the head to get through. The conducting liquid container as well as the optimised design of the 5 coils are also illustrated.

Such simulation studies, involving materials with high electrical conductivity and relative permeability, had never been tried before and at the beginning the simulation software could not converge to a solution whenever this kind of materials was included in the simulation model. Thus, it was necessary to modify a specific parameter, termed *Drop tolerance*, which controls the number of elements neglected by the software in the calculations. For more details about this parameter, namely on how it can be altered, see Appendix IV. The most refined mesh used when simulating a shielding material was the mesh size *Fine* with a maximum number of tetrahedral first order elements of about 135,000. Finer meshes, yielding a higher number of elements, cause the software to fail when converging to the solution.

Additionally, to simplify even further the model, by decreasing the number of elements in the mesh, the conducting liquid domain was not considered for the shielding simulation studies. This assumption resulted from a study proving that the presence of the conducting liquid is not relevant to the $\vec{J}$ distribution in the patient torso. Results are presented in Appendix VI.

The first approach consisted of placing an iron slab 4 cm below the fibreglass container. However, when the metal was positioned nearer the container, namely at 2 cm, the B-field became more attenuated resulting in a decrease of the $\vec{J}$ value observed in the patient torso. This simulation results are also discussed in Appendix

VI. Subsequently, all the following studies were performed with the shield located 2 cm below the container.

Iron and aluminium as shielding materials

After designing the shielding structure, in the COMSOL® AC/DC software, with the proper dimensions, a new domain was automatically created which then should be characterised by assigning it the respective physical properties (σ, ε_r and μ_r).

Iron was the first material to be simulated because it is ferromagnetic and thus, is capable of providing an effective passive magnetic shielding with a relatively low cost.

Nonetheless, another highly conductive material was considered for the shielding structure. Aluminium, although it is not a ferromagnetic metal, has an extremely high σ, about 3 times the conductivity of iron and therefore was also capable of reducing the induced $\vec{J}$ in the patient torso.

The shielding performed by the aluminium slab is not, however, the same passive magnetic shielding observed for the iron, mainly because the μ_r of aluminium is equal to 1, the same as air or biological tissues. Consequently, it can not attract the B-field lines to itself like the iron does. What seems to be happening is that the aluminium is capable of attenuating the B-field by means of its high σ. The transient, increasing B-field generates eddy currents in the aluminium which are strong enough to produce a secondary opposing B-field which acts to cancel or partially attenuate the incident primary B-field (Magnetic Shield Corporation, 2014). Despite this radio frequency (RF) shielding will typically occur for higher frequencies, of 100 kHz and above, it also seems to be occurring in the attenuation of the 5 kHz transient B-field, when considering aluminium as the shielding material.

The properties used to implement the iron and aluminium are presented in Table 3.8 and were obtained from the *Material Browser* available in COMSOL® AC/DC. This list of materials can be accessed as explained in Appendix IV.

Furthermore, another interesting and unexpected observation was the fact that the simulation results are quite identical when considering iron or aluminium as the

Table 3.8: Physical properties of iron and aluminium considered for the shielding material. σ: electrical conductivity. ε_r: relative permittivity. μ_r: relative permeability. ρ: density.

Metal	$\boldsymbol{\sigma}$ **(S/m)**	$\boldsymbol{\varepsilon_r}$	$\boldsymbol{\mu_r}$	$\boldsymbol{\rho}$ **(kg/m^3)**
Iron	$1.120 \cdot 10^7$	1	4000	7870
Aluminium	$3.774 \cdot 10^7$	1	1	2700

shielding material. This was observed when simulating the previous OC and the new optimised design. Results are described in Appendix VI.

Similar results were also obtained when simulating a nickel-iron alloy, termed Mu-Metal, which is commonly used to shield static or slowly varying B-fields (Magnetic Shield Corporation, 2014). These were just first estimates and further simulations with Mu-Metal or other shielding alloys falls out of the scope of this dissertation. Choosing the most appropriate material and the respective optimisation should be performed in future work.

Henceforth, iron was considered as the shielding material in the following simulation studies.

Optimisation of the iron slab: size and thickness

In order to reduce the weight of the iron slab, a study was performed, investigating the influence of considering thinner and smaller shielding slabs over the induced $\vec{J}$ distribution in the patient torso.

Regarding the thickness of the structure, several square iron slabs (3×3 m^2) were simulated having different thicknesses ranging from 4 cm to only 0.5 cm. The optimised coil geometry and currents were used for all the simulations. Such results are presented in Table 3.9.

As demonstrated by the simulation results, the maximum $\vec{J}$ value induced in the torso volume had an expected behaviour, increasing as the iron slab was getting thinner.

Nonetheless, aiming at the 4.5 mA/m^2 safety threshold, one can see that only the 4-cm and 2-cm thick slabs allow for an induction in the heart below the adopted safety limit.

Table 3.9: Current density values in the patient torso, located behind a (3×3 m^2) iron slab with variable thickness. The mesh used for each case and the number of elements calculated are also presented.

Thickness (cm)	Mesh	No. elements	Torso volume (A/m^2)		
			Max	Min	Heart
4	Normal	39,046	0.178	$1.212 \cdot 10^{-4}$	$4.090 \cdot 10^{-3}$
4	Fine	120,920	0.293	$4.584 \cdot 10^{-4}$	$4.173 \cdot 10^{-3}$
3	Normal	33,226	0.206	$3.653 \cdot 10^{-4}$	$5.850 \cdot 10^{-3}$
2	Normal	36,640	0.283	$3.150 \cdot 10^{-4}$	$3.390 \cdot 10^{-3}$
2	Fine	134,319	0.379	$6.711 \cdot 10^{-4}$	$7.747 \cdot 10^{-3}$
1	Normal	40,978	0.307	$9.891 \cdot 10^{-4}$	$7.290 \cdot 10^{-3}$
0.5	Normal	46,764	0.366	$5.360 \cdot 10^{-4}$	$5.280 \cdot 10^{-3}$

To make sure that such results can be trustworthy, two additional simulations were done using the aforementioned slabs but with a more refined mesh (*Fine*).

Attending at the $\vec{J}$ value in the heart of the patient and comparing the results obtained by the two meshes it is possible to conclude that for the 2-cm thick slab, the results can not be considered as valid, since $\delta x = 56.2$ %, clearly surpassing the 10 % acceptance limit.

For the 4-cm thick iron slab, however, the induction in the heart tissue remained constant even when considering a finer mesh with more elements. As confirmed by the δx of 2 %, these results can be trusted and the optimum value, so far, for the $\vec{J}$ in the heart is assumed to be approximately 4.2 mA/m^2.

The next optimisation step involved the size of the 4-cm thick iron slab, again with the purpose to reduce the overall size and weight of the shield.

Figure 3.18 shows the variation of the $\vec{J}$ values in the patient heart as a function of the dimension of the side of the square slab.

As expected, for a wider slab the number of B-field lines intersecting the shielding structure is higher and thus, the attenuation power of the metal structure increases. From this study, one can see that in order to meet the adopted safety threshold, the square iron slab must have at least a 3-m side.

The role of the iron slab in the attenuation of the B-field can be quantified by the ratio between the $\vec{J}$ induced in the heart with and without the shielding, while

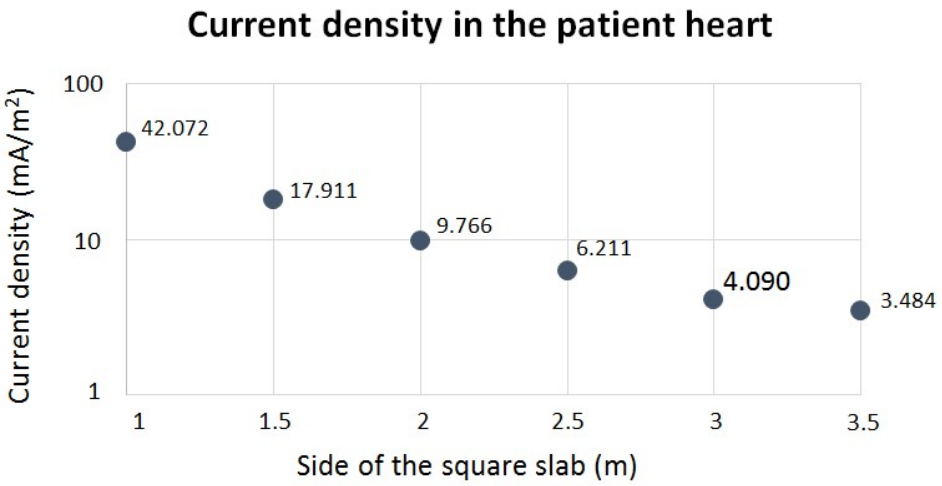

Figure 3.18: Behaviour of the induced current density, $\vec{J}$, in the heart of the patient which is protected by an iron slab of variable size. The side of the square slab ranged from 1 m to 3.5 m. For better visualisation, the vertical axis is represented in logarithmic scale. Note that the $\vec{J}$ values are displayed in mA/m^2.

maintaining all the other parameters constant. This ratio is known as the Shielding Factor (S) and it is defined as follows:

$$S = \frac{\|\vec{J}\, without\, shielding\|}{\|\vec{J}\, with\, shielding\|} \tag{3.2}$$

Considering the values without and with shielding from Tables 3.7 and 3.9, respectively, the shielding factor for the optimised iron slab is given by $S = 0.135\,/\,4.173 \cdot 10^{-3} = 32.4$.

The possible influence of having a metal structure, on the distribution of the $\vec{J}$ induced in the brain volume was also investigated. By simulating the new OC, immersed in conducting liquid, with the optimised iron slab placed below the container, it was found that the inclusion of the metal had no significant effect neither on the value of the $\vec{J}$ at the centre of the brain ($\delta x = 0.4$ %) nor on the RI value ($\delta x = 3.3$ %). Such observation can be justified by the fact that the induced currents in the brain mainly depend on the conducting solution in which the head is immersed, and thus, it is not influenced by the shield.

3.4.3 Operator safety

To allow for a system operator or nursing staff to be positioned near the patient, thus behind the iron slab, a simulation study was performed with an ellipsoidal torso located at 10 cm and 100 cm from the patient back, as seen in Figure 3.19.

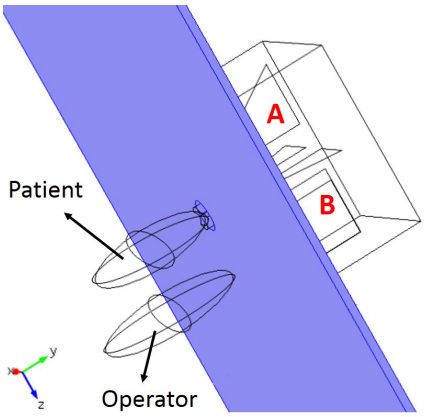

Figure 3.19: Schematic representation of the patient and an operator located behind the iron slab. The operator is placed right next to the metal slab, not in direct contact, and at 10 cm from the patient back. Coils A and B are also indicated.

For both cases, the induced $\vec{J}$ in the heart of the operator lies below the safety threshold, being equal to 4.4 mA/m^2 and 4.2 mA/m^2 for the operator located at 10 cm and 100 cm from the patient, respectively. Therefore, there are no safety restrictions on being close to the patient, as long as the the operator/nurse remains behind the iron slab and thus shielded against the transient B-field.

Next, the protection of an operator, located not behind but above the metal slab, by means of distance and shielding is discussed.

Protection of the operator by means of distance

Similarly to what was done with the previous OC in Figure 3.9, three ellipsoidal torsos were also positioned sideways to the new dTMS configuration on the same positions in respect to the patient (anterior, lateral and posterior) in order to determine the magnitude of the induced $\vec{J}$ in the heart of an operator placed sideways to the container. In addition, a fourth ellipsoidal torso was also considered on the opposite side of the patient, on the top of the fibreglass container, in order to cover all the possible directions around the 5-coil system.

All the four torsos were placed very close to the container, without touching it, to obtain the maximum induced $\vec{J}$ value for each position. These simulations were performed with the optimised new OC but without the iron slab since the shield would not have had any influence over the induced currents in the operators torso. Results are presented in Table 3.10.

Table 3.10: Current density (A/m^2) induced in the torso volume of four operators located anteriorly, posteriorly, laterally and on the opposite side of the patient (top position), very close to the container.

Position	**Torso volume (A/m^2)**		
	Max	**Min**	**Heart**
Anterior	1.090	0.040	0.186
Lateral	1.464	0.062	0.397
Posterior	18.956	0.508	3.193
Top	1.183	0.068	0.321

This simulation study confirmed that, as expected, the torso located posteriorly, in respect to the patient, experiences the highest induced $\vec{J}$ due to the increased current intensity passing through coil B.

Therefore, further studies only considered this posteriorly located torso, because it represents the worst case scenario and by guaranteeing its safety, the safety of an operator located in any of the remaining positions, all around the container, is also assured.

Table 3.11 presents the values of the induced $\vec{J}$ in the posterior torso, located at different distances from the fibreglass container in order to determine the minimum safety distance for an operator located posteriorly, behind coils B and C.

At a minimum distance of 2 m from the fibreglass container, the safety of the operator is guaranteed, regardless of its position relatively to the new OC.

Protection of the operator by means of shielding

After establishing the minimum safety distance, a fully closed metallic structure was suggested, with the purpose to allow any system operator or nursing staff to be anywhere in the dTMS system surroundings without worrying about safety

Table 3.11: Current density values (A/m^2) in the torso volume of an operator located in a posterior position, at different distances from the container.

Distance (cm)	Torso volume (A/m^2)		
	Max	**Min**	**Heart**
100	0.070	$3.666 \cdot 10^{-3}$	0.021
150	0.026	$7.057 \cdot 10^{-4}$	$5.595 \cdot 10^{-3}$
200	0.014	$5.108 \cdot 10^{-5}$	$3.760 \cdot 10^{-3}$
250	$9.131 \cdot 10^{-3}$	$2.314 \cdot 10^{-4}$	$2.02 \cdot 10^{-3}$

issues. This iron-based 3-cm thick shielding cage completely encloses the container as illustrated in Figure 3.13.

Before assessing the effects of such shield on the operator torso, a simulation study was performed to investigate the attenuation of the $\vec{J}$ in the patient heart as a result of the shielding capability of the new proposed structure. Results can be found in Table 3.12.

Table 3.12: Induced current density in the heart of the patient, the latter shielded by a metal cage fully enclosing the conducting liquid container. The mesh and number of elements calculated for each simulation are also described.

Mesh	No. elements	Torso volume (A/m^2)		
		Max	**Min**	**Heart**
Normal	23,236	0.204	$8.579 \cdot 10^{-5}$	$2.467 \cdot 10^{-3}$
Fine	82,901	0.433	$1.195 \cdot 10^{-4}$	$3.115 \cdot 10^{-3}$
Fine	131,898	0.435	$1.196 \cdot 10^{-4}$	$3.072 \cdot 10^{-3}$

Once again, to determine whether one can rely on the obtained results, the relative errors between the three simulations were calculated. As seen by the values in Table 3.12, the difference between the first and second simulation was quite significant regarding the induced $\vec{J}$ in the heart of the patient, yielding an unacceptable δx of 20.8 %.

However, between the two meshes *Fine*, the relative error for the $\vec{J}$ value observed in the patient heart is only 1.4 %, which makes these results trustworthy. Consequently, the proposed metal cage, surrounding the 5-coil system, provides

the best attenuation power, so far, which is reflected by its shielding factor: $S = 0.135 \,/\, 3.072 \cdot 10^{-3} = 43.9$.

Regarding the capability of this new proposed shield to protect the system operator, two simulations were carried out with an ellipsoidal torso located posteriorly to the patient. The torso volume was placed, at first, 100 cm apart from the metal cage and then practically next to the same shielding structure, without touching it.

Table 3.13 presents the simulation results obtained for each situation.

Table 3.13: Current density values (A/m^2) in the torso volume of an operator located in a posterior position, when placed right next to the metal cage and 100 cm apart.

Distance (cm)	**Torso volume (A/m^2)**		
	Max	**Min**	**Heart**
≈ 0	$6.282 \cdot 10^{-3}$	$9.421 \cdot 10^{-5}$	$7.898 \cdot 10^{-4}$
100	$3.373 \cdot 10^{-5}$	$1.291 \cdot 10^{-6}$	$6.426 \cdot 10^{-6}$

From these promising results, one can conclude that the metal cage is extremely effective in attenuating the varying B-field produced by the 5 coils of the new OC. Considering the worst case scenario, when the operator is located next to the shield, behind coils B and C, the $\vec{J}$ in the heart of the operator not even reaches 1 mA/m^2, being clearly inferior to the accepted safety threshold.

The distribution of the induced $\vec{J}$ in the operator torso, placed very close to the shielding structure, is shown in Figure 3.20. The direction of the induced $\vec{J}$ is the same of the current circulating in the coil B, as expected, since the coils are immersed in conducting liquid.

By evaluating the magnetic flux density outside the fibreglass container, with the metal cage surrounding the new OC, it is possible to see that the B-field is attenuated, at least, by three orders of magnitude, comparing with the situation where there is no shielding protecting the operator. Such results are illustrated in Appendix VII.

It is important to point out, though, that the B-field lines resist in making sharp turns and therefore, the edges of the proposed structure (see Figure 3.13) should

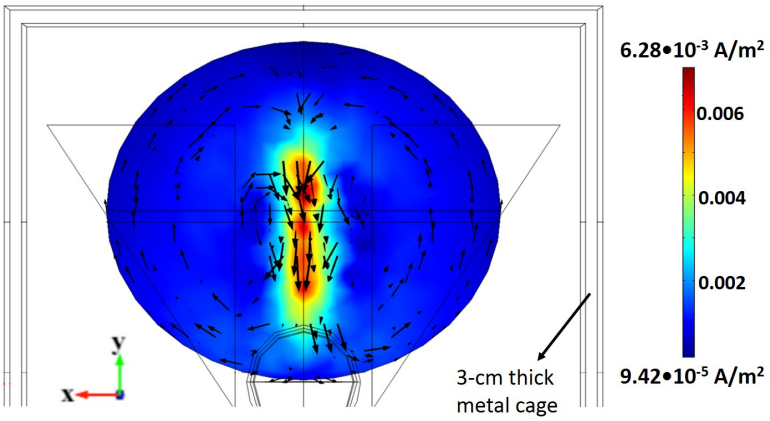

Figure 3.20: Distribution (colour scale) and direction (arrows) of the induced current density in an ellipsoidal torso placed next to the metal cage, in a posterior position (behind coils B and C). Coils D and E are indicated. For better visualisation, the arrows are represented in logarithmic scale.

be smoothed rather than having sharp creases, in order to improve its shielding efficiency, if needed.

Safety concerns regarding the future experimental validation tests

In order to validate all the simulation studies performed so far, future experimental tests will have to be carried out in order to confirm the results obtained through the COMSOL® AC/DC software.

LIP already has one magnetic stimulator available, capable of feeding the 5-coils system. In this section a study is presented where $I_A = I_0$ so that the 3 kA provided by the stimulator may be used. Despite this value being 3 times larger than the necessary stimulator current, it allows to study the distance necessary to protect the induction of heart fibrillation. Thus, the experimental currents must be related as follows: $I_A = I_0$, $I_B = -12I_0$, $I_C = 3I_0$, $I_D = I_E = -3I_0$, where I_0 is the output current provided by the stimulator. As a result, coil A will have only one turn, coil B will have 12 turns and coils D, C and E will be comprised of 3 turns of wire each.

Since the currents will be increased 3 times, comparing with the optimised ratio, a simulation study was conducted to determine the minimum safety distance that must be considered in the experimental tests. Results are depicted in the chart of Figure 3.21, which demonstrates the decrease of the $\vec{J}$ in the operator heart with the distance from the container.

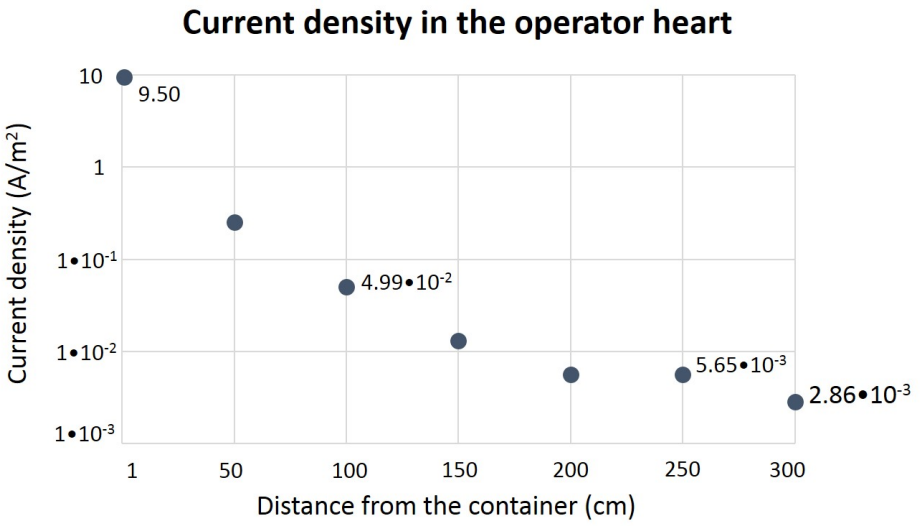

Figure 3.21: Behaviour of the induced current density, $\vec{J}$, in the heart of the operator which is posteriorly located, as a function of the distance between the torso and the fibreglass container. For better visualisation, the vertical axis is represented in logarithmic scale. Note that the $\vec{J}$ values are displayed in A/m^2.

Only for distances greater or equal than 3 m, the $\vec{J}$ in the heart of the operator drops to an acceptable value of about 3 mA/m^2.

However, if the proposed metal cage is implemented, this safety distance restriction no longer applies.

The potential cost of the fully closed shielding structure was also determined. The metal cage not only reduced even further the $\vec{J}$ induced in the heart of the patient and the operator but also allowed for a more economic solution, using less than half of the amount of metal needed, when comparing with the metal slab. Table 3.14 summarises the data on the cost of the shielding structure.

Table 3.14: Cost of a potential shielding structure to be implemented in the future. Results are presented both for iron and aluminium. Information about the price of the material was kindly provided by the workshop staff at LIP.

Structure	Metal	Total weight (kg)	Price (€/kg)	Total cost (€)
Cage	Iron	1,211.8	1.5	1,817.8
	Aluminium	415.8	6.0	2,494.5
Slab	Iron	2,828.5	1.5	4,242.7
	Aluminium	970.4	6.0	5,822.3

Considering the results in Table 3.14, a metal cage made of iron seems a valid

option, to be implemented as a shielding structure, for the experimental validation tests, since it is the more economic solution. Nevertheless, the aluminium provides a much lighter structure, with less than half of the weight of the iron cage, being a more suitable alternative to shield a future system, intended for clinical environments.

3.4.4 Optimum results

After the described optimisation process, a new dTMS system was proposed, capable of achieving more than 60 % RI at the centre of the brain (10-cm depth), while guaranteeing the safety of the patient and of any operator/nursing staff that can, now, be positioned anywhere in the 5-coil system surroundings. The system of coils and the respective shielding structure are illustrated in Figure 3.11 and Figure 3.13.

The distribution of the induced $\vec{J}$ obtained after simulating the new OC surrounded by a 2-m radius sphere of air is illustrated in Figure 3.22.

In Appendix VIII, the distribution of the $\vec{J}$ induced in the remaining domains (scalp, skull, CSF and conducting liquid), is also illustrated.

The values of the induced $\vec{J}$ in the patient and in the operator are summarised in Tables 3.15 and 3.16. The values presented for the operator were induced in a torso volume, posteriorly located, right behind the shielding metal cage.

Table 3.15: Induced current density (A/m^2) values for the patient brain, after optimising the new 5-coil dTMS system and its shielding structure.

Brain volume (A/m^2)			
Max	**Min**	**Centre | RI (%)**	**Retina | RI (%)**
5.397	1.039	3.254 | 60.3 (%)	1.735 | 32.1 (%)

Table 3.16: Induced current density (A/m^2) values for the patient and operator torso, after optimising the new 5-coil dTMS system and its shielding structure.

	Torso volume (A/m^2)		
	Max	**Min**	**Heart**
Patient	0.435	$1.196 \cdot 10^{-4}$	$3.072 \cdot 10^{-3}$
Operator	$6.282 \cdot 10^{-3}$	$9.421 \cdot 10^{-5}$	$7.898 \cdot 10^{-4}$

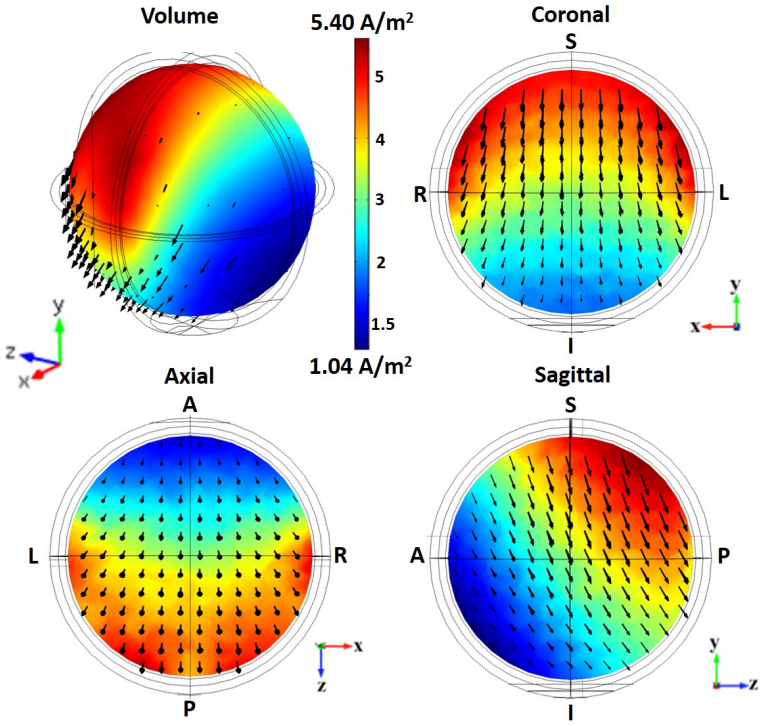

Figure 3.22: Distribution (colour scale) and direction (arrows) of the induced current density represented in a three-dimensional view and central slices (coronal, axial and sagittal) of the brain volume. The illustrated stimulation was performed having the 5-coils and the head model immersed in conducting liquid and the whole system surrounded by a 2-m radius spherical volume of air. A: anterior. P: posterior. L: left. R: right. S: superior. I: inferior.

The maximum current density of 5.40 A/m^2 is in compliance with the cortical activation threshold of 6 A/m^2, defined for frequencies in the kHz range. Since the effects of $\vec{J}$ values higher than this maximum threshold on cortical brain regions are yet not fully understood, the superficial maximum current density induced by the presented 5-coil configuration should not be much higher than the 6 A/m^2 limit. If needed, in order to reach the 6 A/m^2 threshold, one must simply increase the current I_0 and, therefore the current on the five coils also increases by the same amount, leading to a higher $\vec{J}$ in the brain volume.

Regarding the value of the $\vec{J}$ in the retina, induced by the new OC, it is clear that it surpasses the adopted threshold for the induction of magnetophosphenes (1 A/m^2). Since the threshold for cortical stimulation lies at 6 A/m^2 for the kHz range, as explained in Section 2.3.3, the relative induction in the retina should be equal or inferior than 16 % ($1/6 \simeq 16\%$).

Nevertheless, the evaluation of the induced $\vec{J}$ in the retina was performed in the brain volume (homogeneous medium with an electrical conductivity of 0.33 S/m), since the eyes were considered within the brain model and not as individualised tissues. The position of the retinas, located within the head model used for this work, was determined by the method described in Appendix III.

The eyes, despite being quite conductive, are surrounded by low-conductivity tissues such as fat, muscle and skull (Laakso and Hirata, 2012). Consequently, the $\vec{J}$ induced by the new OC in the retinas will most likely be inferior to the values obtained from simulation, since the latter were measured in a relatively conductive medium, making this evaluation method quite conservative.

Additionally, the adopted threshold of 1 A/m^2 resulted from a conservative extrapolation over experimental data measured at much lower frequencies than the frequency range considered in this work. This also supports the conclusion that the $\vec{J}$ obtained in the retinas might be acceptable, considering the risk/benefit ratio resulting from the high RI at the centre of the brain.

However, if the induced currents in the retinas still remain a problem, namely due to the discomfort caused by the magnetophosphenes, there is another alternative solution that can be considered, involving the dTMS protocol being performed under anaesthesia. Some studies have been published where TMS-induced effects were reported in anaesthetised animals (Aydin-Abidin et al., 2006, Bestmann, 2008). In addition, Burke *et al.* also reported motor cortex responses after applying an electrical stimulation protocol in anaesthetised patients. They found that, as expected, the anaesthetic increased the threshold current required to evoke a corticospinal response (Burke et al., 2000). Nonetheless, the electrical stimulation was capable to induce neural responses from corticospinal axons despite the administration of an anaesthetic.

Thus, these findings support the hypothesis that the magnetic stimulation applied via the proposed configuration, will most probably be effective in stimulating the brain tissue even if the patient has to be anaesthetised.

The value of the RI at the centre of the brain, provided by the new OC, constitutes an unprecedented stimulation power in depth, surpassing the

deep-brain stimulation capability of TMS standard coils, like the figure-8 coil and the H-coil (Zangen et al., 2005), as seen in Figure 3.23.

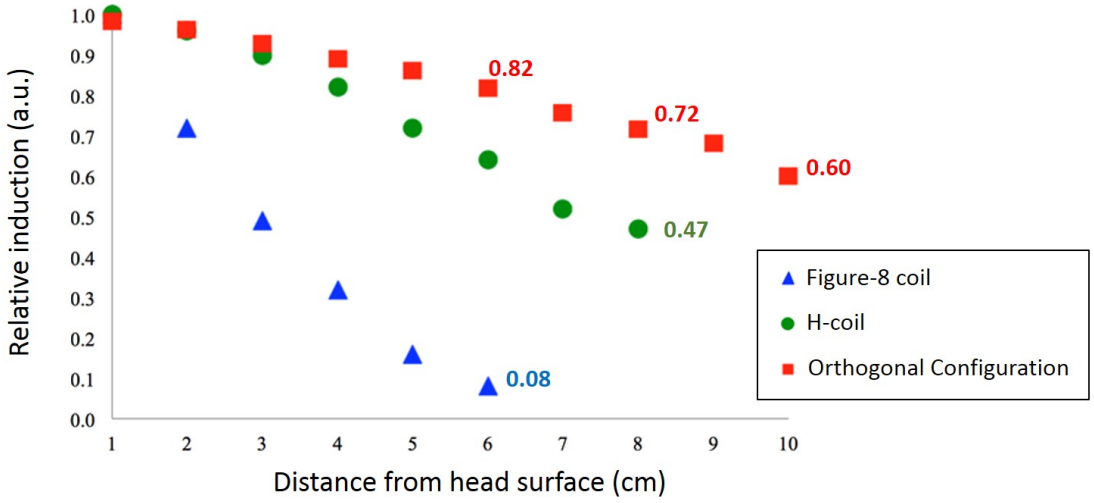

Figure 3.23: Current density induced in a spherical brain model relatively to the surface maximum, as a function of distance, for two standard TMS coils (figure-8 and H-coil) and for the new proposed dTMS system. Data for the standard coils obtained from (Roth and Zangen, 2014*b*).

Reaching 82 % and 72 % of RI at brain depths of 6 cm and 8 cm, respectively, the new OC distinctively overcomes the stimulation capability of both standard TMS coils, in addition to being the only one able to attain a 10-cm brain depth.

As a final remark, all the simulations performed in the scope of this work, including the studies presented in Chapter 4, were conducted considering a bared electric wire for the coils, which, as a result, was in direct contact with the conducting liquid. In order to see the influence of having an insulated wire, which reflects a realistic situation, a study was performed using a small circular coil, positioned over an animal head model.

The main conclusion is that the distribution of the $\vec{J}$ induced in the animal brain model was not significantly affected by the insulation of the wire in the coil, although a slightly decrease of the RI at the centre of the brain was observed. Such results are presented in more detail in Appendix IX. A study on the effects of the insulation of the coils in the new OC must, however, be performed in future work, in order to clarify the influence of this wire insulation in the human model.

3.5 Testing COMSOL Multiphysics® AC/DC shielding results

With the purpose to validate the simulation results obtained with the COMSOL® AC/DC software, namely in respect to the shielding capability of iron and aluminium, experimental tests were conducted, using the built in-house magnetic stimulator available at LIP (Simões et al., 2013).

The construction of such device was based on the battery-powered portable magnetic stimulator developed by Epstein *et al.* (Epstein, 2008). The 7-turn stimulator coil with an inner diameter of 11.5 cm yielded an inductance of about 10 μH, with a current of approximately 3 kA flowing through each turn. The series capacitor bank is capable of fully charging in about 1.2 s, thus allowing a maximum frequency of 0.8 Hz for the delivery of TMS monophasic pulses (Simões et al., 2013). This power electronics system is shown in Figure 3.24.

Experimental data was acquired through a PicoScope® 2203 PC Oscilloscope (Pico Technology Ltd., 2013) complemented by the PicoScope® 6 software (Pico Technology Ltd., 2015) and the consequent processing was done using the MathWorks MATLAB® software (The MathWorks Inc., 2015) (see Appendix I for more details).

3.5.1 Attenuation of the TMS-induced pulse in a saline solution

The first experimental test consisted in measuring the attenuation of the TMS-induced E-field inside a saline solution, with an electrical conductivity of 7 S/m, comprised in a cylindrical container (7-cm radius and 5-cm height). The amount of sodium chloride required to achieve the pretended σ was determined as explained in Appendix X.

A dipole probe was placed at the centre of the cylindrical container, in order to measure the potential difference between two closely spaced points at a distance of 1 cm, therefore providing a indirect readout of the total E-field in the direction of the line joining the two points. The two insulated wires coming out of the probe

were twisted together to prevent the induction of a voltage in the leads by the increasing B-field pulse and then were connected to a high input impedance (GΩ) instrumentation amplifier with a gain of 25.7. The advantage in using such amplifier is that it prevents parasite currents from passing through the probe terminals and the amplifier itself.

The cylindrical container was then positioned behind a 4-mm thick iron slab (20×20 cm^2) and a 25-mm thick aluminium slab (30×22 cm^2) to evaluate the shielding capability of the referred metal barriers.

The whole setup used in this experiment is presented in Figure 3.24.

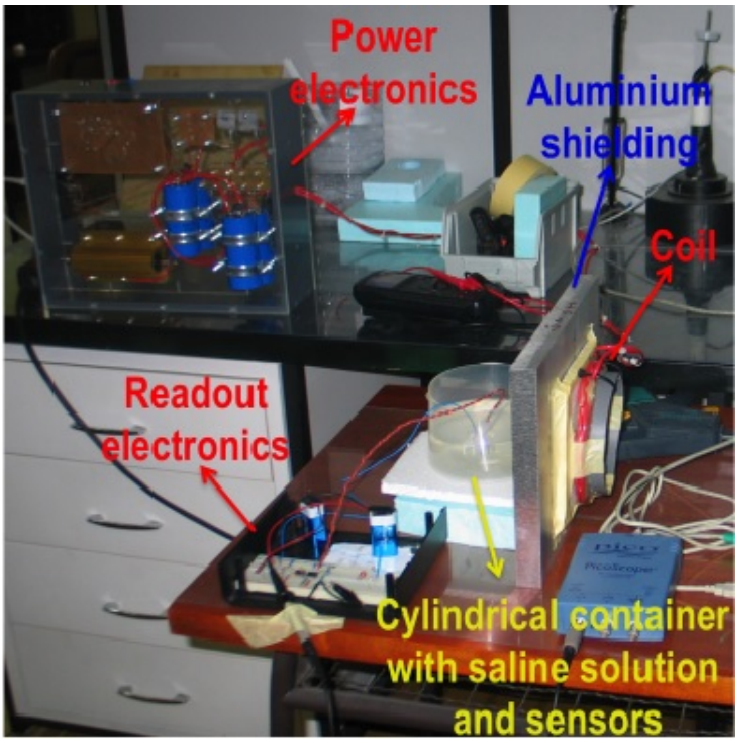

Figure 3.24: Experimental setup used to evaluate the attenuation of the E-field induced in a saline solution by a TMS pulse, delivered by a 7-turn coil positioned tangentially to the container. The 25-mm thick aluminium slab is placed between the TMS coil and the container filled with the conducting solution (7 S/m).

The obtained experimental results are depicted in Figure 3.25, where it is possible to see the monophasic TMS pulses induced in the saline solution.

From the results depicted in Figure 3.25, the 4-mm thick iron slab appears to be able of reducing the induced E-field by approximately 10 times. However, it can be seen that the E-field attenuation capability of aluminium is higher, being almost impossible to distinguish the TMS-induced pulse from the noise inherent to

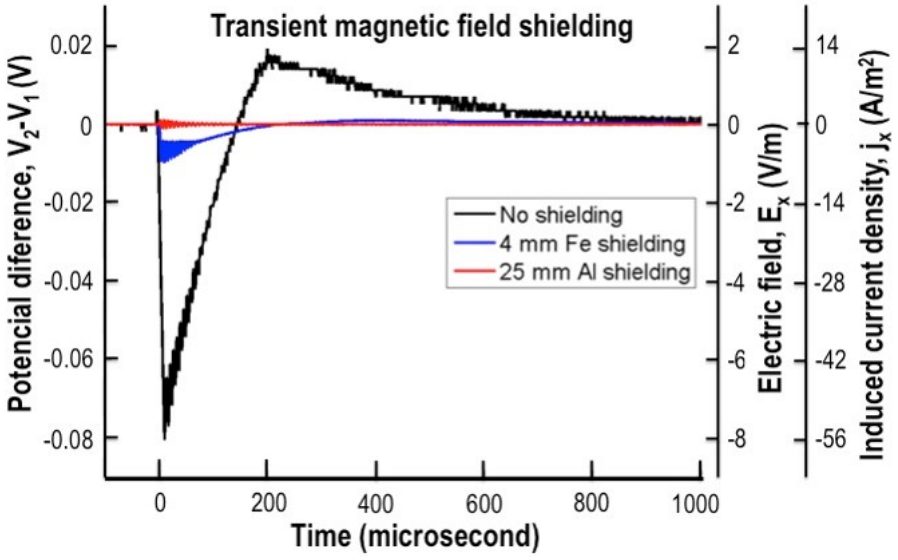

Figure 3.25: Waveforms obtained experimentally without any shielding (black), with iron (blue) and aluminium shielding (red).

the readout electronics. Nevertheless, the aluminium shield attenuates the transient B-field by, at least, two orders of magnitude, when comparing with the case where no shielding barrier was considered.

Simulation study to assess the attenuation of the TMS-induced pulse in a saline solution

After this first experimental test, a COMSOL® AC/DC-based study was conducted to see if the results obtained via simulation translated the same attenuation power of the tested metal barriers.

Therefore, the setup illustrated in Figure 3.26 was simulated while being surrounded by a spherical volume of air. The dimensions of the cylindrical container and the metal slabs were thoroughly replicated as well as the physical properties of each material/solution. The 7-turn circular coil was also modelled with the real 5.75-cm inner radius.

The simulations were done using different meshes, both for iron and aluminium, so that the δx can be calculated for each metal, thus validating, or not, the results obtained. Such results are shown in Table 3.17.

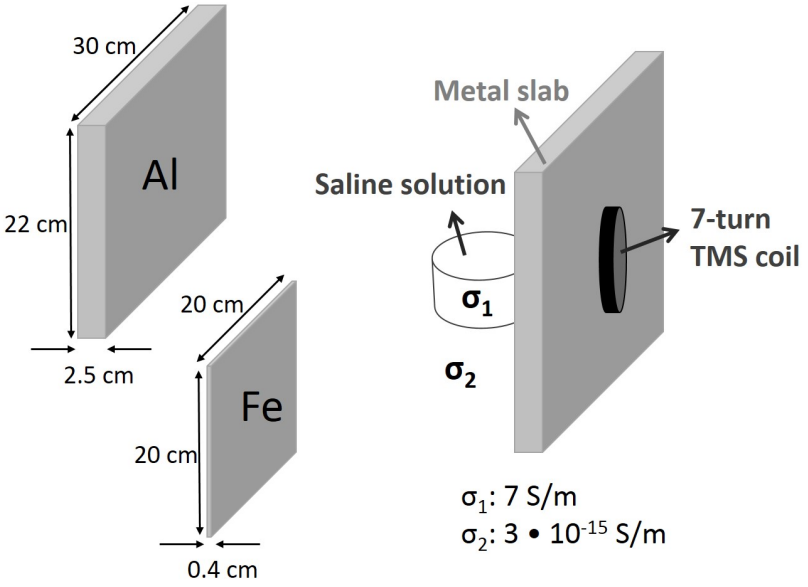

Figure 3.26: Simulation setup used to replicate the experimental test evaluating the capability of two metal slabs in attenuating the TMS-induced pulse in a container filled with saline solution ($\sigma_1 = 7$ S/m). Both the iron (Fe) and the aluminium (Al) slabs were placed between the TMS coil and the current density sensor, located within the container. The whole setup was surrounded by a spherical volume of air ($\sigma_2 = 3 \cdot 10^{-15}$ S/m).

Table 3.17: Induced current density (A/m^2) at the centre and surface of a cylindrical container filled with a saline solution, with and without a metal slab positioned between the container and a 7-turn circular coil. Results are presented for the two used meshes *Fine* and *Finer*.

Metal	**Mesh**	**Without shielding (A/m^2)**		**With shielding (A/m^2)**	
		Max	**Centre**	**Max**	**Centre**
Iron	Fine	624.060	62.227	11.476	1.202
	Finer	631.450	48.518	6.917	0.674
Aluminium	Fine	363.430	38.369	0.670	0.169
	Finer	369.070	20.970	0.719	0.100

Table 3.18 contains the values for the shielding factor calculated for iron and for aluminium, regarding the maximum $\vec{J}$ values and the values obtained at the centre of the container.

As seen by the results, the iron slab has allowed for an attenuation by a factor of 50, but such conclusion can not be considered, since the δx of the shielding factors, regarding both the maximum values (40.4 %) as well as the centre values (28.1 %), is unacceptable.

Table 3.18: Shielding factor calculated for iron and aluminium regarding the maximum current density value in the container and the value observed at the centre of the cylindrical container.

Metal	Mesh	Shielding factor	
		Max	Centre
Iron	Fine	54.380	51.780
	Finer	91.290	71.985
Aluminium	Fine	542.433	227.036
	Finer	513.310	209.700

However, regarding the thicker slab of aluminium, the 500-fold reduction of the maximum $\vec{J}$ value can be considered as valid, with a δx of 5.7 %, as well as the attenuation by more than two orders of magnitude, observed at the centre of the cylindrical container (200-fold reduction). For the latter, the δx was calculated as 8.3 %, thus inferior to the 10 % acceptable simulation error. This result, obtained with the aluminium slab is in compliance with the experimental results shown in Figure 3.25, therefore validating the capability of the 2.5-cm thick aluminium slab to shield the B-field pulse.

3.5.2 Attenuation of the TMS-induced pulse measured by a probe coil

A similar study to the one performed with the cylindrical container filled with saline solution, was conducted to assess the attenuation of the transient B-field measured by two pickup coils as seen in Figure 3.27. Again, the built in-house stimulator was used to deliver the single, monophasic TMS-like pulses through the 7-turn coil.

A single-loop probe coil with a 6-cm radius was placed around the TMS coil in order to pick the magnetic flux generated by the increasing current passing through the 7-turn coil and to evaluate if the presence of a metal slab had any influence over the induced pulse. A smaller coil (7.5-mm radius) was then placed above the TMS coil as illustrated in Figure 3.27 with the purpose to evaluate the B-field attenuation capability of the aforementioned iron and aluminium slabs, which dimensions are illustrated in Figure 3.26.

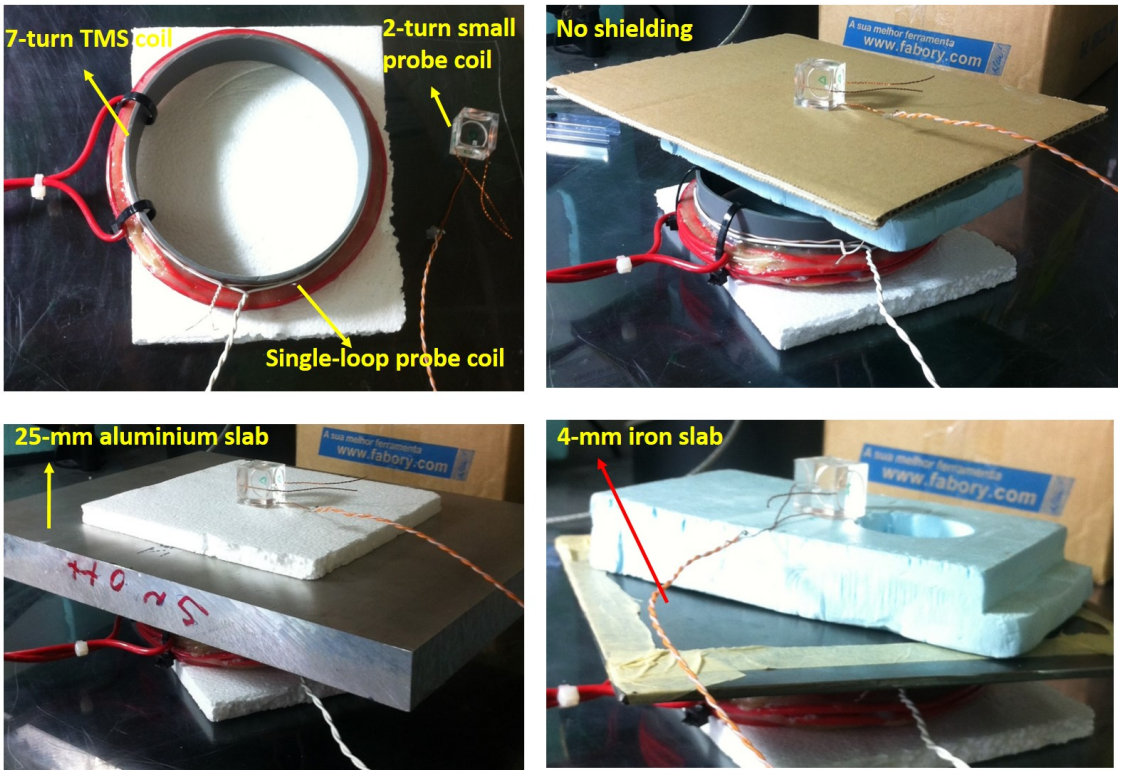

Figure 3.27: Setup used for the experimental measure of the TMS pulse induced in two probe coils. One single with a diameter of 12 cm and a 2-turn probe coil with a 1.5-cm diameter were placed around the 7-turn TMS coils and above that same coil, respectively. A 4-mm thick iron slab and a 25-mm thick aluminium slab were positioned between the TMS coils and the small pickup coil.

A piece of cardboard, an iron slab and an aluminium slab were positioned, one at a time, between the small 2-turn probe and the TMS coil. The cardboard does not interfere, in any way, with the varying B-field, and was used only to keep the distance between the smaller sensor and the TMS coil constant throughout the tests. In addition, styrofoam, which also does not perturb the B-field, was used for the same purpose. The pulses induced in this 2-turn coil therefore reflect the attenuation of the increasing B-field provided by the metal shielding barriers. Such results are shown in Figure 3.28a.

The readouts from the larger probe coil allowed to see the effects of having a metal slab near the TMS coil. As seen in Figure 3.27b, the magnetically induced pulse in the single-loop probe is, indeed, affected by the presence of the metal, namely regarding the width of the pulse.

As demonstrated by Figure 3.28a, the induced pulse in the smaller probe is significantly attenuated when shielded by a metal slab. As expected, the wider and

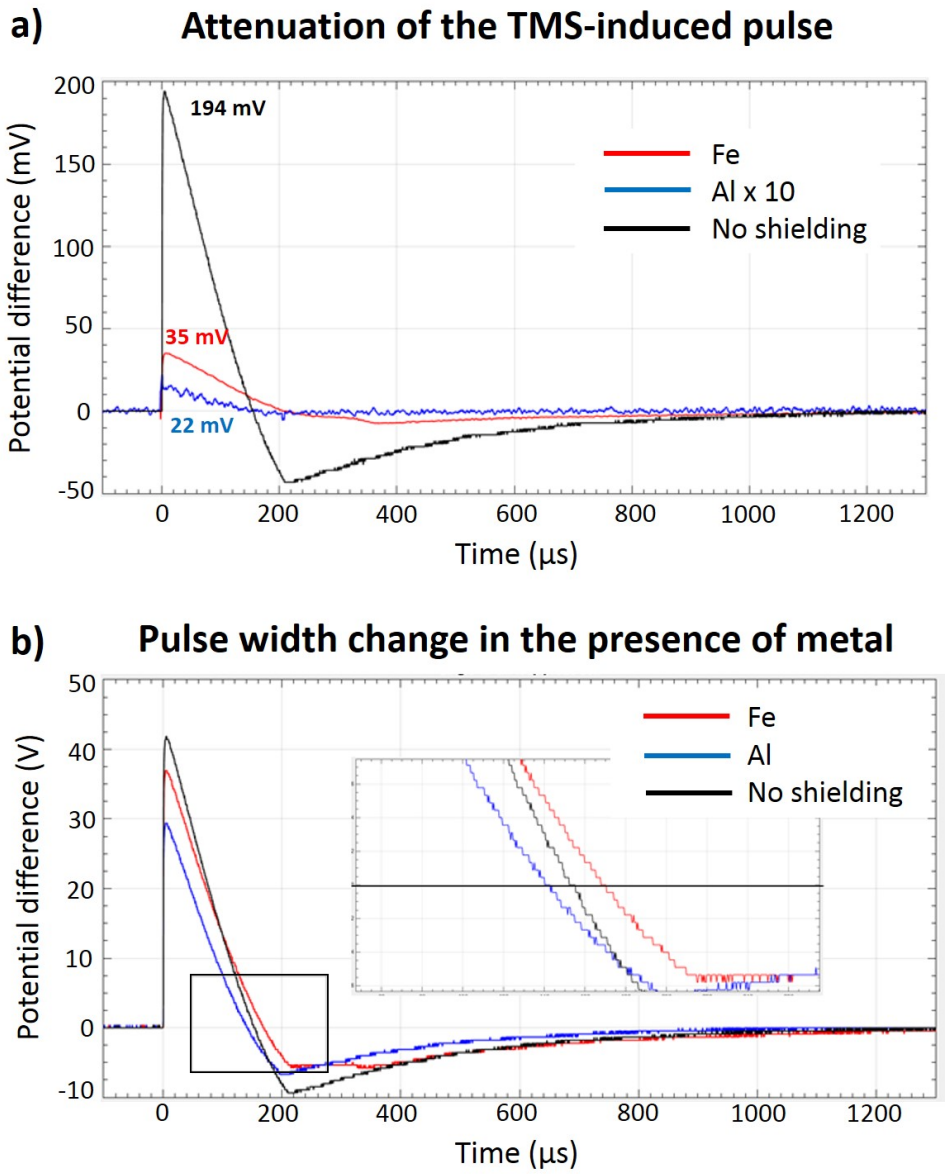

Figure 3.28: Experimental readouts from two probe coils. **(a)** Attenuation of the magnetically induced pulse in a 2-turn pickup coil positioned above the TMS coil, with a piece of cardboard (no shielding), an iron (Fe) or aluminium (Al) slab in between. The peak values are indicated for all three cases. Note that the vertical axis is in mV. **(b)** Variation of the timing of the pulse induced in a single-loop probe coil due to the presence of a metal slab, placed next to the TMS coil. The zero crossing points for all the three signals are enlarged for better visualisation.

thicker aluminium slab provided greater attenuation of the B-field, reducing the TMS-induced pulse by almost two orders of magnitude. The peak value dropped from 194 mV to approximately 2.2 mV, yielding a shielding factor of $S = 63.0$ (a scaling taking into consideration the pulse height ratio of Figure 3.28b was applied).

The iron slab, however, despite being only 4 mm thick allowed for a 5-fold reduction of the induced pulse, reflected by an S of 5.0 (the same aforementioned pulse scaling was applied).

Although it is not significant, when compared to the signal attenuation observed in Figure 3.28a, the pulse width change occurring in the signals sensed by the larger coil is still noticeable. As seen in the enlarged area of Figure 3.28b, containing the three zero crossing points, the proximity of an iron slab causes a slight increase on the timing of the pulse. On the other hand, the presence of aluminium is responsible for the decrease of the duration of pulse. When no shield is present, the wave crosses the zero point at 154 μs, whereas for iron this time increases to 167 μs and for aluminium drops to 140 μs.

Since the duration of the pulse, T, is proportional to the inductance of the coil (Roth and Zangen, 2012), these results can be explained by a variation of the total inductance, L.

Chapter 4

The effect of tissue conductivity

4.1 Introduction

As presented in the previous chapter, the proposed new five-coil dTMS system must contain a conducting liquid surrounding all the coils and part of the head model. Otherwise, it is not possible to induce such high current densities at the centre of the brain as the new dTMS system does.

The origin of the stimulation achieved by the proposed configurations within the Deep-Brain TMS project, including the new orthogonal configuration, had never been analysed, which motivated the simulation study described in this chapter. Due to the implementation of a conducting solution surrounding the patient head, it is crucial to understand if there is an electrical contribution, besides the magnetic stimulation, and if so, what is the relevance of the electrical stimulation concerning the neuromodulation capabilities of the new dTMS device.

As previously described in Chapter 2, standard and commercially available TMS devices stimulate the brain tissue through the E-field and associated eddy currents produced after placing an induction coil over the scalp.

With this in mind, a simulation study was performed, under the COMSOL Multiphysics® AC/DC software, considering an insulating layer surrounding the spherical brain phantom, specifically located between the skin layer and the cerebrospinal fluid, CSF. With this insulating layer it was possible to study the impact of all conductive layers existing in the head, including especially the skull.

The results and main conclusions of this study are presented in the following sections.

4.2 Deep transcranial magnetic stimulation: a simulation study

The simulation studies presented in this section were carried out under the COMSOL Multiphysics® AC/DC software, using the spherical head model described in Chapter 3.

First, a brief description of the surface charge effect is presented along with some studies that justify the need to include the conducting liquid in the proposed new orthogonal configuration, followed by the study that was performed in the scope of this work to understand the contribution of the electrical stimulation delivered by the 5-coil dTMS system.

4.2.1 Mitigating the surface charge effect

The inclusion of the conducting liquid, as a part of the dTMS system, emerged from the need to mitigate one of the main factors responsible for the rapid attenuation of the E-field with depth.

This physical limiting effect, termed surface charge effect, arises from the existence of surface discontinuities between the different head tissues, which have different electrical conductivities, σ (Miranda, 2013). Consequently, in the presence of the induced E-field, electric charge (ions) accumulates at these interfaces such as the skin/air or the CSF/skull interface, originating a secondary E-field that also contributes to the induced E-field. This secondary field can not be neglected and it is one of the reasons why realistic layers with correct values of conductivity must be incorporated in the head model (Miranda, 2013).

The surface charge density at the interfaces occurs because, although the E-field is the same on both sides of the interface, the conductivity is not. Therefore, the normal component of the current density is higher in the high-conductivity tissue leading to an accumulation of charge, since the amount of ions reaching the interface

is greater than the amount leaving it. Charge accumulation is proportional to the E-field intensity and is greater when the induced E-field is perpendicular to the tissue interfaces (Miranda, 2013).

Figure 4.1 depicts eddy currents alongside a surface discontinuity in which, such currents reach the interface in a non-tangential direction resulting in an accumulation of charge and consequent discharge along the surface boundary. When several eddy-current paths reach the same portion of a discontinuity, surface charge density grows, thus increasing the current density on the surface, hindering the penetration depth of the induced pulse by decreasing the current density on deeply located brain regions (Oliveira et al., 2012).

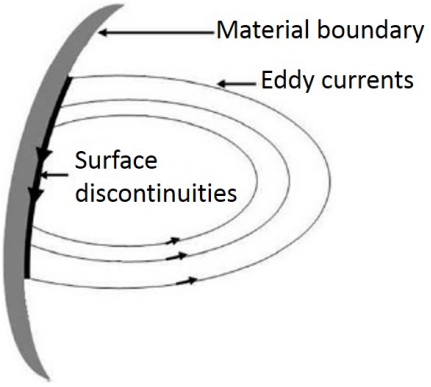

Figure 4.1: Schematic representation of the surface charge effect as a result of the presence of a discontinuity interfering with the path of eddy-currents. The boundary separates two media with different electrical conductivities The bold dark arrows represent the discharge along the surface discontinuity. Adapted from (Oliveira et al., 2012)

Within LIP collaboration it was shown, via simulation, that the surface effect, highly reducing brain penetration power in dTMS protocols, is, indeed, a direct consequence of surface discontinuities existing between the different layers considered in the realistic head model (Sousa et al., 2014).

However, this problem due to surface discontinuities can be mitigated by the use of a conducting liquid surrounding the head model and the system of coils. In the presence of this conducting solution the currents induced within the liquid will, in turn, induce eddy currents in the brain tissue in the opposite direction in respect to that induced without the liquid. Consequently, the induction of eddy currents

observed in the brain tissue is a result of both the transient current of the coil and the currents induced in the surrounding liquid (Simões et al., 2013).

Simões *et al.* demonstrated, experimentally, that the surface effect can be highly reduced by the implementation of a saline solution surrounding a cylindrical container filled with a brain-like solution. Both the coil and the brain-like solution (σ=0.11 S/m) were immersed in a larger container filled with a saline solution, 50 times more conductive than the brain-like solution. After the application of a TMS monophasic pulse, delivered by the magnetic stimulator described in Section 3.5, the induced E-field was measured in several points within the brain-like solution. The signal loss observed from the centre of the container relatively to the surface maximum was significantly reduced from 81 % to only 24 % when the stimulator coil and the brain-like solution were surrounded by air and conducting liquid, respectively (Simões et al., 2013). Therefore, it was proved that the signal intensity loss from the periphery to the centre can be highly diminished by immersing the system (coil + brain model) in conducting liquid.

By using the same four-layer head model (skin, skull, CSF and brain) described in the previous chapter, a simulation study was performed using a 5-cm radius circular coil located above the head model (Sousa et al., 2014). Simulation results are depicted in Figure 4.2, where three distinct cases were analysed. First, the head model was surrounded by air and with the three layers around the brain (skin, skull and CSF) having different conductivities (see Table 3.1). Then, the head model, as well as the coil, were immersed in conducting liquid (with an electrical conductivity of about 120 times higher than the conductivity of the brain), in which the three realistic external layers of the head model were also considered. Finally, the non-realistic situation, with the three external layers having the same σ, was also considered (Sousa et al., 2014).

The effect of encasing the spherical head model in conducting liquid is well illustrated by the shifting of the projection of the minimum current density from the centre of the brain (Figure 4.2-left) to the anterior region (Figure 4.2-middle). When all three concentric layers have equal σ, such minimum current density completely vanishes from the brain volume, proving that the surface effect is a consequence of

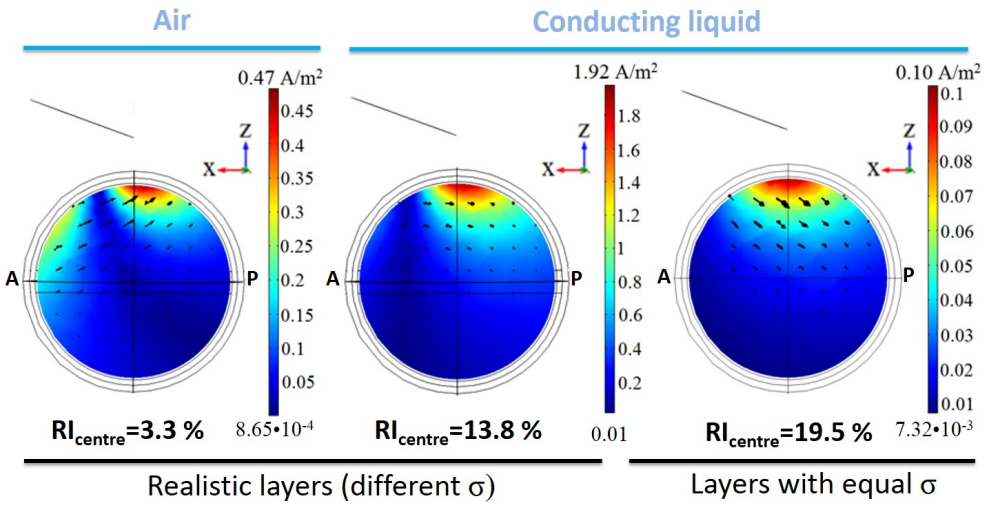

Figure 4.2: Distribution (colour scale) and direction (arrows) of the induced current density in a sagittal central slice of a spherical brain volume surrounded by three realistic layers (skin, skull and cerebrospinal fluid). The circular coil is anteriorly positioned above the head model and tilted by 20°. The relative induction (RI) at the centre of the brain in respect to surface maximum is shown for each case. **Left:** head model surrounded by air. **Middle:** head model surrounded by conducting liquid. **Right:** head model surrounded by conducting liquid, in which all the three external layers have identical electrical conductivities (σ). A: anterior. P: posterior. Adapted from (Sousa et al., 2014)

the surface discontinuities.

Additionally, the absence of the second surface maximum, observed in the left image, is also quite notorious and expected, reflecting the reduction of the accumulation of charge when the head model is surrounded by conducting liquid (middle and right images). When the conducting liquid is present the relative induction, RI, at the brain centre, is 4 times higher (RI=13.8 %) relatively to the situation when the system is surrounded by air (RI=3.3 %) (Sousa et al., 2014). Thus, the increase of the RI at the centre of the brain, due to the conducting liquid, also supports the conclusion that by attenuating the surface effect it is possible to maximise the current density induced in deeper brain structures.

4.2.2 The impact of skull tissue conductivity

To evaluate the hypothesis of the presence of skull tissue currents influencing the overall brain current distribution attained by the new orthogonal configuration, an insulating layer was simulated as a part of the spherical head model. Such layer was

placed between the skin and the CSF, thus substituting the skull, which already had the lowest conductivity among the three layers surrounding the brain (0.008 S/m). In order to ensure total absence of the electrical contribution, the chosen electrical conductivity for the aforementioned layer was $1 \cdot 10^{-15}$ S/m, thus preventing the currents induced in the conducting liquid from flowing across the head and reaching the brain.

Initially, the impact of the insulating layer on the distribution of the current density was analysed by means of a 5-cm radius circular coil placed above the head model. The same three situations mentioned in the previous Section 4.2.1, were again considered. Figure 4.3 shows the simulation results for the head model with different layer conductivities surrounded by air (left image) or immersed in conducting liquid, σ =10 S/m, (middle image) and lastly for the spherical brain surrounded by layers with identical conductivity of $1 \cdot 10^{-15}$ S/m, with the system also immersed in conducting liquid (right image).

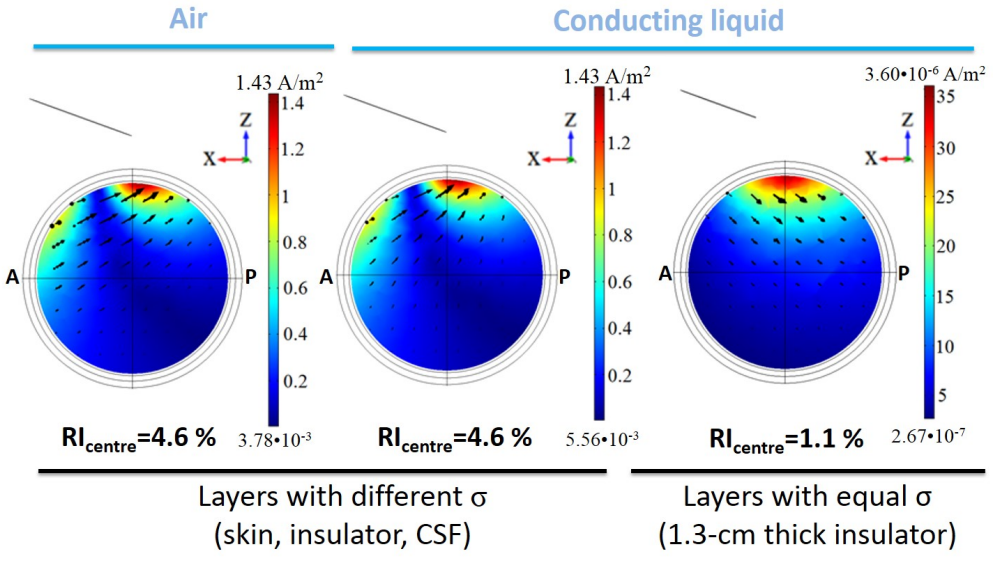

Figure 4.3: Distribution (colour scale) and direction (arrows) of the current density induced in a brain volume (sagittal view) surrounded by an insulating layer, located below the skin layer (left and middle). The circular coil was positioned above the spherical head model and tilted by 20°. The relative induction (RI) at the centre of the brain in respect to surface maximum is shown for each case. **Left:** head model surrounded by air. **Middle:** head model surrounded by conducting liquid. **Right:** head model surrounded by conducting liquid, in which all the three external layers have identical, and very low electrical conductivity (σ). A: anterior. P: posterior.

Unlike the results presented in Figure 4.2, the reduction of the surface effect, observed when considering a conductive solution around the spherical model, was highly hindered by the presence of an insulating layer. This is due to the charge accumulation that occurs at the surface discontinuities, mainly at the skin/insulator and insulator/CSF interfaces, which can not be avoided in spite of the presence of the conducting liquid. Additionally, the current density distribution and direction as well as the RI at the centre of the brain are quite similar between the two situations depicted in the left and middle images of Figure 4.3, which correspond to the full system surrounded by air and conducting liquid, respectively. Such findings support the conclusion that when the brain volume is electrically insulated, the implementation of a conducting liquid around the full system is useless regarding the attenuation of the undesirable surface charge effect.

Nevertheless, when all the concentric external layers have identical conductivities (*i.e.* when there are no discontinuities around the brain) this limiting effect is significantly reduced, as seen by the vanishing of both the minimum current density and the second surface maximum from the brain volume, in the right image.

When the full system is surrounded by air instead of a conducting solution, the effect of the insulating layer is not significant, probably because the relevance of the surface effect, observed even without the insulator, surpasses the influence caused by the insulating layer, as there are no relevant differences between the left images of Figures 4.2 and 4.3.

Contribution of skull conductivity for the new orthogonal configuration

A similar study was carried out using the orthogonal configuration described in Section 3.4.4. Such system was simulated while surrounded by air and conducting liquid (σ =10 S/m) and for the latter situation, the skull layer was substituted by an insulating material with an electrical conductivity of $1 \cdot 10^{-15}$ S/m. For the first case, the head model was considered with a realistic electrical conductivity for each one of the three layers (skin, skull and CSF) surrounding the brain volume.

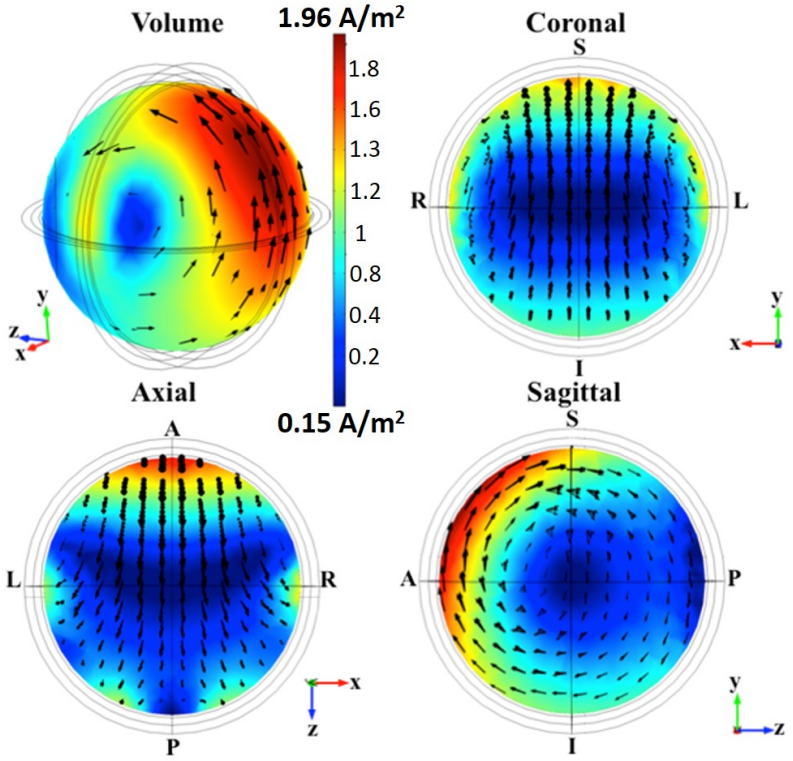

Figure 4.4: Three-dimensional view and central slices (coronal, axial and sagittal) of the human head model depicting the distribution (colour scale) and direction (arrows) of the induced current density in the spherical brain volume. Results obtained with the stimulating assembly surrounded by air and considering the skin, skull and cerebrospinal layers with realistic conductivities around the brain volume. A: anterior. P: posterior. L: left. R: right. S: superior. I: inferior.

Although the new orthogonal configuration has proved to be very efficient in stimulating the centre of the brain, with a RI of 60 %, such penetration power requires that the system of coils and part of the head model are immersed in a conducting solution.

If the surrounding medium is replaced by air (see Figure 4.4) the distribution of the induced current density drastically changes, since the surface discontinuities lead to an accumulation of charge at the interfaces, resulting in the previously described surface charge effect. By comparing these results with the ones obtained with the system immersed in conducting liquid (see Figure 3.22) it can be seen that the minimum current density shifted from the anterior-inferior region to the centre of the brain, as expected due to the surface effect. Additionally, the differences in the current density direction as well as in the magnitude of the current density range are quite notorious, resulting from the absence of skull currents, seen in Figure 4.4.

The influence of an insulating layer in the simulation results attained with the orthogonal configuration is well illustrated in Figure 4.5.

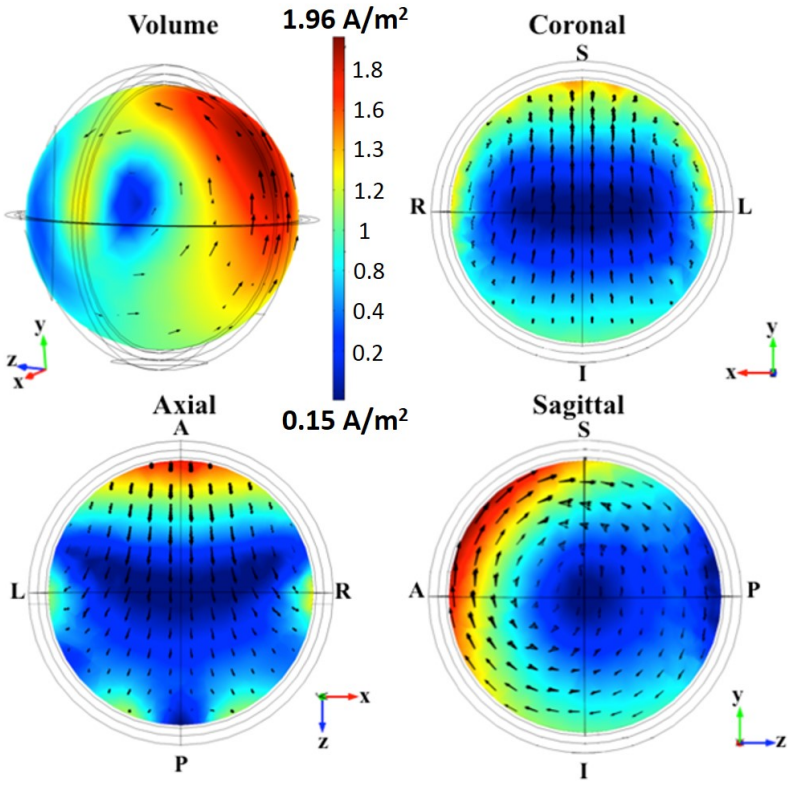

Figure 4.5: Three-dimensional view and central slices (coronal, axial and sagittal) of the human head model depicting the distribution (colour scale) and direction (arrows) of the induced current density in the spherical brain volume. Simulation performed with the system of coils and part of the head model immersed in conducting liquid. A highly insulating layer was considered between the skin and the cerebrospinal fluid. A: anterior. P: posterior. L: left. R: right. S: superior. I: inferior.

Despite being immersed in a conductive solution, Figure 4.5 illustrates the effect of the insulating layer. The differences between the results shown in Figure 3.22 and 4.5 clearly illustrate the high impact of the contribution of skull currents to the current distributions attained with the new 5-coil system in Figure 3.22.

Moreover, the similarity between Figure 4.4 and 4.5 is also remarkable, with the differences of the induced current densities only becoming noticeable at the mA/m^2 level (see Table 4.1). The insulating layer, despite the presence of the conducting liquid, is responsible for the shifting of the minimum current density to the centre of the brain, thus yielding a RI below 4 % at the brain centre. This enhancement

of the unavoidable surface effect is translated in a rapid decrease of the stimulation penetration power with depth.

Table 4.1: Current density values (A/m^2) in the brain tissue with the head model surrounded by air (Setup 1) or immersed in conducting liquid while brain is electrically insulated (Setup 2).

Simulation setup	**Brain volume (A/m^2)**			**Relative induction (%)**
	Max	**Min**	**Centre**	
Setup 1	1.962	0.152	0.072	3.6
Setup 2	1.964	0.151	0.072	3.6

From the presented study it is possible to conclude that the brain currents resulting from the orthogonal system are strongly complemented by electrical currents existing in the skull.

This work was of vital importance in order to explain, for the first time, the physical origin of the high penetration power of the new 5-coil dTMS device. It was demonstrated that a conductive layer is required to achieve such high deep-brain stimulation capability.

Chapter 5

New power electronics for high-frequency TMS: a simulation study

5.1 Introduction

Aiming for the countless benefits of rTMS protocols, a feasibility study was performed towards the development of a high-frequency magnetic stimulator capable of delivering TMS pulses at frequencies up to 10 Hz. The main challenge was to design and simulate a new power electronics system suitable for repetitive TMS, which first included the understanding of the underlying principles of a series RLC circuit.

In the present chapter, a brief introduction on series RLC circuits is presented as well as the two most widely used switches in TMS circuits.

Additionally, simulation results are also included, regarding the two configurations proposed and how the circuit parameters influence their energy efficiency as well as the charging time of the rTMS circuit, which is the limiting factor for the maximum frequency allowed for the repetitive magnetic stimulator.

5.2 TMS circuit as a series RLC circuit

As introduced in Chapter 2, TMS circuitry is based on a series RLC circuit (see Figure 2.10) defined by a second degree differential equation with constant coefficients as follows:

$$L\frac{\partial^2 I}{\partial t^2} + R\frac{\partial I}{\partial t} + \frac{I}{C} = 0 \tag{5.1}$$

Before the switch is connected, at $t = 0$, the current I is zero and all the energy is stored in the capacitor, with voltage V_C. Solving the Equation 5.1 gives the current I_L that flows through the circuit (Roth and Zangen, 2012):

$$I_L(t) = \frac{V_C}{\omega L} e^{-\alpha t} \sin(\omega t) \tag{5.2}$$

where $\alpha = R/2L$ is referred to as the damping factor since the $e^{-\alpha t}$ is responsible for the decay or damping of both V_C and I_L. The higher the value of α, the more rapidly I_L decays.

In the hypothetical, ideal situation where there is absolutely no damping and no energy dissipated in the resistor, since $R = 0$ and $\alpha = 0$, the circuit states would oscillate at the undamped natural frequency ω_0 (Agarwal and Lang, 2005), given by:

$$\omega_0 = \frac{1}{\sqrt{LC}} \tag{5.3}$$

Moreover, the duration T of one pulse cycle is determined by the inductance and capacitance as seen below:

$$T = 2\pi\sqrt{LC} \tag{5.4}$$

assuming the condition $R << \sqrt{L/C}$. Otherwise, the resistance R also influences the duration T (Roth and Zangen, 2012). For a typical TMS pulse, the initial E-field phase lasts for $t = T/4$, which usually is in the range of 50 to 100 μs (Peterchev et al., 2008).

Regarding the transient behaviour of the RLC circuit, some authors prefer to use another quantity to reflect such behaviour, defined as the exponential damping

ratio ζ which is a function of α and ω_0 (Irwin and Nelms, 2010):

$$\zeta = \frac{\alpha}{\omega_0} = \frac{R}{2}\sqrt{\frac{C}{L}} \tag{5.5}$$

The dynamic response of the RLC circuit due to an initial capacitor voltage depends on the value of ζ which reflects the oscillatory and/or decaying behaviour of the current flowing through the coil.

If $\zeta > 1$, the transient current exponentially decays without oscillations and this response is commonly called overdamped, where the energy exchange between the capacitor and the coil ceases (Agarwal and Lang, 2005).

When $\alpha = \omega_0$, the response is said to be critically damped, where the circuit response decays in the fastest possible time without oscillating. In this case, V_C and I_L exhibit similar behaviour.

Finally, when $\zeta < 1$ (underdamped dynamics), the response is an exponentially damped sinusoid which decays at a rate determined by ζ, with V_C and I_L exhibiting both oscillatory and decaying behaviour (Agarwal and Lang, 2005, Irwin and Nelms, 2010). The total circuit resistance R is the main responsible for the damping of the current and also influences the frequency $\omega = \sqrt{\omega_0^2 - \alpha^2}$ at which the underdamped response oscillates (Irwin and Nelms, 2010).

As seen in Equation 5.2, the current pulse generated in TMS is comprised of an exponential factor and a sinusoidal factor and therefore, TMS pulses are an example of an underdamped transient behaviour.

With this is mind, in the following simulation study, two different configurations were tested, varying the value of the total resistance R in order to investigate the role of the damping ratio ζ on the TMS pulse shape.

5.2.1 Power electronics switching devices: thyristor and insulated gate bipolar transistor

A crucial component of the TMS circuit is the fast switch, usually a thyristor or an insulated gate bipolar transistor, that must be capable of being traversed by very high currents in very short periods of time (Roth and Zangen, 2012).

Silicon Controlled Rectifier

The silicon controlled rectifier (SCR) or as it is more commonly known, thyristor, is a solid state[1] high-speed switching device capable of conducting heavy electrical loads. As seen in Figure 5.1, the SCR has three terminals labelled Anode, Cathode and Gate. This unidirectional semiconductor device has two distinct modes of operation, the on-state and the off-state in which the SCR behaves like a current source or an open circuit, respectively (Irwin and Nelms, 2010).

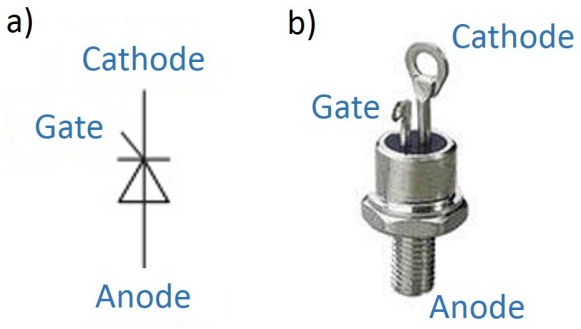

Figure 5.1: (a) Circuit symbol of a silicon controlled rectifier (SCR), a three-terminal semiconductor device labelled Anode, Cathode and Gate. Adapted from (Wintrich et al., 2011). **(b)** Photo of a typical SCR. Adapted from (Basic Electronics Tutorials, 2015*b*).

The SCR can be switched "ON" by the application of a brief current or input signal, of the order of 10 μs, across the gate terminal. This momentary gate signal is sufficient to trigger the SCR into conduction and once the thyristor has been turned "ON" it remains permanently in this fully-ON state, passing current only in the forward direction (*i.e.* from the anode to the cathode). In addition, since the thyristor is unidirectional it blocks the flow of reverse current, even if a gate signal is applied. While the SCR is conducting, the gate signal loses all control, since even if the gate signal is completely removed the switch remains in its on-state, acting like a rectifier diode[2], until the current flowing from the anode to the cathode decreases below the minimum holding current, I_H. Thus, in order to cause

[1]Solid state devices are electronic components based entirely on the semiconductor where the current is confined to solid elements, flowing as negatively charged electrons or positively charged electrons-free gaps, called holes.

[2]Rectifier diodes are components used to rectify alternating currents, which periodically reverse direction, converting them to direct currents that only flow in one direction.

the SCR to conduct in the first place the anode current must be grater than I_H (Basic Electronics Tutorials, 2015*b*, Wintrich et al., 2011).

Consequently, when the current is a sinusoid like the TMS pulse, the thyristor automatically turns itself "OFF" near to the cross over point at the end of every half-cycle, as the anode current is reduced below the holding current. This effect is known as natural commutation of the SCR and it is very important to the pulse generation in TMS circuits, as it is demonstrated in the following sections. The SCR then remains in the off-state until the next gate triggering signal is applied.

Another advantage of the SCR is that, once conducting, the current flow is only limited by the external resistance of the circuit because the internal forward resistance can be very low (Basic Electronics Tutorials, 2015*b*, Wintrich et al., 2011).

Insulated Gate Bipolar Transistor

The insulated gate bipolar transistor (IGBT) is also a semiconductor switching device capable of handling large collector-emitter currents. Like the SCR, the IGBT has three terminals termed Collector (C), Emitter (E) and the Gate (G) (see Figure 5.2). The first ones are related with the current conductance path, while the gate terminal controls the IGBT behaviour (Basic Electronics Tutorials, 2015*a*, Perret, 2009).

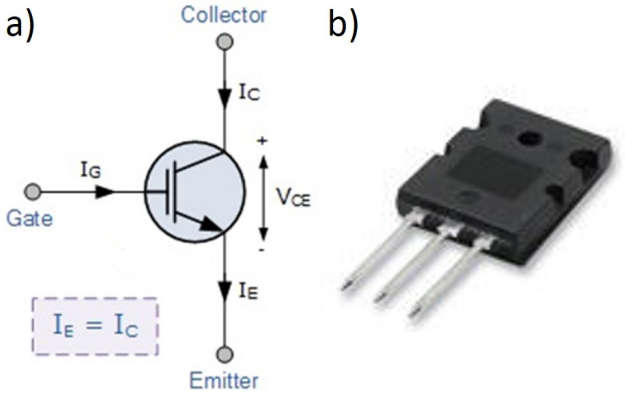

Figure 5.2: (a) Circuit symbol of an insulated gate bipolar transistor (IGBT), a three-terminal semiconductor device labelled Collector, Emitter and Gate. **(b)** Photo of a typical IGBT. Adapted from (Basic Electronics Tutorials, 2015*a*).

In IGBTs, the gate is isolated from the main current channel, so $I_E = I_C$, which makes the IGBT much easier to control. It can be switched "ON" or "OFF" by

simply activating or deactivating the gate terminal. By applying a positive voltage input signal across the gate and the emitter, the device is turned "ON" and remains in this on-state until the input signal is removed.

Similarly to SCRs, IGBTs also have low internal on-state resistance, meaning that the voltage drop, $V = IR$, across the component for a given current I is much lower as well as the power, $P = I^2R$, losses.

This voltage-controlled, unidirectional switch only needs a small voltage on the gate to keep conducting the current in the forward direction (from collector to emitter).

Consequently, IGBTs are widely used in power electronics applications due to their high-voltage capability, fast switching speeds, low conduction losses and a very flexible control (Basic Electronics Tutorials, 2015*a*, Perret, 2009).

5.3 Simulation study under PSPICE

All the simulations presented in this chapter were performed under the OrCAD®PSpice® simulation software (Cadence Design Systems Inc., 2015), described in more detail in Appendix I.

In this initial study, towards the development of a high-frequency magnetic stimulator capable of delivering TMS pulses at a frequency up to 10 Hz, two different configurations were simulated. The main difference between them had to do with the semiconductor switching device considered. The first configuration was designed including two IGBTs as switching devices whereas the second configuration used two SCRs instead. Henceforth, these two configurations will be referred to as Circuit A and Circuit B, respectively.

5.3.1 Two different rTMS circuit configurations using IGBTs or SCRs

Herein, the schematics of both alternatives are presented as well as the basic principle of operation of each one of the circuits.

The constant values of L and C, in both configurations, were set in compliance to the values of inductance and capacitance of the electronic components used in the real, available stimulator, described in Section 3.5.

Circuit A: IGBT-based rTMS circuit

Figure 5.3 depicts the schematics of Circuit A, comprised of two capacitors ($C1 = C2 = 1200\,\mu F$), one coil ($Lr1 = 10\,\mu H$), two diodes ($d1$ and $d2$), a total resistance R and two IGBTs ($Sw1$ and $Sw2$). The total resistance of the circuit is the sum of the internal resistance of the capacitor considered, $R2$ or $R3$, the resistance of the coil, $R4$, and the internal resistance of the IGBT, which was not considered in the total resistance values presented henceforth. Signal sources, $V4$ and $V5$, are the generators of the positive voltage input signal that is applied across the gate terminal of the IGBTS $Sw2$ and $Sw1$, respectively. The pulse width of such signals is predetermined since it corresponds to the period of time in which the IGBTs are switched "ON". At $t = 0$ the capacitor $C1$ is fully charged, having a potential of 600 V and $V_{C2} = 0$ V.

Since there is a need for the current to flow in both directions, forward and reverse, two diodes, $d1$ and $d2$, are connected in parallel with the IGBTs $Sw1$ and $Sw2$, respectively. Thus, the inclusion of $d1$ and $d2$ is of vital importance since the IGBTs are unidirectional devices that only conduct the current in one direction.

To better understand the circuit dynamics and how the pulses are generated, the following figures show the temporal progress of the coil current I_L and of the current passing through both capacitors as well as the rate of change of the voltage of each capacitor. Additionally, in Figure 5.5, the rate of change of I_L is depicted. The evolution of dI_L/dt reflects the behaviour of the voltage V_L at the terminals of the coil (Roth and Zangen, 2012), since:

$$V_L = L\frac{dI_L}{dt} \tag{5.6}$$

The time derivative of I_L corresponds to the TMS-induced pulse in the brain, since the temporal variation of the induced E-field is determined by the rate of change of the current in the coil, dI_L/dt (Miranda, 2013, Simões et al., 2013).

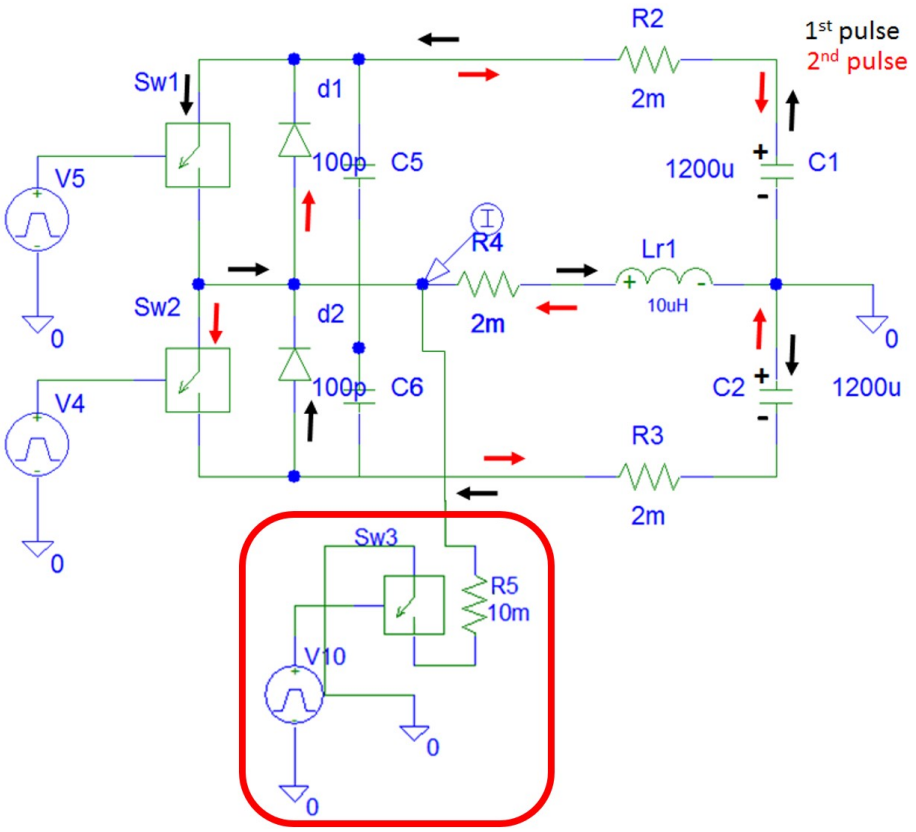

Figure 5.3: Schematics of repetitive pulse TMS-like circuit based on insulated gate bipolar transistors (IGBTs). The black arrows represent the current path in the first pulse and the red arrows are associated with the second pulse. The circuit inside the red box is a damping sub-circuit.

By analysing Figure 5.4, it is important to note that the first pulse is produced during $\Delta t_1 + \Delta t_2$ and the second pulse during $\Delta t_3 + \Delta t_4$. All Δt_i have approximately the same duration of about 170 μs each, which is in compliance with the literature (Roth and Zangen, 2012).

Following the black arrows in Figure 5.3 one can see that when $Sw1$ is activated, at the beginning of Δt_1, the capacitor $C1$ starts discharging through the coil, and therefore V_{C1} decreases accompanied by an increase of I_L and I_{R2} (see Figure 5.4). At the end of Δt_1, the $V5$ input signal is removed, deactivating the IGBT $Sw1$ which starts behaving like an open circuit.

In Δt_2, the diode $d2$ starts conducting ($I_{R2} = 0$ and there is current flowing through the resistor $R3$). Consequently, the capacitor $C2$ is being charged as seen by the variation of V_{C2}. V_{C2} is negative because the voltage probe was placed on the

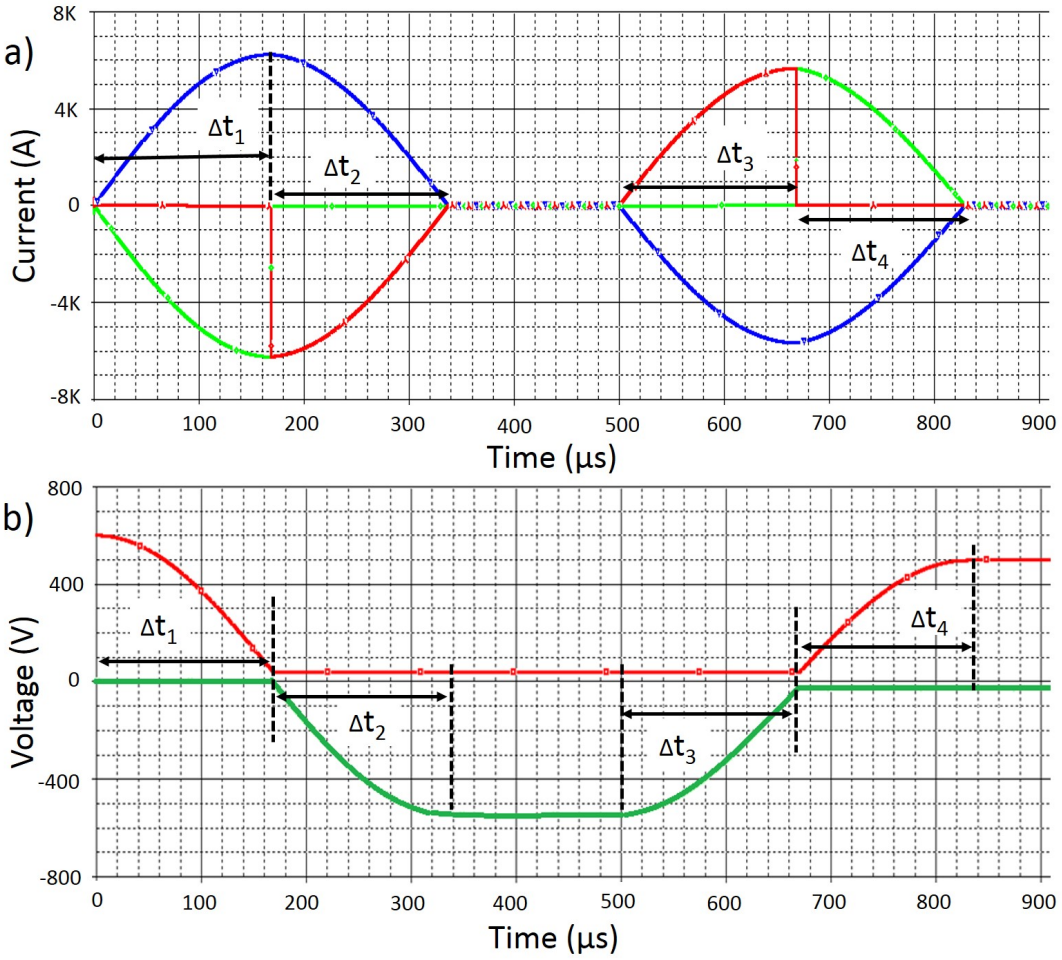

Figure 5.4: **(a)** Temporal evolution of the coil current, I_L (blue), of the current passing through the resistor $R2$, I_{R2} (green) and of the current flowing across the resistor $R3$, I_{R3} (red). **(b)** Voltage of the capacitor $C1$, V_{C1} (red) and voltage of capacitor $C2$, V_{C2} (green).

negative side of $C2$, right next to resistor $R3$. As stated in Section 2.4.2, this ability to recover a significant portion of the energy in the second capacitor is crucial for rTMS devices since it reduces the capacitor charging time between pulses. Due to the dissipation of energy in the total resistance of the circuit, the pulse decays and terminates at the end of Δt_2.

The second pulse (represented by the red arrows in Figure 5.3) is produced in a similar way to that of the first pulse. The $Sw2$ is activated during Δt_3 leading to the discharge of $C2$. At the end of Δt_3, the $Sw2$ is turned "OFF", I_{R3} drops to zero since the diode $d1$ starts conducting recharging $C1$.

Regarding the TMS-induced pulse, in Figure 5.5, it is visible that the induced

pulse is biphasic with an approximate duration of 340 μs and has an amplitude of 60 A/μs, very similar to the results found in the published literature (Roth and Zangen, 2012, Simões et al., 2013).

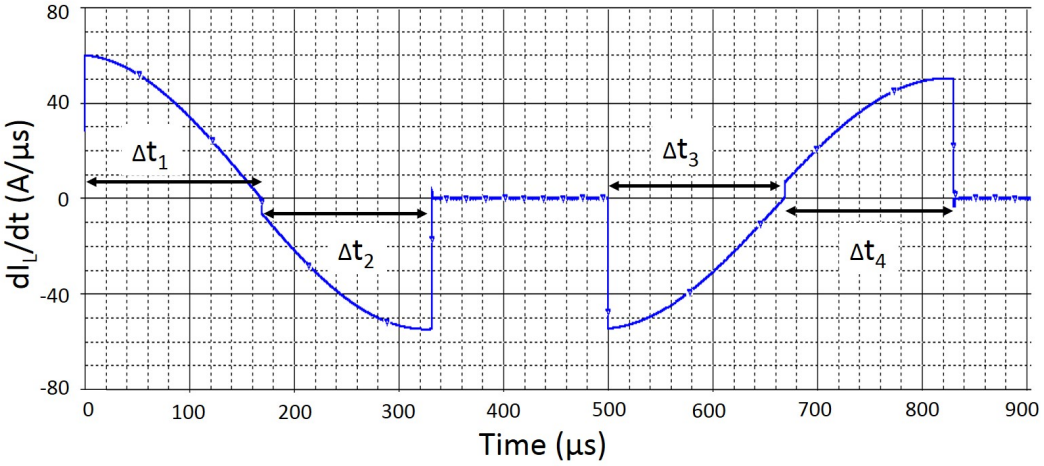

Figure 5.5: (a) Temporal evolution of the time derivative of the current passing through the coil, dI_L/dt.

By observing the corresponding time intervals Δt_i, it can be concluded that for the first pulse, the discharge of $C1$, while $Sw1$ is activated, is responsible for the positive phase of the TMS-induced pulse. Once $Sw1$ is turned "OFF", the voltage at the terminals of the coil inverts its polarity, although the current continues to flow through the coil in the same direction, as seen by the blue line in Figure 5.4a). As for the negative portion, in Δt_2, it is associated with the charging of $C2$.

Oscillation damping after the TMS-induced pulse

The damping sub-circuit represented in the red box in Figure 5.3 prevents the circuit of oscillating after each pulse. The residual energy that remains on the coil after the pulse is dissipated through the resistor $R5$ of 10 $m\Omega$, thus eliminating the oscillations after the pulse, that can reach up to 10 A/μs in amplitude. This sub-circuit is controlled by the IGBT $Sw3$ that is only activated at the end of the pulse and deactivated before the next pulse is generated. This effect is well illustrated in Figure 5.6 below.

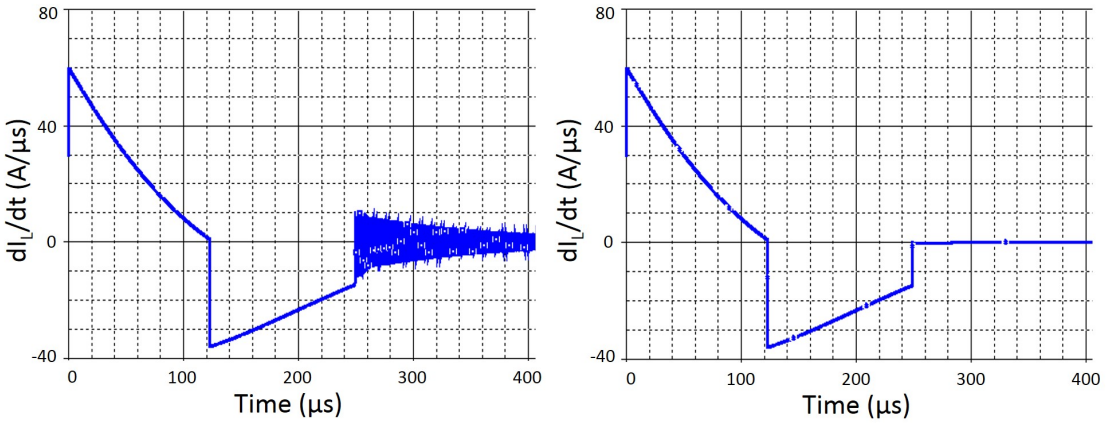

Figure 5.6: TMS-induced pulse with (left) and without (right) oscillations after the pulse is applied. The two pulses were generated by the same circuit A, with a total resistance of 110 $m\Omega$, apart from the absence (left)/presence (right) of the damping sub-circuit.

Circuit B: SCR-based rTMS circuit

A similar analysis was done for Circuit B which, instead of IGBT, uses SRCs as switching devices.

This alternative configuration includes two SCRs, $scr2$ and $scr3$, and the respective input signal sources, $V14$ and $V15$, one coil ($L5 = 10\,\mu H$) and one capacitor bank comprised of two capacitors ($C1 = C2 = 2400\,\mu F$) arranged in anti-series (back to back) so that the result is non-polarised with an equivalent capacitance of 1200 μF. Again, the total resistance is the sum of the resistance of the coil, RL, the internal resistance of the capacitor bank, $R1$, and the internal resistance of each SCR, which was not considered for the total resistance values presented henceforth. At $t = 0$ the capacitor $C1$ is fully charged, having a potential of 600 V and $V_{C2} = 0$ V.

After the application of a brief (10 μs) input signal in the gate terminal of $scr2$, the SCR starts conducting and $C1$ discharges through the coil $L5$. As demonstrated by the black arrows in Figure 5.7, the current is circulating towards $C2$, which is being charged. All of this occurs during Δt_5 (see Figure 5.8), period in which the SCR $scr2$ is always in its on-state, unlike the IGBT in Circuit A, which is turned "OFF" when I_L reaches its maximum, *i.e.* $dI_L/dt = 0$.

The snubber circuit ($R15$ in series with $C14$) is essential to the proper working of the whole electronics system. This is because when the SCR shuts off, there is

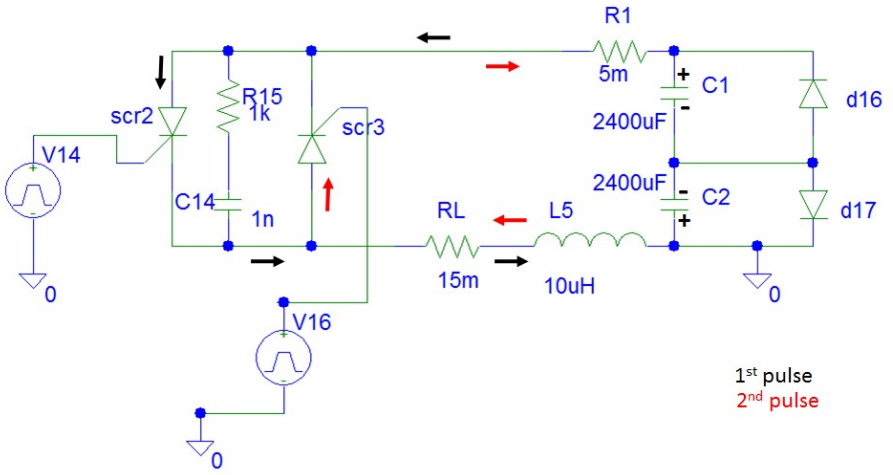

Figure 5.7: Schematics of repetitive pulse TMS-like circuit based on silicon controlled rectifiers (SCRs). The black arrows represent the current path in the first pulse and the red arrows are associated with the second pulse.

still some maintenance current in the coil $L5$.

Similarly to what occurs in Circuit A, the TMS-induced pulse is also biphasic and has a similar duration of the pulse produced in Circuit A, as $\Delta t_5 \approx 340\mu s$.

For the generation of the second pulse (red arrows in Figure 5.7), the process is quite identical but it is the capacitor $C2$ that is discharging through the coil, after the activation of the $scr3$.

In both cases, I_L flows always in the same direction for each pulse and it is V_L that changes its polarity, just like it happened in Circuit A. Finally, the pulses are terminated when I_L decreases below the minimum holding current, I_H, of the SCRs.

For both Circuit A and Circuit B, the capacitor bank is not being recharged between the first and second pulses, since there is no power supply connected to the circuit. This is the reason why the second pulse always appears with lower amplitude because there is less energy available for the second pulse. Nevertheless, this topic will be addressed further on.

Choosing one configuration over the other should take into account the pros and cons of the IGBTs and the SCRs. First of all, the Circuit A is more expensive since the IGBTs have a higher cost comparing with the SCRs (about 100 times higher). In addition, the price of the IGBTs increases significantly with the demands of the circuit, such as high voltages and high currents.

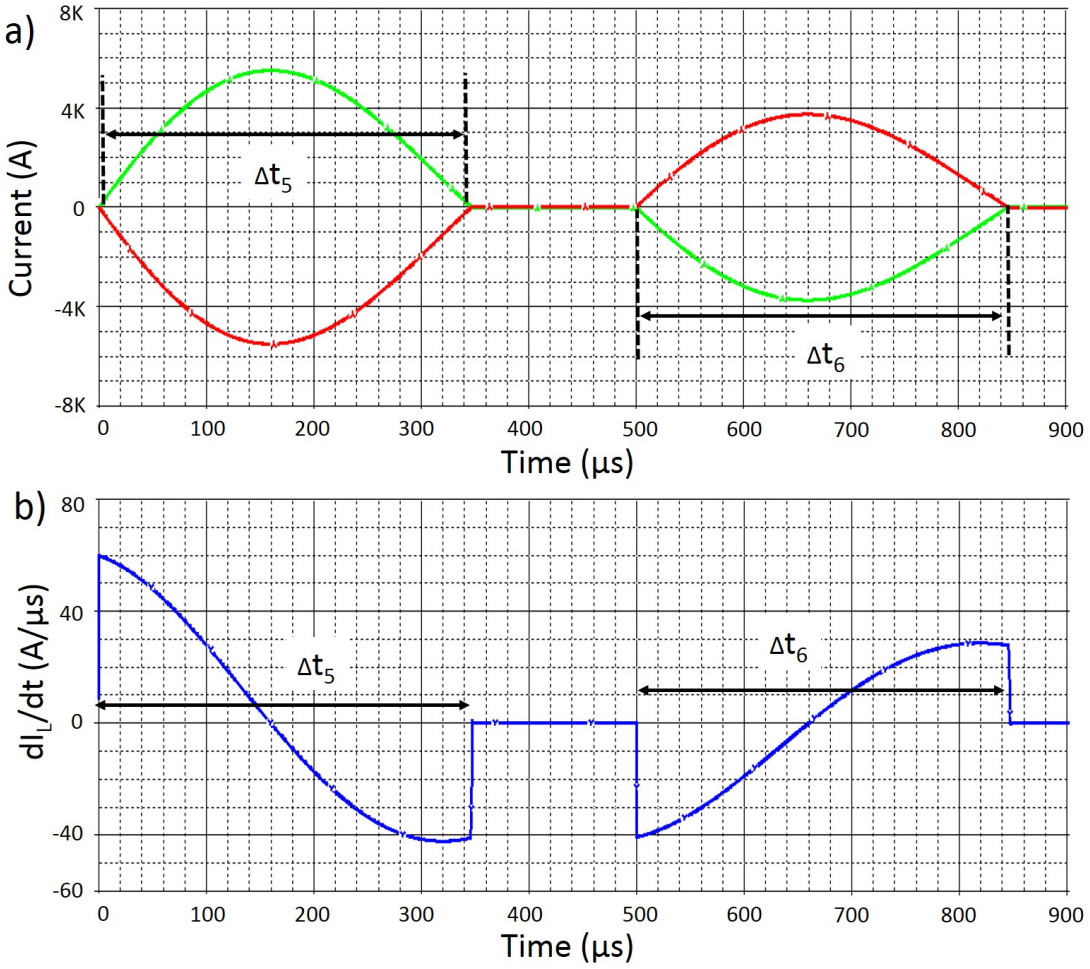

Figure 5.8: **(a)** Temporal evolution of the coil current, I_L (green), and of the current passing through the resistor $R1$, I_{R1} (red). **(b)** Time derivative of I_L as a function of time.

However, IGBTs are much more flexible, in a way that they can be programmed, for example via a microprocessor, allowing the control over the pulse shape and width. Since the duration of the on-state of the IGBT can be controlled, it is possible to modify the circuit to generate different types of pulses, upon need, without replacing electronic components.

SCRs, unlike the IGBTs, can not be programmed. The duration of their on-state depends only on the temporal evolution of the circuit response because the current must drop below a certain threshold in order to turn "OFF" the SCRs. Consequently, such switches offer a more permanent configuration, since in order to attain different pulses, the circuit must be redesigned, which necessarily implies new components that allow for the desired behaviour of the RLC circuit.

5.3.2 The effect of the damping ratio on the pulse shape and energy efficiency of the rTMS circuit

The situation depicted in Figure 5.3, is almost an ideal case since both the internal resistance of the capacitors and the resistance of the coil are very low (2 $m\Omega$ each). Because such electronic components are much harder to find and have much higher cost, a study was performed regarding the effect of the damping ratio ζ (mainly determined by the total resistance) on the TMS pulse. In fact, when considering more realistic values for the total resistance, the behaviour of the RLC circuit completely changes.

Apart from the pulse shape, the energy efficiency was also analysed in the following study, which was defined as the percentage of the total energy of the system that is recovered in the capacitor bank, at the end of the pulse, and not wasted as useless heat. Considering V_i as the initial voltage of capacitor $C1$ and V_f as the voltage of capacitor $C2$ after the pulse is generated, the energy efficiency is given by:

$$\eta = \frac{(1/2)CV_f^2}{(1/2)CV_i^2} \times 100 \ \% \tag{5.7}$$

The inductance of the coil and the capacitance were kept constant to 10 μH and 1200 μF, respectively. Moreover, the capacitor $C1$ was considered to be fully charged at a potential of 600 V before the pulse, so for each situation studied, $V_i = 600$ V. The 1 $m\Omega$ internal resistance of the SCRs and IGBTs was not considered for the calculation of the total resistance R.

Just for having a standard value, the energy efficiency and the damping ratio were calculated for the ideal situation of Figure 5.3 in which $R = 2\,m\Omega + 2\,m\Omega = 4\,m\Omega$. As a result and according to Equation 5.5, the damping ratio is $\zeta \simeq 0.02$. As seen in Figure 5.4, from the initial 600 V, 547.3 V are recovered in the capacitor $C2$ which yields an energy efficiency of about 83.20 % according to Equation 5.7.

This study was carried out using Circuit B but a simulation of Circuit A with higher R is also presented for comparison. Table 5.5 includes the results obtained for each configuration and the respective damping ratio of the circuit.

From the simulation results, for the same damping ratio of $\zeta = 0.6$, Circuit B

Table 5.1: Results of the simulations performed for different damping ratios. The initial voltage of capacitor $C1$ was set to 600 V. I_{max}: Maximum peak current in the coil. ζ: Damping ratio. η: Energy efficiency. R: total circuit resistance. V_f: Remaining voltage of capacitor $C2$ after the pulse.

Circuit	$\mathbf{R(m\Omega)}$	$\mathbf{V_f(V)}$	$\mathbf{I_{max}(A)}$	$\boldsymbol{\zeta}$	$\boldsymbol{\eta(\%)}$
A	4	544.8	6238	0.02	82.45
A	110	145.8	3240	0.60	5.90
B	20	504.0	5502	0.11	70.56
B	35	455.8	4943	0.19	57.71
B	55	406.1	4346	0.30	45.82
B	75	369.0	3869	0.41	37.81
B	110	325.6	3235	0.60	29.45
B	130	310.7	2954	0.71	26.81

appears to be about five times more effective than the configuration using IGBTs, regarding the energy recovered after the pulse. Nevertheless, a 30 % energy efficiency is still not sufficient for the desired behaviour of the high-frequency magnetic stimulator.

In the next figures, the effect of ζ on the pulse shape is clearly illustrated. For this study, only the first pulse is analysed, because the behaviour of the following pulses is quite similar. As expected, for higher values of ζ the exponential decay of the current becomes more significant as the oscillations get more attenuated.

As seen in Figure 5.8, in order to get a biphasic TMS-induced pulse the current passing through the coil must be an "half-sine" signal, which means that I_L must oscillate and therefore ζ must be minimal, so that the damping effect is not significant.

When considering $\zeta \leq 0.2$, it is possible to attain a biphasic TMS-induced pulse, either with Circuit A or Circuit B, similar to the ones produced by commercial stimulators like the Magstim® MagPro X100 (Sommer et al., 2006), as depicted in Figure 5.9.

Higher damping ratios, however, not only significantly reduce the energy efficiency as demonstrated in Table 5.1, but also tend to distort the shape of the signals I_L and dI_L/dt (see Figure 5.10). The TMS-induced pulse, as the value of ζ increases, tends to have a shape more similar to a monophasic pulse rather than

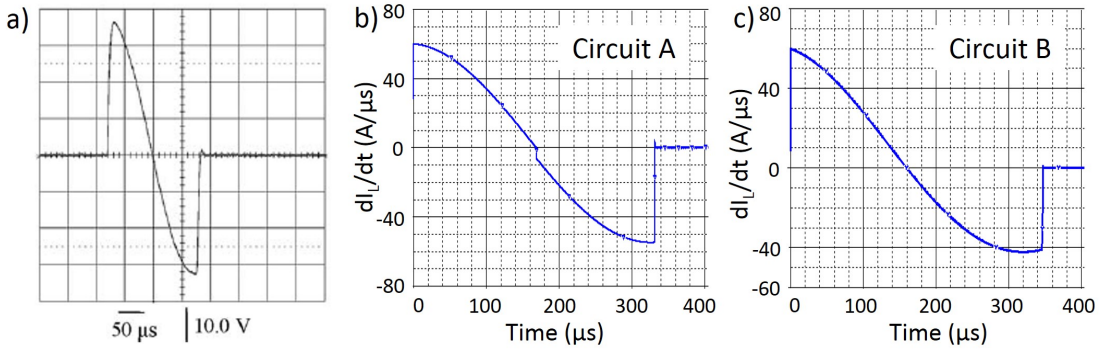

Figure 5.9: Comparison of TMS-induced biphasic pulses. **(a)** Biphasic TMS-induced pulse in a 0.5 cm radius probe coil by the MagPro X100 stimulator at 10 % of maximum stimulator output. Adapted from (Sommer et al., 2006). Biphasic TMS-induced pulse generated in Circuit A **(b)** and Circuit B **(c)**, with a damping ratio of 0.02 and 0.1, respectively.

the desired biphasic pulse.

This happens because when R is higher, for example $R = 110\,m\Omega$, the exponential factor in Equation 5.2 is much more relevant and the coil current is strongly attenuated. Subsequently, the maximum peak current is also significantly reduced from 5.5 kA to about 3 kA as seen in Table 5.1. Such effect occurs in Circuit B and it is even more distinguishable in Circuit A, as seen in Figure 5.10e.

To summarise, in a TMS circuit the resistance has to be minimal, normally on the order of 50 $m\Omega$ (Roth and Zangen, 2012). Additionally, a biphasic pulse is preferable, for the same reasons explained in Section 2.4.2 regarding the triphasic pulse. Therefore, this study aimed to find the threshold damping ratio that allows an acceptable pulse shape (*i.e.* a biphasic TMS-induced pulse) by investigating the effect of the total resistance on both the pulse shape and the energy efficiency of the system. It was concluded that the damping ratio must be of the order of 0.2, thus enabling a recovery of almost 60 % of the initial energy, which sets an upper limit of 35 $m\Omega$ for the total resistance of the circuit.

5.3.3 Recharging the rTMS circuit

One particularly important property of a rTMS circuit is the time that the capacitor bank takes to fully recharge, after each pulse. Even when considering the aforementioned almost ideal situation, the energy efficiency is of the order of

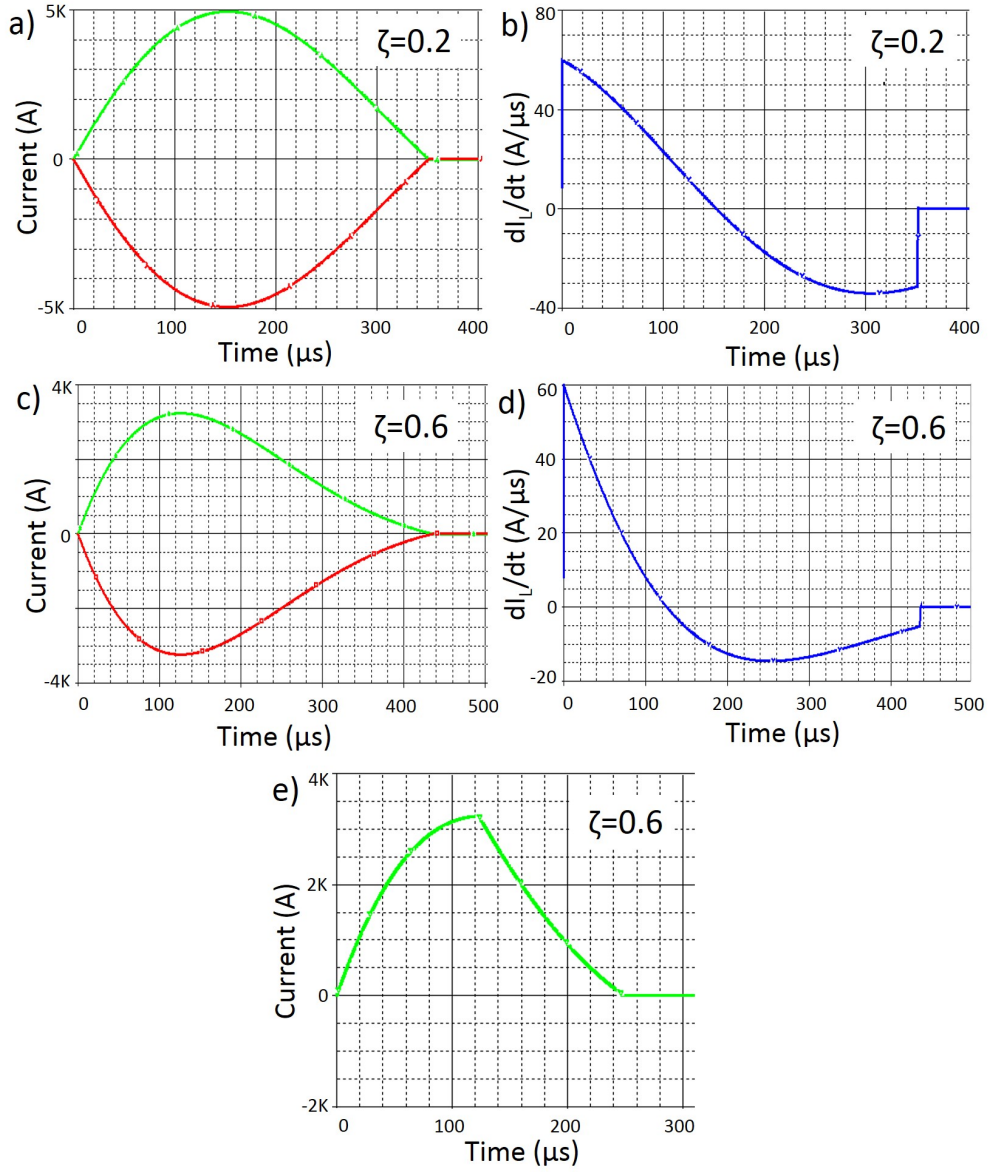

Figure 5.10: Effect of the damping ratio on the response of Circuit B **(a)-(d)** and Circuit A **(e)**. Temporal evolution of the coil current, I_L (green), and of the current passing through the resistor $R1$, I_{R1} (red) for a damping ratio $\zeta = 0.2$ **(a)** and $\zeta = 0.6$ **(c)**. Time derivative of I_L as a function of time for $\zeta = 0.2$ **(b)** and $\zeta = 0.6$ **(d)**. **(e)** Coil current for $\zeta = 0.6$.

80 % which reflects the need for a power supply that enables the recharge of the capacitor bank. Otherwise, the energy available for the next pulse will always be inferior than the energy of the previous pulse, resulting in a decrease of the pulse amplitude.

To illustrate this amplitude loss, Circuit A was simulated but only considering the capacitor $C1$, after short-circuiting the capacitor $C2$ and adjusting the values of

the resistors $R2$, $R3$ and $R4$ to 90 $m\Omega$, 2 $m\Omega$ and 20 $m\Omega$, respectively. The resulting TMS-induced pulse was monophasic, as shown in Figure 5.11, which compares the situation with and without recharging of capacitor $C1$.

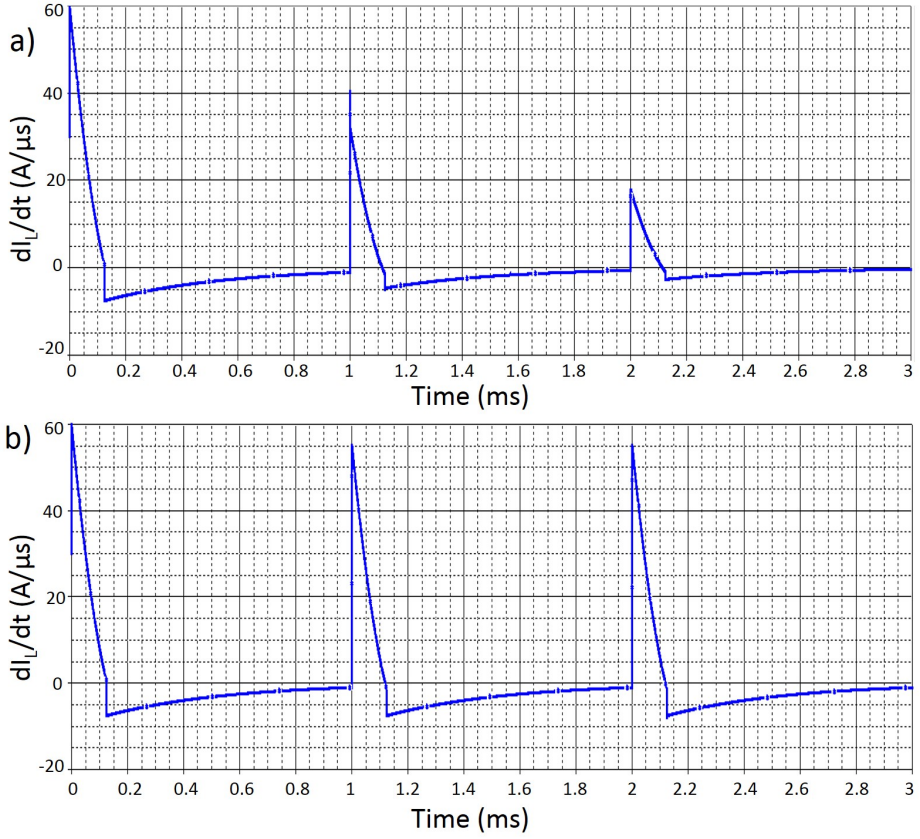

Figure 5.11: Effect of capacitor recharging on the TMS-induced pulses. **(a)**Three monophasic TMS-induced pulses with the capacitor not being recharged after each pulse **(b)** TMS-induced pulses with the capacitor $C1$ being fully recharged at the initial voltage of 600 V, after each pulse.

The reduction of the amplitude of the second and third pulses is notorious when $C1$ is not recharged, decreasing from 60 A/μs of the first pulse, to about 35 A/μs and 20 A/μs for the second and third pulses, respectively. However, when $C1$ is set to 600 V after each pulse, no significant amplitude decrease was observed (see Figure 5.11).

Therefore, in order to guarantee that the energy available is kept constant for every pulse, a charging sub-circuit was proposed, which is capable of feeding the capacitors of Circuit A and Circuit B. This power supply (see Figure 5.12) is comprised of a 230 V (root mean square value voltage) AC power source, an AC-DC converter and the IGBT $Sw3$ which is activated at the end of each pulse

and is turned "OFF" before the next pulse is applied, when the capacitors are fully charged with the required voltage.

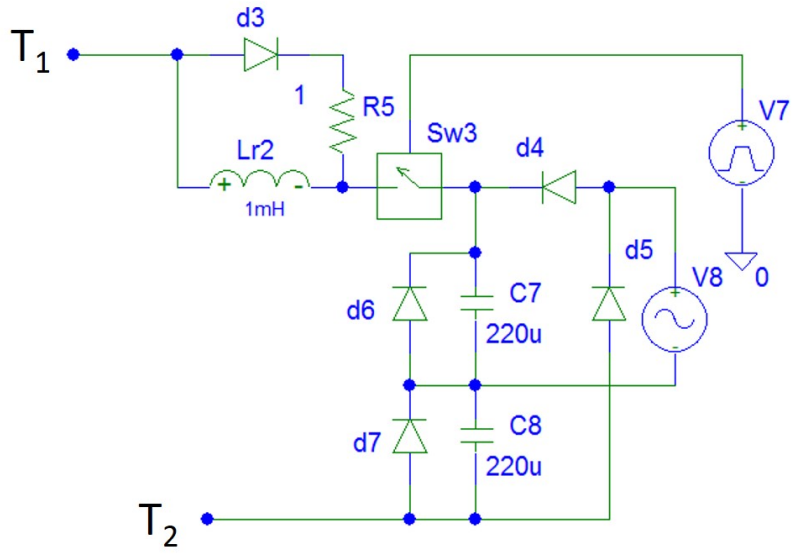

Figure 5.12: Power supply of a rTMS circuit. From the AC power source, $V8$, a potential difference of 650 V is generated between terminals T_1 and T_2 that will feed the capacitor bank, thus recharging the circuit after each pulse is delivered. Circuit A and Circuit B connect to this power supply via terminals T_1 and T_2.

During the positive phase of the AC signal, originated by $V8$ in Figure 5.12, the capacitor $C7$ is charged up to 325 V, whereas during the negative phase, the capacitor $C8$ charges to -325 V. As a result, the AC-DC converter essentially duplicates the 325 V (peak value voltage) to generate a potential difference of 650 V that is posteriorly transferred to the capacitor bank through the coil $Lr2$, after the IGBT is activated.

Immediately after the switch $Sw3$ is turned "ON", the capacitor bank of the main circuit starts to be charged and experiences an abrupt variation of its voltage V_C. Assuming that

$$I_C = C\frac{dV_C}{dt} \tag{5.8}$$

it is expected that once the IGBT starts conducting, a high-amplitude peak current is observed. In order to attenuate this peak current, the inductor $Lr2$ was projected. According to Equation 5.6, the coil will oppose to the sudden change of the current, limiting the value of dI/dt, thus smoothing the peak current. Such effect was

indeed demonstrated by reducing the inductance of the coil $Lr2$ to 10 nH, which is equivalent to replacing the coil by a simple wire. Then, a simulation of the Circuit A, with a total resistance of 35 $m\Omega$, connected to the charging sub-circuit was performed. When the 1 mH coil was considered, the peak amplitude was only of about 325 A, whereas when the inductance was reduced to 10 nH, the maximum peak reached approximately 26 kA, which highlights the role of the coil $Lr2$ in preventing such high-amplitude peak currents.

For both circuits, A and B, the charging process must be alternated between the two capacitors, $C1$ and $C2$, in order to guarantee that the energy available for each pulse is the same. For example, before the first pulse, the capacitor $C1$ of both circuits must be charged to a certain required voltage, whereas for the second pulse the same must occur, but to the capacitor $C2$. This procedure should be repeated over and over again throughout the whole rTMS protocol, assuring that all the pulses delivered have the same intensity.

Consequently, two configurations were proposed to allow the alternated charging of the capacitors $C1$ and $C2$, using the same sub-circuit, shown in Figure 5.12, for Circuit A and Circuit B. These schematics are presented in Figure 5.13 where the connections between the terminals T1 and T2 of the charging sub-circuit and the main circuits, A and B, were projected using IGBTs.

As demonstrated in Figure 5.13, for Circuit A, the capacitor $C1$ is charged after the simultaneous activation of S_{A1} and S_{A2} and capacitor $C2$ is charged when S_{A3} and S_{A4} are conducting. Likewise, for Circuit B, $C1$ is charged when S_{B1} and S_{B2} are turned "ON" and after the activation of S_{B3} and S_{B4}, the potential difference of 650 V, between the terminals $T1$ and $T2$, is transferred to $C2$ instead.

Both schematics include four IGBTs, required to establish the connection between the main circuit and the power supply. Therefore, the electronic components needed to charge Circuit A and Circuit B are essentially the same and there are no significant differences in choosing one configuration over the other, regarding the circuitry that feeds the system.

Another key point is the design of the charging sub-circuit according to the repetition rate pretended for the rTMS system. An initial simulation was carried

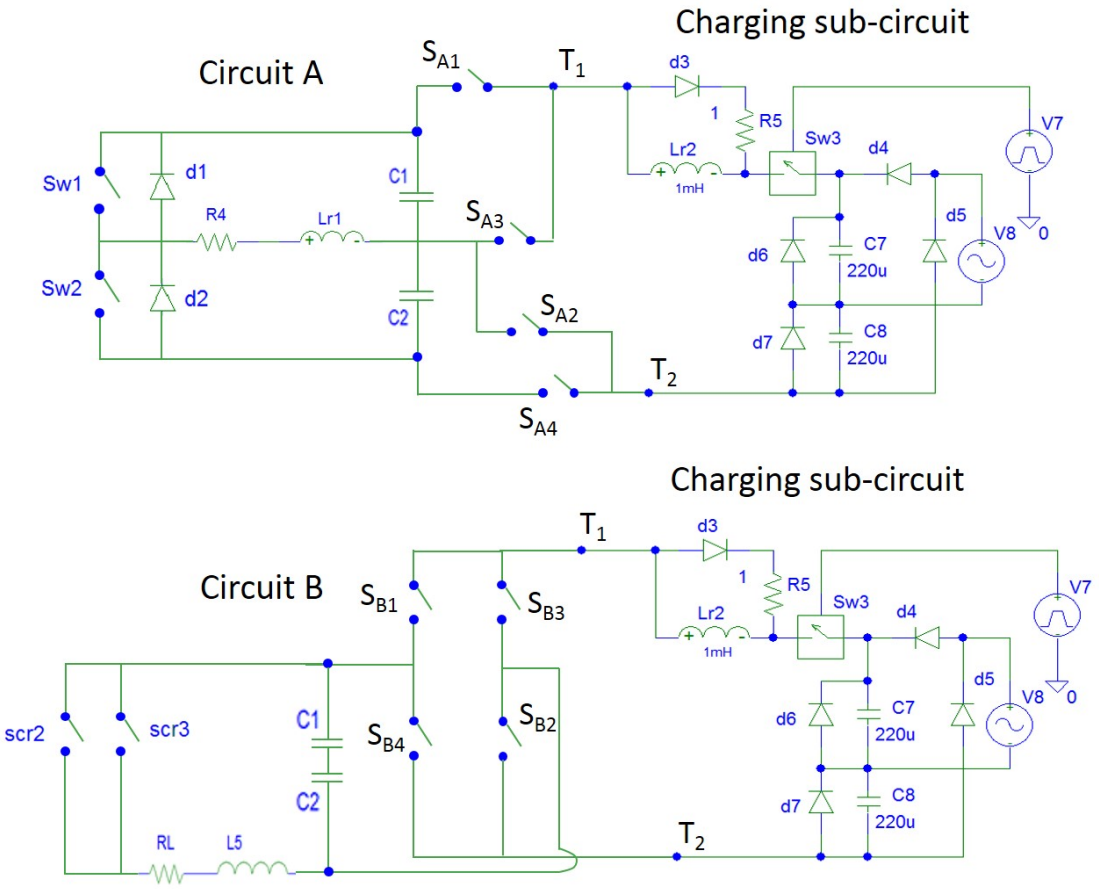

Figure 5.13: Charging sub-circuit connected to Circuit A (top) and Circuit B (bottom). The switches S_{Ai} and S_{Bi} are insulated gate bipolar transistors (IGBTs). By controlling the duration of the on-state of each IGBT it is possible to alternately charge $C1$ and $C2$ for both Circuit A and Circuit B.

out with the charging sub-circuit connected to Circuit A ($R = 35\,m\Omega$) in order to assess the time required for the capacitor $C1$ to charge up to 600 V. Results showed that the proposed system took about 100 ms to charge $C1$, which is in compliance with the desired frequency of 10 Hz for the high-frequency rTMS device. Capacitors $C7$ and $C8$ must be carefully selected due to their influence on the recharging time which, in turn, sets the limit for the maximum frequency allowed for the magnetic stimulator.

Chapter 6

Conclusions and future directions

The aforementioned orthogonal configuration constitutes an ongoing project started some years ago with the main purpose to design, by simulation, a new TMS system capable of inducing currents in the centre of the brain with an induction capability higher than that of state of the art TMS devices. Such standard TMS coils remain, so far, unable to handle several neurological disorders requiring deep-brain stimulation, therefore constraining the full potential of this non-invasive technique.

In order to overcome this gap, a five-coil system, termed orthogonal configuration, had already been proposed in previous collaborative work, being capable of stimulating the brain centre with an intensity above 50 % in respect to the surface maximum. However, initial COMSOL Multiphysics® AC/DC-based simulations, performed within the scope of this dissertation, showed that such coil design was not guaranteeing the safety of the patient, therefore compromising the whole project.

Consequently, the former orthogonal configuration was redesigned and updated, aiming to guarantee the safety of the patient and the safety of any system operator or nursing staff while keeping the penetration power in depth, allowing for the neuroactivation of deeply located brain regions.

By modifying the shape of the coils and the currents flowing through each one of them, the new improved TMS system attained an unprecedented 60 % relative induction in respect to the surface maximum.

As for the safety issues, mainly related to the potential induction of heart fibrillation by the 5-coil configuration, the shielding capability of a metal structure was investigated. Simulation results, supported by experimental data, have shown that a shielding barrier of iron or aluminium is, indeed, capable of attenuating the transient B-field, reflected by a reduction of two orders of magnitude of the current density induced in a saline solution. Starting from a metal slab, the shielding structure was optimised until the proposal of a metal cage, surrounding the five coils, the conducting liquid container and the patient head. This shield allowed, for the first time, to reach negligible current density values in the heart of the patient (3 mA/m^2) and the operator (0.7 mA/m^2). Such results, which are about three orders of magnitude below the heart fibrillation threshold, are quite encouraging towards the development of the orthogonal configuration shielded by a relatively simple and economic solution, compatible with the future implementation of this system in health facilities.

Furthermore, and following the fact that the physical origin of the stimulation achieved by the 5-coil system had never been analysed, a simulation study was carried out proving that electrical conduction is occurring in the skull in the orthogonal configuration. By using an insulating layer in place of the skull, thus eliminating its electrical impact, the relative induction in the brain dropped to 3.6 % at the centre, despite the presence of the conducting liquid. Such results denote the vital importance of having a conductive layer to achieve high deep-brain stimulation power through the new TMS system.

The final milestone of the present work consisted of designing a new power electronics circuit able to drive the orthogonal configuration and deliver excitatory (high-frequency) TMS protocols. Two different configurations, using two types of fast-rate switches, were projected and tested under PSpice®, for which it was concluded that the damping ratio must fall below 0.2 in order to attain a biphasic TMS-induced pulse and also recover almost 60 % of the initial energy, from pulse to pulse. In addition, in order to guarantee that the energy available is kept constant for every pulse, a charging sub-circuit was proposed, which is capable of feeding the two configurations used. Initial simulations have shown that the proposed charging

circuit takes about 100 ms to fully charge the main circuit, thus being in compliance with the desired frequency of 10 Hz for the high-frequency rTMS device.

After these full, exhaustive simulation studies it is highly necessary to reach the validation of the simulation results obtained. This task requires the implementation of the orthogonal configuration prototype, including the construction of the large five coils which is being performed at the high-precision mechanical workshop of LIP, the construction of a spherical brain phantom with the same conductivity as the skull, by means of 3D printing and lastly the construction and positioning of the E-field and current density sensors and their sensitive readout electronics in order to measure the electric potential difference in several points of the head volume. Additional simulation studies should also be conducted in order to further optimise the shielding structure, namely by using more suitable materials such as Mu-Metal.

Finally, the stimulating power electronics must be fabricated in order to apply both high-frequency and low-frequency trains of stimuli via the proposed new TMS system, aiming to measure the resulting E-field distribution induced inside the conductive sphere and inside real human skulls, already kindly provided by the Department of Life Sciences of University of Coimbra. The skulls will allow studying experimental results obtained under the effect of real skull cavities. The head model and the skulls will be filled with a solution, which electrical conductivity must have the same value of the brain conductivity, namely 0.33 S/m.

Appendices

Appendix I

Description of the software and hardware used for the simulation studies and data processing

Finite element method: meshing considerations

In this work, the majority of the simulations were carried out in the COMSOL Multiphysics® AC/DC Module software which is based on the finite element method (FEM). This is a numeral technique through which the software solves a continuum problem such that the problem domain is divided into several, smaller parts, termed finite elements, that are described by a number of parameters. Over these elements, it is possible to define a set of simpler equations describing the solution to the governing complex equation in order to approximate solutions by minimising an associated error function. Therefore, this finite element mesh serves two purposes: dividing the geometry model into smaller pieces and represent the solution to the problem under study (Frei, 2013*a*).

There are four different types of finite elements that can be used to mesh a particular geometry: tetrahedra, hexahedra, prisms and pyramids, which are first order elements since they have straight lines and therefore approximate via a linear polynomial of type $y = ax + b$. Such elements can be seen in Figure I.1, where the grey circles represent the corners, or nodes of the elements (Frei, 2013*a*). The solution for each element is then computed at the node points, and a polynomial is used to interpolate all these solutions throughout the elements to recover the total solution field (Frei, 2013*a*). Within COMSOL Multiphysics®, tetrahedral elements

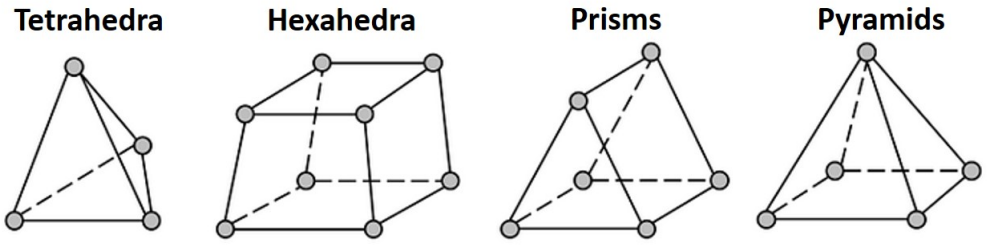

Figure I.1: Different types of elements to be used in the meshing of a particular geometry model. These are first order elements since they have straight edges which are represented by only two points.

are the default element type since any 3D volume, regardless of its shape, can be meshed with tetrahedral elements (Frei, 2013*b*). In this work, all the simulated volumes were meshed using first order tetrahedral elements.

Although it is possible to always compute a solution, no matter how coarse the mesh is, it may not be very accurate. Thus, as one refines the mesh, the solution will become more accurate (Frei, 2013*b*). After the construction of the geometry model, the mesh is selected within one of nine possible levels/sizes, *Extremely Coarse* >> *Extra Coarse* >> *Coarse* >> *Coarser* >> *Normal* >> *Fine* >> *Finer* >> *Extra Fine* >> *Extremely Fine*. By refining the mesh, towards the *Extremely Fine* level, the number of finite elements, considered for the calculation, significantly increases.

The most used mesh sizes were *Finer*, *Fine* and *Normal* levels. For some simulations the convergence of the solution lasted about 15 hours.

Software and hardware used

The AC/DC module is used for simulating electromagnetic phenomena. The COMSOL® AC/DC-based simulations were performed on a Dell® Optiplex 7010 computer with 4 CPUs Intel® i7, 3.40 GHz and 8 GB RAM.

The experimental data, presented in Chapter 3, was acquired using the PicoScope® 6 software and was processed using the MathWorks MATLAB® software on an ASUS® Notebook N61J Series computer with 4 CPUs Intel® i7, 1.60 GHz and 4 GB RAM.

Regarding the simulations of electrical circuits described in Chapter 5, the OrCAD®PSpice® software was used on an eMachines® EL1850 computer with a Intel Celeron® processor E3400, 2.60 GHz and 4 GB RAM.

Appendix II

Human head and torso models defined for the Comsol Multiphysics AC/DC simulations

For the simulation studies described along this project, it was necessary to create different domains, each one corresponding to a different tissue/material with its particular properties.

Although the head and torso models considered for the simulations were set as simplified representations, realistic properties and dimensions were taken into account when defining the corresponding domains in the simulation software.

For each study, the simulation software calculated the mesh of the finite elements of the several domains considered. Due to the existence of intersections between different domains, like the conducting liquid domain and the scalp domain, sometimes it was necessary to consider a third domain, resulting from such intersection. Figure II.2 illustrates this third domain, represented by the number 2 which resulted from the fact that the head model is only partly immersed in the conducting liquid and therefore the domain corresponding to the saline solution intersects the scalp domain.

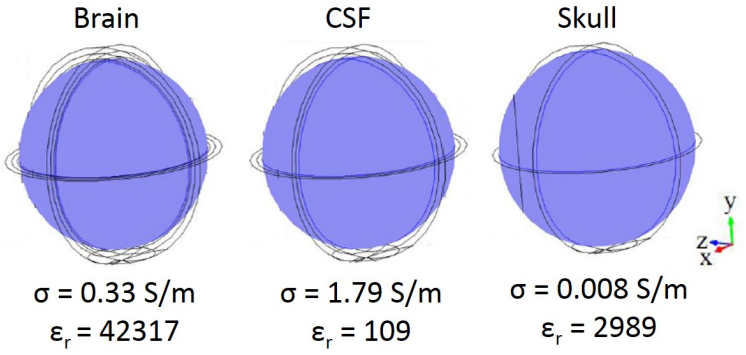

Figure II.1: Domains defined in the COMSOL Multiphysics AC/DC software, for the different head tissues. Brain (left), cerebrospinal fluid, CSF, (middle) and skull (right). The electrical conductivity (σ) and the relative permittivity (ϵ_r) are indicated below each image.

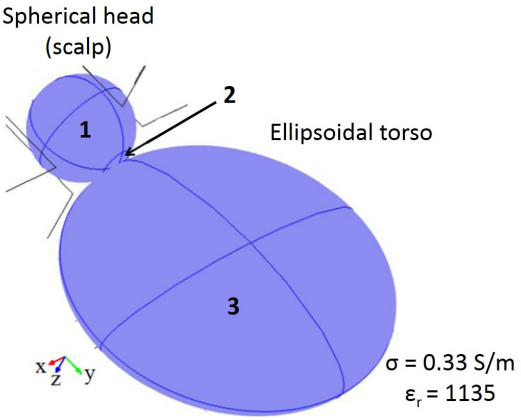

Figure II.2: Skin domains (scalp (1) and torso (3)) defined in the COMSOL Multiphysics AC/DC software, for the head and torso models. Due to the intersection of the fibreglass container with the head model it was necessary to consider a third domain, represented by the number 2. The electrical conductivity (σ) and the relative permittivity (ϵ_r) are also indicated on the right.

Appendix III

Method used to estimate the approximate position of the retinas within the head model used for the simulations

Once the eyes were not considered in the human head model used for the simulations, the following method was applied in order to estimate the position of the retinas (Sousa, 2014).

Assuming d as the depth of the retina and α as the angle between the hypothetical eye position and the central axis of the head model, as demonstrated in Figure III.1a. Considering the distance between the outer surface of the cornea and the retina as 2.4 cm (Hecht, 1987) and the dimension of the ocular cavity as 0.6 cm, the value of d was estimated as 3 cm.

A value of 6.5 cm was considered for the average adult interpupillary distance (Gross et al., 2008) and the angle α is given by:

$$\alpha = \tan^{-1}\left(\frac{0.5 \times 6.5}{10}\right) = 18^{\circ}$$

With the value of α and the depth of the retina in the head model it is relatively straightforward to estimate its position.

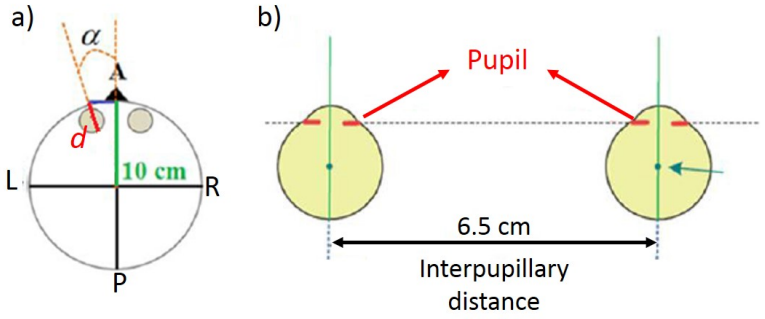

Figure III.1: Method used for the estimation of the position of the retinas. **(a)** Axial view of the head model with a radius of 10 cm. **(b)** Representation of the interpupillary distance. d: depth of the retina. α: angle between the eye position and the central axis of the head model. A: anterior. P: posterior. L: left. R: right.

Appendix IV

Simulation parameters and configurations in COMSOL Multiphysics® AC/DC software

Setting the surface of the volume of air as the infinity

When considering the spherical "world" of air surrounding the whole simulation apparatus, it was necessary to define the surface of the volume of air as the infinity, where the potential and the E-field are zero.

To do so, one must simply assign each one of the 8 sub-divisions of the spherical surface to the boundary condition defined by the equation $V = 0$, as demonstrated in Figure IV.1.

After following the steps, represented by the red numbers, it is possible to select each sub-domain and the condition $V = 0$ immediately becomes assigned to the selected sub-division.

Setting the value of the *Drop tolerance*

As explained before in Chapter 3, sometimes it is useful to alter the *Drop tolerance* parameter to a more suitable value in order to overcome the problems that do not allow the software to converge to a solution.

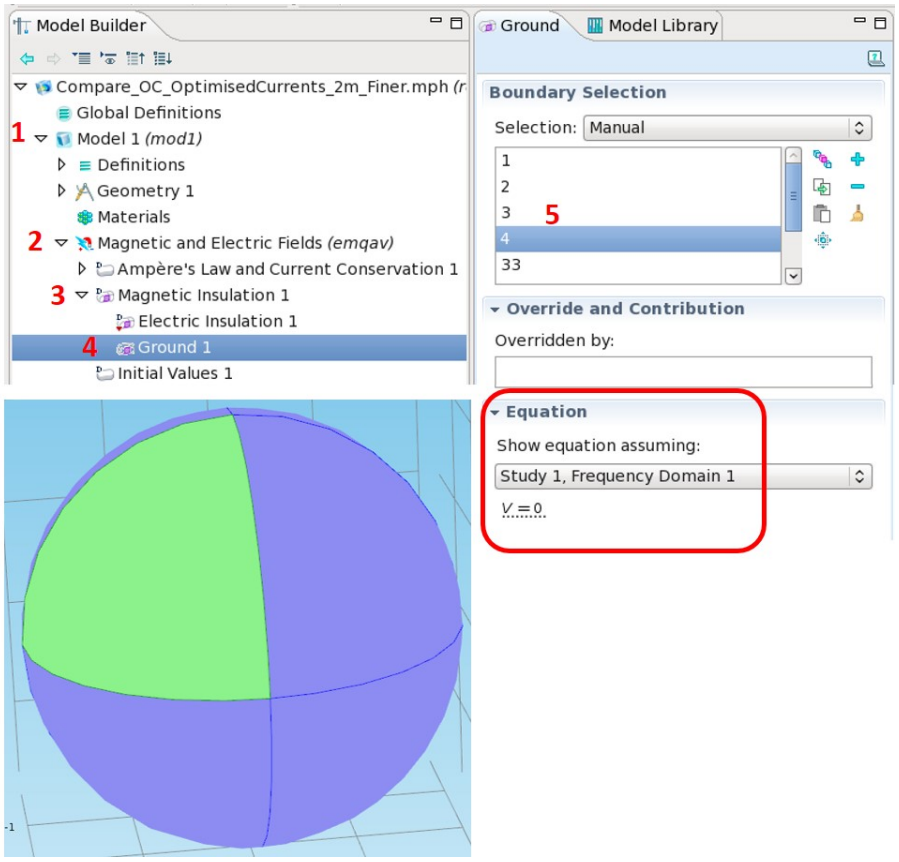

Figure IV.1: Steps required to set the spherical surface (purple sphere) as the infinity. One of the eight sub-divisions of the surface is represented in green which corresponds to sub-domain 4. The red numbers indicate the sequential steps that must be followed to define the boundary condition of zero potential at the surface.

The *Drop tolerance* factor reflects the number of finite elements that are neglected by the algorithm when computing the solution. Defining higher values for this parameter implies that more elements are neglected. As a result, less memory and computational time are needed while searching for the solution. However, for some particular problems and geometries, an higher *Drop tolerance* value prevents the software to converge to a final solution since the algorithm becomes less accurate as a result of considering fewer elements in the convergence process (COMSOL Inc., 2010).

Therefore, the main challenge is to achieve a compromise between the computational cost (time and memory) and the accuracy and precision of the iterative method in order to find the proper solution in the shortest time possible.

In this work, when the simulation model included a metal, for shielding purposes, the *Drop tolerance* had to be adjusted to $1 \cdot 10^{-6}$ instead of 0.01, which

was the value used for all the remaining simulations. The $1 \cdot 10^{-6}$ value was found through a trial and error method and was the only value allowing for the software to converge to a solution when simulating a shielding material. As expected, this adjustment significantly increased the simulation time from a few minutes (for a *Drop tolerance* of 0.01) up to 15 hours.

Figure IV.2 illustrates the steps that must be followed to modify the *Drop tolerance* parameter.

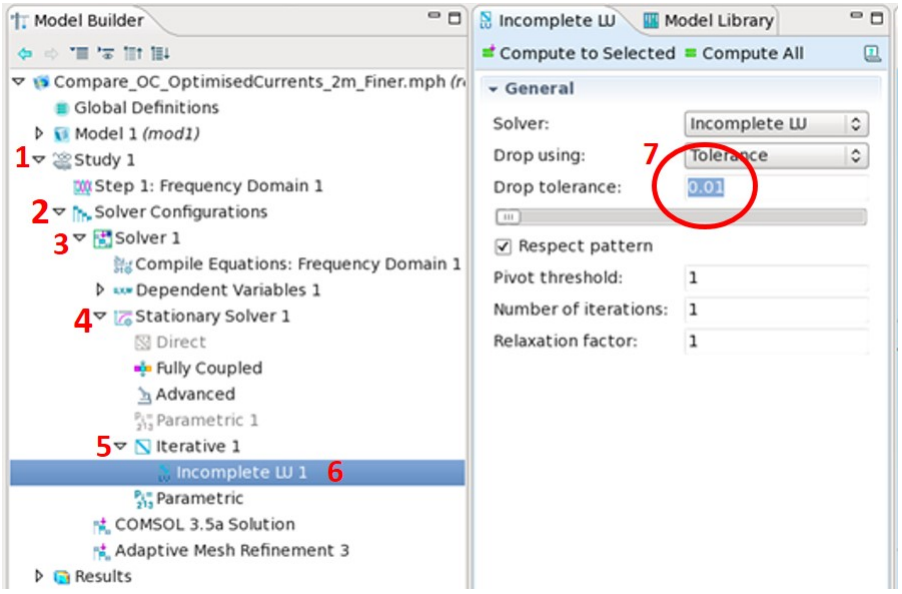

Figure IV.2: Steps required to set the *Drop tolerance* parameter.

Materials library in COMSOL Multiphysics® AC/DC

The properties of the shielding materials used in this work were obtained in the material browser of the COMSOL Multiphysics® AC/DC software, following the next steps: *Geometry menu >> Materials >> Open Material Browser >> Built-in Menu.*

An extensive list of materials is then presented along with the respective properties, such as electrical conductivity, relative permeability and density.

Appendix V

Current density induced by the previous orthogonal configuration in the fibreglass container surroundings

The presence of the conducting liquid was found to have no significant effect in the intensity of the current density induced in an ellipsoidal torso placed outside the fibreglass container.

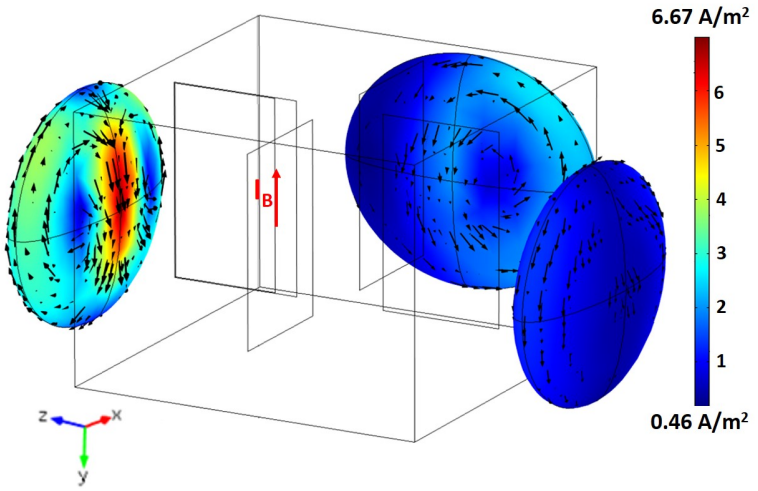

Figure V.1: Three-dimensional view of the three ellipsoidal torsos anteriorly, posteriorly and laterally located. Torsos are positioned 10 cm away from the container. The distribution (colour scale) and direction (arrows) of the induced current density in all three torsos is also illustrated as well as the direction of the current in coil B. Both the 5 coils and the patient head were surrounded by air. Arrows are represented in logarithmic scale.

When comparing with the situation when the 5 coils are surrounded by air, the main difference is associated with the direction of the induced currents in the torso which is opposite to that of the currents induced by the coils immersed in a saline solution, as demonstrated in Figure V.1 and Figure V.2.

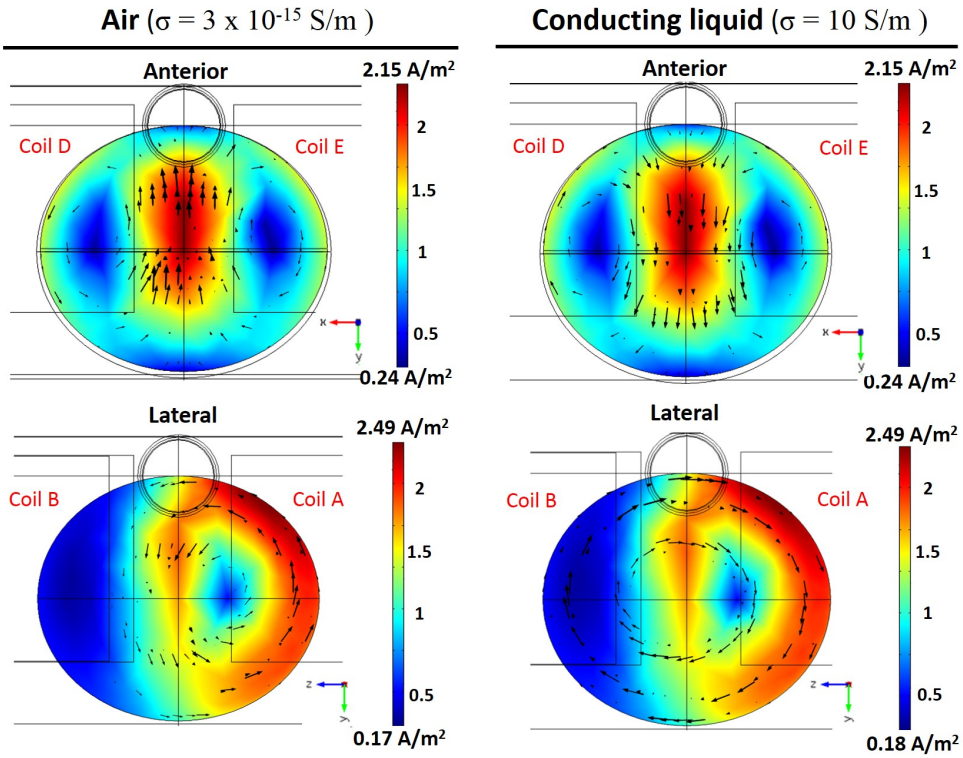

Figure V.2: Distribution (colour scale) and direction (arrows) of the current density in an ellipsoidal torso, located anteriorly and laterally to the patient, induced by the 5-coil system surrounded by air (left images) and conducting liquid (right images). Coils A, B, D and E are also represented.

Appendix VI

Considerations regarding the simulation of a metal shielding structure

The implementation of a shielding structure between the patient torso and the system of coils resulted in the need to add a neck for the patient model, as illustrated in Figure VI.1. Such adaptation was done mainly to prevent the metal structure to intersect the patient torso and thus increase the distance between the metal and the torso. The neck was modelled as a 6-cm radius cylinder with 6 cm height and an electrical conductivity similar to the torso and scalp (*i.e.* 0.33 S/m).

Considering the neck domain, it did not alter the head position and, therefore, had no significant effect in the induced $\vec{J}$ distribution. Through a study performed using the new OC system with the optimised currents it was found that the percentage relative errors were insignificant (below 1 %) for the $\vec{J}$ values observed

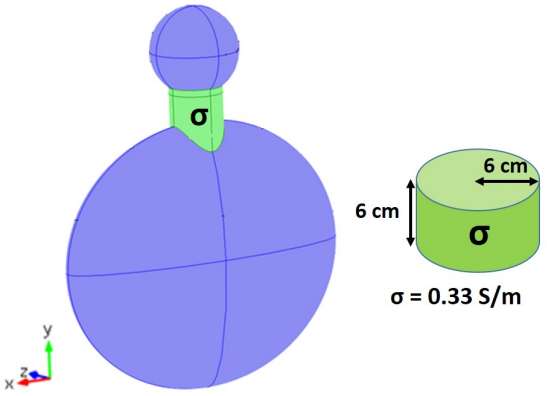

Figure VI.1: Three-dimensional view of the patient model with the three external domains, scalp, torso (blue) and neck (green). The cylindrical model of the neck is also illustrated with the respective dimensions. The neck has the same electrical conductivity as the skin (scalp and torso).

at the brain surface (maximum) and centre, comparing with the optimum results presented in Section 3.4.4.

Influence of having conducting liquid regarding the current density in the patient torso

By simulating the previous OC surrounded by a 1-m radius sphere of air it was possible to demonstrate that the existence of the conducting liquid is irrelevant to the induced current density in the patient torso. Considering the maximum values induced in the torso volume of 4.558 A/m^2 and 4.509 A/m^2 for the case with and without liquid, respectively, there is no significant difference between the two situations since $\delta x = 1.1$ %, thus inferior to 10 %.

Increasing the attenuation of the magnetic field by approaching the shield to the conducting liquid container

By approaching the metal slab to the fibreglass container, from 4 cm to 2 cm, the $\vec{J}$ induced in the patient torso decreased. The simulations were carried out using the previous OC surrounded by a 3.6-m radius sphere of air with an iron slab ($3\times3\times0.04$ m^3) positioned 4 cm and 2 cm away from the container. The maximum $\vec{J}$ in the torso volume decreased from 3.370 A/m^2 to 2.576 A/m^2 while the induced value in the heart dropped from 0.704 A/m^2 to 0.525 A/m^2.

Impact of using iron or aluminium as the shielding material on the current density induced in the patient torso

Table VI.1 demonstrates the similar results obtained in the patient torso when a metal slab made of iron or aluminium was simulated between the dTMS system and the torso. Three different simulation setups were tested. Even the $\vec{J}$ values observed in the metal slab are identical when using iron or aluminium. The first consisted of placing a 4-cm thick square metal slab (3×3 m^2), 2 cm apart from the fibreglass container, with the previous OC being surrounded by a 3.6-m radius volume of air. Setup 2 and 3 already used the optimised geometry of the new OC, shielded by a 0.5-cm thick and 4-cm thick metal slab, respectively. Again, the shield was considered to be 2 cm apart from the container.

Table VI.1: Current density values induced in the patient torso and in the shielding material itself after placing a metal (iron or aluminium) slab between the 5-coil system and the torso volume.

Setup	Iron				Aluminium			
	Torso (A/m^2)		Metal (A/m^2)		Torso (A/m^2)		Metal (A/m^2)	
	Max	Heart	Max	Min	Max	Heart	Max	Min
Setup 1	2.576	0.574	$4.911 \cdot 10^6$	1805	2.575	0.581	$4.911 \cdot 10^6$	1806
Setup 2	0.406	0.007	$7.777 \cdot 10^6$	$1.001 \cdot 10^4$	0.403	0.007	$8.949 \cdot 10^6$	$1.002 \cdot 10^4$
Setup 3	0.205	0.005	$1.278 \cdot 10^6$	363.6	0.205	0.004	$1.278 \cdot 10^6$	363.4

Appendix VII

Attenuation of the magnetic field via a 3-cm thick metal cage

By simulating the new optimised orthogonal configuration with and without a shielding structure, enclosing the fibreglass container, it was possible to see that the magnetic flux density is reduced at least by three orders of magnitude, when the shield is present. Figure VII.1 shows the magnetic flux density in a central slice of the surrounding world of air, for the two described situations.

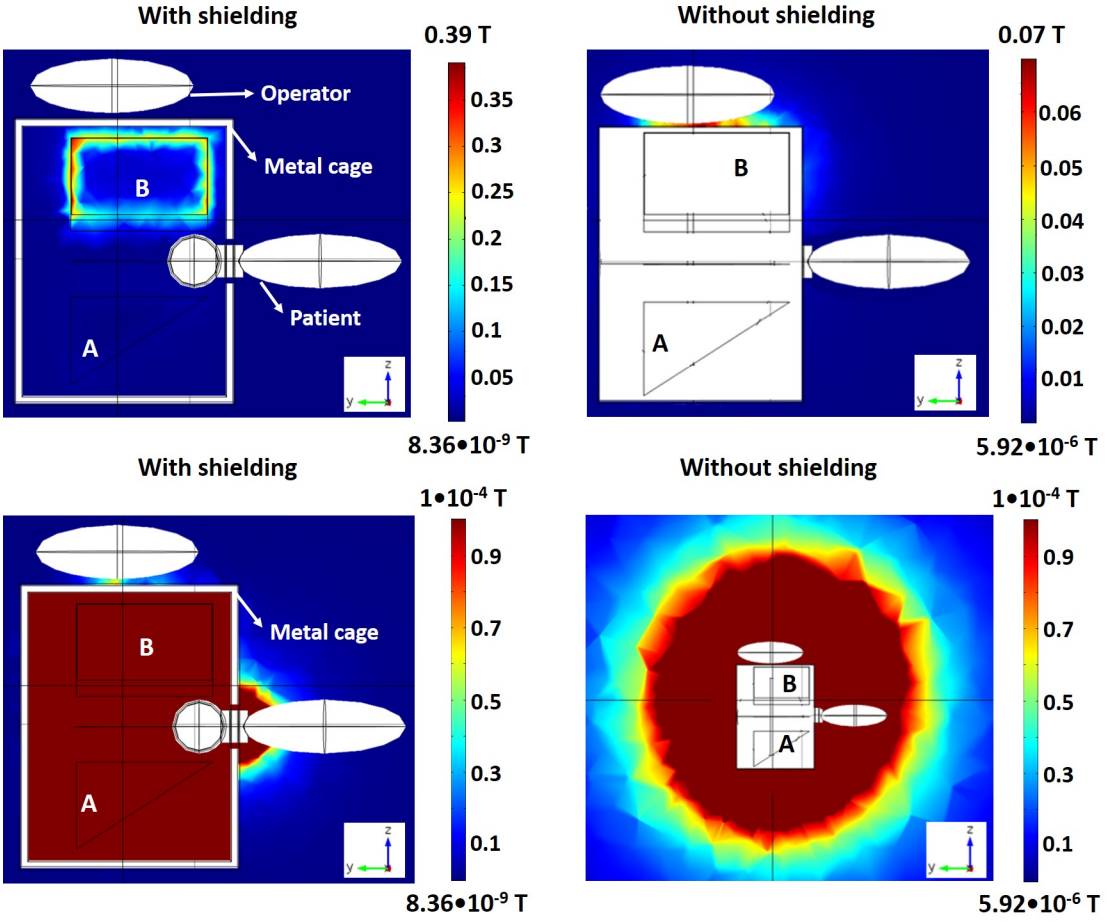

Figure VII.1: Distribution (colour scale) of the magnetic flux density, in tesla (T), for the situation where the metal cage is considered (left images) or absent (right images). The operator, posteriorly located, is represented as well as the patient. The images on the left (with shielding), represent a simulation without considering conducting liquid around the coils and the patient head. Therefore, there is also air inside the fibreglass container. In the images on the right (without shielding), the 5 coils and the head model are immersed in conducting liquid. In the two top figures, the colour scale was not modified. For the bottom images (left and right) the colour scale was truncated to a limit value of 0.1 mT. Coils A and B are also indicated.

As seen by the image in the top right corner of Figure VII.1, the magnetic flux density around the operator has an intensity of about $7 \cdot 10^{-2}$ T, when there is no shield between the coils and the operator.

However, when an iron structure is considered, surrounding the 5-coil system, the magnitude of the magnetic flux density drops to circa $7 \cdot 10^{-5}$ T, between the operator and the metal cage (see bottom left image of Figure VII.1), thus reflecting an attenuation by three orders of magnitude.

Appendix VIII

Current density induced in the several domains by the new orthogonal configuration

Figure VIII.1 shows the distribution and direction of the $\vec{J}$ induced in the scalp, skull and CSF domains of the head model and also in the conducting liquid near the smaller rectangular coil (coil B), where the $\vec{J}$ is higher.

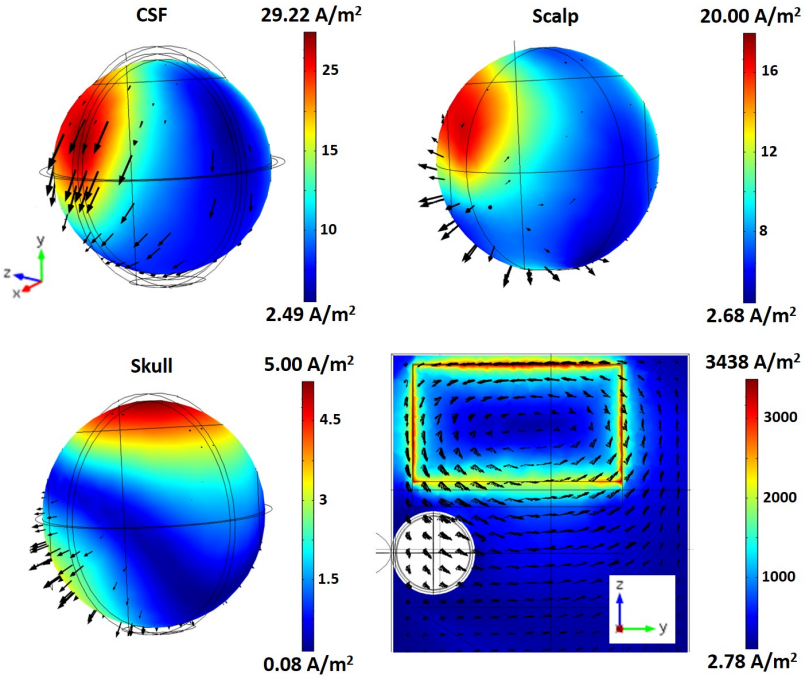

Figure VIII.1: Three-dimensional view of the distribution (colour scale) and direction (arrows) of the induced current density in the CSF, scalp and skull domains of the head model. On the bottom right corner, a central slice of the conducting liquid is depicted as well as the head model. The current passing trough the coil B is circulating in the $-y$ direction (inferior branch), opposite to the induced currents in the conducting liquid, flowing in the $+y$ direction.

Appendix IX

Influence of having an insulated wire in the current density distribution

In order to investigate the difference between having an insulated wire or a wire in direct contact with the conducting solution, a simulation was performed using a 2-cm radius circular coil, with a current of 3 kA, located above an animal head model. The tissue conductivities considered were very similar to the human head model. The results are illustrated in Figure IX.1.

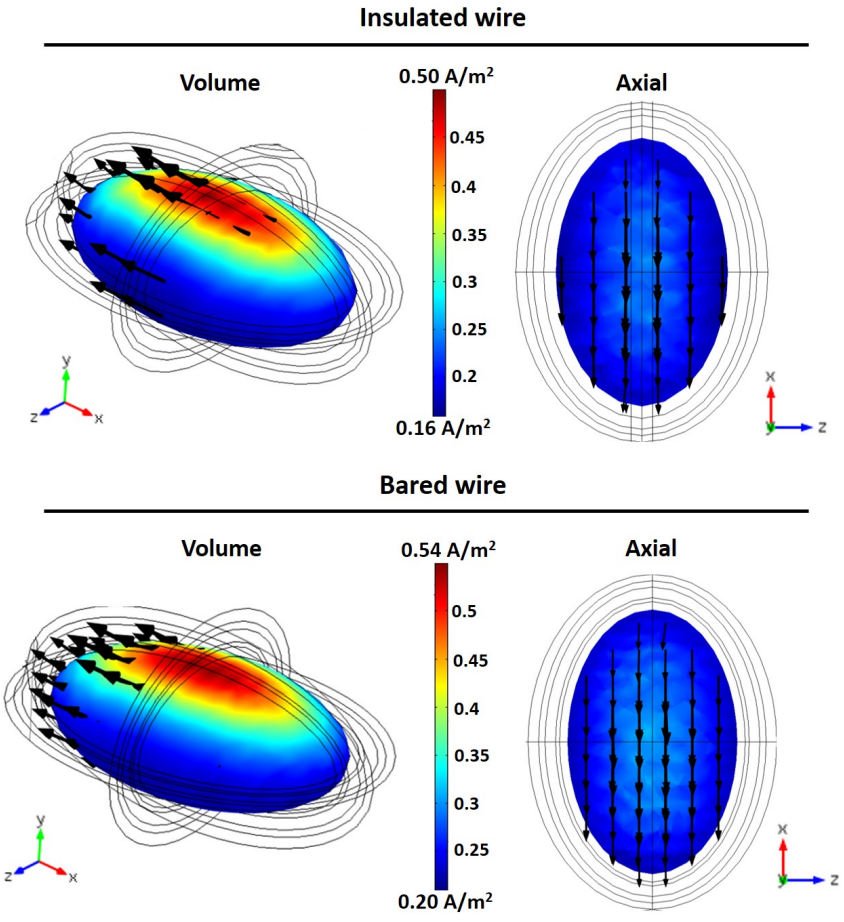

Figure IX.1: Three-dimensional view and central slice (axial view) of the distribution (colour scale) and direction (arrows) of the induced current density in an animal brain model. The stimulation was performed by an insulated circular coil (top images) and by a circular coil with bared wire (bottom images).

The distribution and direction of the induced $\vec{J}$ is quite similar between the two situations, although the RI at the centre of the brain dropped by five percentage

points when considering an insulating material around the coil.

Appendix X

Electrical conductivity of an aqueous solution

To achieve an electrical conductivity of 7 S/m in a saline solution used for the experimental tests, the amount of NaCl required was determined by the information presented in Table X.1.

Thus, for 427.46 g of water one must add 21.37 g (5%) of NaCl in order to get a NaCl solution with the desired σ of 7 S/m.

Table X.1: Electrical conductivity in S/m as a function of concentration, in mass percent. Adapted from (Weast, 1989, Wolf, 1966).

Electrolyte	**Concentration (mass percent)**				
	1 %	**2 %**	**5 %**	**10 %**	**20 %**
Sodium chloride	1.60	3.02	7.01	12.6	20.4

References

Agarwal, A. and Lang, J. H. (2005), *Foundations of Analog and Digital Electronic Circuits*, Morgan Kaufmann Publishers, Elsevier.

American Heart Association (2014), 'Ventricular Fibrillation'. [Accessed March 30th, 2015].
URL: *http://www.heart.org/HEARTORG/Conditions/Arrhythmia/AboutArrhythmia/Ventricular-Fibrillation_UCM_324063_Article.jsp*

Aydin-Abidin, S., Moliadze, V., Eysel, U. T. and Funke, K. (2006), 'Effects of repetitive TMS on visually evoked potentials and EEG in the anaesthetized cat: dependence on stimulus frequency and train duration.', *J. Physiol.* **574**(Pt 2), 443–455.

Bailey, W. H., Su, S. H., Bracken, T. D. and Kavet, R. (1997), 'Summary and evaluation of guidelines for occupational exposure to power frequency electric and magnetic fields.', *Health Phys.* **73**(3), 433–53.

Bakker, J. F., Paulides, M. M., Neufeld, E., Christ, a., Chen, X. L., Kuster, N. and van Rhoon, G. C. (2012), 'Children and adults exposed to low-frequency magnetic fields at the ICNIRP reference levels: theoretical assessment of the induced electric fields', *Phys. Med. Biol.* **57**(7), 1815–1829.

Barlow, H. B., Kohn, H. I. and Walsh, E. G. (1947), 'The effect of dark adaptation and of light upon the electric threshold of the human eye', *Am. J. Physiol.* **148**, 376–381.

Basic Electronics Tutorials (2015*a*), 'Insulated Gate Bipolar Transistor'. [Accessed June 2nd, 2015].
URL: *http://www.electronics-tutorials.ws/power/insulated-gate-bipolar-transistor.html*

Basic Electronics Tutorials (2015*b*), 'Thyristor Tutorial'. [Accessed June 2nd, 2015].
URL: *http://www.electronics-tutorials.ws/power/thyristor.html*

Baumann, S. B., Wozny, D. R., Kelly, S. K. and Meno, F. M. (1997), 'The electrical conductivity of human cerebrospinal fluid at body temperature', *IEEE Trans. Biomed. Eng.* **44**(3), 220–225.

Belmaker, R. H. and Agam, G. (2008), 'Major Depressive Disorder', *N. Engl. J. Med.* **358**, 55–68.

Berlucchi, G. and Buchtel, H. A. (2008), 'Neuronal plasticity: historical roots and evolution of meaning', *Exp. Brain Res.* **192**(3), 307–319.

Bersani, F. S., Minichino, A., Enticott, P. G., Mazzarini, L., Khan, N., Antonacci, G., Raccah, R. N., Salviati, M., Delle Chiaie, R., Bersani, G., Fitzgerald, P. B. and Biondi, M. (2013), 'Deep transcranial magnetic stimulation as a treatment for psychiatric disorders: A comprehensive review', *Eur. Psychiatry* **28**(1), 30–39.

Bestmann, S. (2008), 'The physiological basis of transcranial magnetic stimulation.', *Trends Cogn. Sci.* **12**(3), 81–83.

Bliss, T. V. and Cooke, S. F. (2011), 'Long-term potentiation and long-term depression: a clinical perspective', *Clinics* **1**, 3–17.

Brainsway (2013*a*), 'Brainsway Receives CE Marketing Approval for Treatment of Autism, Alzheimer's and Smoking Cessation'. [Accessed June 1st, 2015].
URL: *http://www.brainsway.com/press_release/brainsway-receives-ce-marketing-approval-treatment-autism-alzheimers-and-smoking*

Brainsway (2013*b*), 'Brainsway Receives FDA Approval'. [Accessed June 1st, 2015].
URL: *http://www.brainsway.com/press_release/brainsway-receives-fda-approval*

Brainsway (2014*a*), 'Brainsway Receives Brazilian ANVISA Approval for Treating Six Brain Disorders'. [Accessed June 1st, 2015].
URL: *http://www.brainsway.com/press_release/brainsway-receives-brazilian-anvisa-approval-treating-six-brain-disorders*

Brainsway (2014*b*), 'Brainsway Receives CE Approvals for Treating Multiple Sclerosis (MS), Stroke and Obsessive Compulsive Disorder (OCD)'. [Accessed June 1st, 2015].
URL: *http://www.brainsway.com/press_release/brainsway-receives-ce-approvals-treating-multiple-sclerosis-ms-stroke-and-obsessive*

Brainsway (2015), 'Deep TMS Indications'. [Accessed June 1st, 2015].
URL: *http://www.brainsway.com/researchers-portal*

Brodal, P. (2010), *The Central Nervous System: Structure and Function*, Oxford University Press.

Burke, D., Bartley, K., Woodforth, I. J., Yakoubi, a. and Stephen, J. P. (2000), 'The effects of a volatile anaesthetic on the excitability of human corticospinal axons.', *Brain* **123**(Pt 5), 992–1000.

Bush, G., Luu, P. and Posner, M. I. (2000), 'Cognitive and emotional influences in anterior cingulate cortex', *Trends Cogn. Sci.* **4**(6), 215–222.

Cadence Design Systems Inc. (2015), 'OrCAD EE (PSpice) Designer'. [Accessed June 3rd, 2015].
URL: *http://www.orcad.com/products/orcad-pspice-designer/overview*

Chen, R., Cros, D., Curra, A., Di Lazzaro, V., Lefaucheur, J. P., Magistris, M. R., Mills, K., Rösler, K. M., Triggs, W. J., Ugawa, Y. and Ziemann, U. (2008), 'The clinical diagnostic utility of transcranial magnetic stimulation: Report of an IFCN committee', *Clin. Neurophysiol.* **119**(3), 504–532.

Chieffo, R., De Prezzo, S. and Leocani, L. (2014), 'Deep repetitive transcranial magnetic stimulation with h-coil on lower limb motor function in chronic stroke: A pilot study', *Arch. Phys. Med. Rehabil.* **95**(6), 1141–1147.

Chieffo, R., Ferrari, F. and Leocani, L. (2014), 'Excitatory deep transcranial magnetic stimulation with H-coil over the right homologous Broca's region improves naming in chronic post-stroke aphasia.', *Neurorehabil. Neural Repair* **28**(3), 291–298.

Clapp, P., Bhave, S. V. and Hoffman, P. L. (2010), 'How Adaptation of the Brain to Alcohol Leads to Dependence : A Pharmacological Perspective', *Alcohol Res Heal.* **31**(4), 310–339.

COMSOL Inc. (2010), 'COMSOL Multiphysics Reference Guide: Version COMSOL 4.0a'.

COMSOL Inc. (2015), 'COMSOL Multiphysics AC/DC Module'. [Accessed June 3rd, 2015].
URL: *https://www.comsol.pt/acdc-module*

Cooke, S. F. and Bliss, T. V. P. (2006), 'Plasticity in the human central nervous system', *Brain* **129**(7), 1659–1673.

Coop, A. D., McKay, D. R., Lancaster, J. and Fox, P. T. (2010), 'Single neuron electrophysiology of transcranial magnetic stimulation. I. Passive responses', *BMC Neurosci.* **11**(Suppl 1), P86.

Costa, M. M. R. R. and Marques de Almeida, M. J. B. (2012), *Fundamentos de Física*, 3rd edn, Edições Almedina, S.A., Coimbra.

Counter, S. a. and Borg, E. (1992), 'Analysis of the coil generated impulse noise in extracranial magnetic stimulation.', *Electroencephalogr. Clin. Neurophysiol.* **85**, 280–288.

Currà, A., Modugno, N., Inghilleri, M., Manfredi, M., Hallett, M. and Berardelli, A. (2002), 'Transcranial magnetic stimulation techniques in clinical investigation.', *Neurology* **59**(12), 1851–1859.

Deng, Z.-D., Lisanby, S. H. and Peterchev, A. V. (2013*a*), 'Coil design considerations for deep transcranial magnetic stimulation.', *Clin. Neurophysiol.* **125**(6), 1202–1212.

Deng, Z.-D., Lisanby, S. H. and Peterchev, A. V. (2013*b*), 'Electric field depth-focality tradeoff in trancranial magnetic stimulation : simulation comparison of 50 coil designs', *Brain Stimul.* **6**(1), 1–13.

Di Lazzaro, V., Dileone, M., Pilato, F., Profice, P., Cioni, B., Meglio, M., Papacci, F., Sabatelli, M., Musumeci, G., Ranieri, F. and Tonali, P. a. (2010), 'Long-term motor cortex stimulation for amyotrophic lateral sclerosis', *Brain Stimul.* **3**(1), 22–27.

Downar, J. and Daskalakis, Z. J. (2013), 'New targets for rTMS in depression: A review of convergent evidence', *Brain Stimul.* **6**(3), 231–240.

Enticott, P. G., Fitzgibbon, B. M., Kennedy, H. a., Arnold, S. L., Elliot, D., Peachey, A., Zangen, A. and Fitzgerald, P. B. (2014), 'A double-blind, randomized trial of deep Repetitive Transcranial Magnetic Stimulation (rTMS) for autism spectrum disorder', *Brain Stimul.* **7**(2), 206–211.

Epstein, C. M. (2008), 'A six-pound battery-powered portable transcranial magnetic stimulator', *Brain Stimul.* **1**(2), 128–130.

Faraday, M. (1832), 'Experimental Researches in Electricity', *Philos. Trans. R. Soc. London* **122**(0), 125–162.

Farzan, F. (2014), Single-Pulse Transcranial Magnetic Stimulation (TMS) Protocols and Outcome Measures, *in* A. Rotenberg, J. C. Horvath and A. Pascual-Leone, eds, 'Transcranial Magn. Stimul. Neuromethods, vol. 89', Springer, chapter 5, p. 384.

Fitzgerald, P. B., Fountain, S. and Daskalakis, Z. J. (2006), 'A comprehensive review of the effects of rTMS on motor cortical excitability and inhibition', *Clin. Neurophysiol.* **117**(12), 2584–2596.

Frei, W. (2013*a*), 'Meshing Considerations for Linear Static Problems'.
URL: *https://www.comsol.com/blogs/meshing-considerations-linear-static-problems/*

Frei, W. (2013*b*), 'Meshing your Geometry: When to Use the Various Element Types'.
URL: *http://www.comsol.com/blogs/meshing-your-geometry-various-element-types/*

Gonçalves, S. I., De Munck, J. C., Verbunt, J. P. a., Bijma, F., Heethaar, R. M. and Lopes da Silva, F. (2003), 'In vivo measurement of the brain and skull resistivities using an EIT-based method and realistic models for the head', *IEEE Trans. Biomed. Eng.* **50**(6), 754–767.

Gross, H., Blechinger, F. and Achtner, B. (2008), *Handbook of Optical Systems, Volume 4, Survey of Optical Instruments*, John Wiley & Sons, Inc.

Guse, B., Falkai, P. and Wobrock, T. (2010), 'Cognitive effects of high-frequency repetitive transcranial magnetic stimulation: A systematic review', *J. Neural Transm.* **117**(1), 105–122.

Hecht, E. (1987), *Optics 2nd Edition*, Addison-Wesley.

Heller, L. and van Hulsteyn, D. B. (1992), 'Brain stimulation using electromagnetic sources: theoretical aspects.', *Biophys. J.* **63**(1), 129–138.

Hirata, A., Takano, Y., Fujiwara, O., Dovan, T. and Kavet, R. (2011), 'An electric field induced in the retina and brain at threshold magnetic flux density causing magnetophosphenes.', *Phys. Med. Biol.* **56**(13), 4091–4101.

Horvath, J. C., Perez, J. M., Forrow, L., Fregni, F. and Pascual-Leone, A. (2011), 'Transcranial magnetic stimulation: a historical evaluation and future prognosis of therapeutically relevant ethical concerns.', *J. Med. Ethics* **37**(3), 137–143.

ICNIRP (1998), 'ICNIRP Guidelines for limiting exposure to time varying electric, magnetic and electromagnetic fields (up to 300 GHz)', *Health Phys.* **74**, 494–523.

ICNIRP (2003), 'Guidance on determining compliance of exposure to pulsed and complex non-sinusoidal waveforms below 100 kHz with International Commission on Non-Ionizing Radiation Protection guidelines.', *Health Phys.* **84**(3), 383–387.

ICNIRP (2010), 'ICNIRP statement — guidelines for limiting exposure to time-varying electric and magnetic fields (1 Hz to 100 kHz) International Commission on Non-Ionizing Radiation Protection', *Health Phys* .

Irwin, J. D. and Nelms, R. M. (2010), *Basic Engineering Circuit Analysis*, tenth edit edn, John Wiley & Sons, Inc.

Isserles, M., Rosenberg, O., Dannon, P., Levkovitz, Y., Kotler, M., Deutsch, F., Lerer, B. and Zangen, A. (2011), 'Cognitive-emotional reactivation during deep transcranial magnetic stimulation over the prefrontal cortex of depressive patients affects antidepressant outcome', *J. Affect. Disord.* **128**(3), 235–242.

Izquierdo, I., Quillfeldt, J. A., Zanatta, M. S., Quevedo, J., Schaeffer, E., Schmitz, P. K. and Medina, J. H. (1997), 'Sequential Role of Hippocampus and Amygdala, Entorhinal Cortex and Parietal Cortex in Formation and Retrieval of Memory for Inhibitory Avoidance in Rats', *Eur. J. Neurosci.* **9**(4), 786–793.

Jiles, D. C. (1998), *Introduction to Magnetism and Magnetic Materials, Second Edition*, CRC Press.

Karlström, E. F., Lundström, R., Stensson, O. and Mild, K. H. (2006), 'Therapeutic staff exposure to magnetic field pulses during TMS/rTMS treatments', *Bioelectromagnetics* **27**(2), 156–158.

Kobayashi, M. and Pascual-Leone, A. (2003), 'Transcranial magnetic stimulation in neurology', *Lancet Neurol.* **2**(3), 145–156.

Kolin, A., Brill, N. Q. and Broberg, P. J. (1959), 'Stimulation of Irritable Tissues by Means of an Alternating Magnetic Field.', *Exp. Biol. Med.* **102**(1), 251–253.

Kowalski, T., Silny, J. and Buchner, H. (2002), 'Current Density Threshold for the Stimulation of Neurons in the Motor Cortex Area', *Bioelectromagnetics* **23**(6), 421–428.

Kujirai, T., Caramia, M. D., Rothwell, J. C., Day, B. L., Thompson, P. D., Ferbert, A., Wroe, S., Asselman, P. and Marsden, C. D. (1993), 'Corticocortical Inhibition In Human Motor Cortex', *J. Physiol.* **471**, 501–519.

Laakso, I. and Hirata, A. (2012), 'Computational analysis of thresholds for magnetophosphenes', *Phys. Med. Biol.* **57**(19), 6147–6165.

Lamm, C. and Singer, T. (2010), 'The role of anterior insular cortex in social emotions.', *Brain Struct. Funct.* **214**(5-6), 579–91.

Less EMF Inc. (2015), 'Magnetic Field Shielding'. [Accessed June 10th, 2015].
URL: *http:// www.lessemf.com/ mag-shld.html*

Levkovitz, Y., Harel, E. V., Roth, Y., Braw, Y., Most, D., Katz, L. N., Sheer, A., Gersner, R. and Zangen, A. (2009), 'Deep transcranial magnetic stimulation over the prefrontal cortex: Evaluation of antidepressant and cognitive effects in depressive patients', *Brain Stimul.* **2**(4), 188–200.

Levkovitz, Y., Rabany, L., Harel, E. V. and Zangen, A. (2011), 'Deep transcranial magnetic stimulation add-on for treatment of negative symptoms and cognitive deficits of schizophrenia: a feasibility study.', *Int. J. Neuropsychopharmacol.* **14**(7), 991–996.

Levkovitz, Y., Roth, Y., Harel, E. V., Braw, Y., Sheer, A. and Zangen, A. (2007), 'A randomized controlled feasibility and safety study of deep transcranial magnetic stimulation', *Clin. Neurophysiol.* **118**(12), 2730–2744.

Lipton, R. B., Dodick, D. W., Silberstein, S. D., Saper, J. R., Aurora, S. K., Pearlman, S. H., Fischell, R. E., Ruppel, P. L. and Goadsby, P. J. (2010), 'Single-pulse transcranial magnetic stimulation for acute treatment of migraine with aura: a randomised, double-blind, parallel-group, sham-controlled trial', *Lancet Neurol.* **9**(4), 373–380.

Loo, C. K., McFarquhar, T. F. and Mitchell, P. B. (2008), 'A review of the safety of repetitive transcranial magnetic stimulation as a clinical treatment for depression.', *Int. J. Neuropsychopharmacol.* **11**, 131–147.

Lövsund, P., Oberg, P. a., Nilsson, S. E. and Reuter, T. (1980), 'Magnetophosphenes: a quantitative analysis of thresholds.', *Med. Biol. Eng. Comput.* **18**(3), 326–334.

Maccabee, P. J., Eberle, L., Amassian, V. E., Cracco, R. Q., Rudell, a. and Jayachandra, M. (1990), 'Spatial distribution of the electric field induced in volume by round and figure '8' magnetic coils: relevance to activation of sensory nerve fibers.', *Electroencephalogr. Clin. Neurophysiol.* **76**(2), 131–141.

Mackay, W. A. (2009), *Neurofisiologia sem lágrimas*, 4ª edição edn, Fundação Calouste Gulbenkian.

Maeda, F., Keenan, J. P., Tormos, J. M., Topka, H. and Pascual-Leone, a. (2000), 'Modulation of corticospinal excitability by repetitive transcranial magnetic stimulation.', *Clin. Neurophysiol.* **111**(5), 800–805.

Magnetic Shield Corporation (2014), 'Magnetic Fields & Shields Overview'.

Miranda, P. C. (2013), 'Physics of effects of transcranial brain stimulation.', *Handb. Clin. Neurol.* **116**, 353–66.

Najib, U., Bashir, S. and Edwards, D. (2011), 'Transcranial brain stimulation: clinical applications and future directions', *Neurosurg. Clin. North Am.* **22**(2), 233–259.

Najib, U. and Horvath, J. C. (2014), Transcranial Magnetic Stimulation (TMS) Safety Considerations and Recommendations, *in* A. Rotenberg, J. C. Horvath and A. Pascual-Leone, eds, 'Transcranial Magn. Stimul. Neuromethods, vol. 89', Humana Press, chapter Chapter 2, p. 384.

National Institute of Neurological Disorders and Stroke (2008), 'Know Stroke. Know the Signs. Act in Time.'. [Accessed June 1st, 2015].
URL: *http://www.ninds.nih.gov/disorders/stroke/knowstroke.htm*

Nowak, K., Mix, E., Gimsa, J., Strauss, U., Sriperumbudur, K. K., Benecke, R. and Gimsa, U. (2011), 'Optimizing a rodent model of Parkinson's disease for exploring the effects and mechanisms of deep brain stimulation.', *Parkinsons. Dis.* **2011**, 414682.

Oberman, L. (2014), Repetitive Transcranial Magnetic Stimulation (rTMS) Protocols, *in* A. Rotenberg, J. C. Horvath and A. Pascual-Leone, eds, 'Transcranial Magn. Stimul. Neuromethods, vol. 89', Springer Protocols, chapter Chapter 7, p. 384.

Oberman, L., Eldaief, M., Fecteau, S., Ifert-Miller, F., Tormos, J. M. and Pascual-Leone, A. (2012), 'Abnormal modulation of corticospinal excitability in adults with Asperger's syndrome', *Eur. J. Neurosci.* **36**(6), 2782–2788.

Oliveira, H., Ferreira, C., Silva, M., Fonte, P., Salvador, R. and Crespo, P. (2012), 'Multiple coils excited at single or multiple frequencies in a conducting liquid for deep and whole-brain transcranial magnetic stimulation. I. Single-Frequency Excitation', *Current* pp. 1–6.

Opitz, A., Legon, W., Rowlands, A., Bickel, W. K., Paulus, W. and Tyler, W. J. (2013), 'Physiological observations validate finite element models for estimating subject-specific electric field distributions induced by transcranial magnetic stimulation of the human motor cortex', *Neuroimage* **81**, 253–364.

Parlamento Europeu and Conselho da União Europeia (2013), 'Directiva 2013/35/UE relativa às prescrições mínimas de segurança e saúde em matéria de exposição dos trabalhadores aos riscos devidos aos agentes físicos (campos electromagnéticos)', **2013**, 1–21.

Pascual-Leone, A., Valls-Solé, J., Wassermann, E. M. and Hallett, M. (1994), 'Responses to rapid-rate transcranial magnetic stimulation of the human motor cortex.', *Brain* **117**, 847–858.

Pawar, S. D., Murugavel, P. and Lal, D. M. (2009), 'Effect of relative humidity and sea level pressure on electrical conductivity of air over Indian Ocean', *J. Geophys. Res. Atmos.* **114**(2), 1–8.

Perret, R. (2009), *Power electronics semiconductor devices*, John Wiley & Sons, Inc.

Peterchev, A. V., Jalinous, R. and Lisanby, S. H. (2008), 'A transcranial magnetic stimulator inducing near-rectangular pulses with controllable pulse width (cTMS)', *IEEE Trans. Biomed. Eng.* **55**(1), 257–266.

Pico Technology Ltd. (2013), 'PicoScope 2203 PC Oscilloscopes: Users's Guide'. [Accessed June 22nd, 2015].
URL: *https://www.picotech.com/download/manuals/ps2203.en-4.pdf*

Pico Technology Ltd. (2015), 'PicoScope 6 Software: Beginner's Guide'. [Accessed June 22nd, 2015].
URL: *https://www.picotech.com/download/manuals/BeginnersGuideToPicoScope.pdf*

Reilly, J. P. (1991), 'Magnetic field excitation of peripheral nerves and the heart: a comparison of thresholds.', *Med. Biol. Eng. Comput.* **29**(6), 571–579.

Reilly, J. P. (2002), 'Neuroelectric mechanisms applied to low frequency electric and magnetic field exposure guidelines–part I: sinusoidal waveforms.', *Health Phys.* **83**(3), 341–55.

Robertson, E. M., Théoret, H. and Pascual-Leone, a. (2003), 'Studies in cognition: the problems solved and created by transcranial magnetic stimulation.', *J. Cogn. Neurosci.* **15**(7), 948–960.

Rosenberg, O., Gersner, R., Klein, L., Kotler, M., Zangen, A. and Dannon, P. (2012), 'Deep transcranial magnetic stimulation add-on for the treatment of auditory hallucinations: a double-blind study', *Ann. Gen. Psychiatry* **11**(1), 13.

Rosenberg, O., Roth, Y., Kotler, M., Zangen, A. and Dannon, P. (2011), 'Deep transcranial magnetic stimulation for the treatment of auditory hallucinations: a preliminary open-label study.', *Ann. Gen. Psychiatry* **10**(1), 3.

Rosenberg, O., Shoenfeld, N., Zangen, a., Kotler, M. and Dannon, P. N. (2010), 'Deep TMS in a resistant major depressive disorder: A brief report', *Depress. Anxiety* **27**(5), 465–469.

Rossi, S., Hallett, M., Rossini, P. and Pascual-Leone, A. (2009), 'Safety, ethical considerations, and application guidelines for the use of transcranial magnetic stimulation in clinical practice and research', *Clin. Neurophysiol.* **120**, 2008–2039.

Rotenberg, A., Horvath, J. C. and Pascual-Leone, A. (2014), The Transcranial Magnetic Stimulation (TMS) Device and Foundational Techniques, *in* A. Rotenberg, J. C. Horvath and A. Pascual-Leone, eds, 'Transcranial Magn. Stimul. Neuromethods, vol. 89', Springer, chapter 1, p. 384.

Roth, Y., Amir, A., Levkovitz, Y. and Zangen, A. (2007), 'Three-Dimensional Distribution of the Electric Field Induced in the Brain by Transcranial Magnetic Stimulation Using Figure-8 and Deep H-Coils', *Clin. Neurophysiol.* **24**(1), 31–38.

Roth, Y., Padberg, F. and Zangen, A. (2007), 'Transcranial magnetic stimulation of deep brain regions: Principles and methods', *Adv. Biol. Psychiatry* **23**, 204–224.

Roth, Y. and Zangen, A. (2012), Basic Principles and Methodological Aspects of Transcranial Magnetic Stimulation, *in* C. Miniussi, W. Paulus and P. M. Rossini, eds, 'Transcranial Brain Stimul.', CRC Press, chapter 1.

Roth, Y. and Zangen, A. (2014*a*), Reaching Deep Brain Structures: The H-Coils, *in* A. Rotenberg, J. C. Horvath and A. Pascual-Leone, eds, 'Transcranial Magn. Stimul. Neuromethods, vol. 89', Springer Protocols, chapter 4, p. 384.

Roth, Y. and Zangen, A. (2014*b*), Transcranial Magnetic Stimulation of Deep Brain Regions, *in* J. D. Bronzino and D. R. Peterson, eds, 'Biomed. Eng. Fundam.', 4 edn, CRC Press.

Ruohonen, J. and Ilmoniemi, R. J. (2005), Basic Physics and Design of Transcranial Magnetic Stimulation Devices and Coils, *in* M. Hallett and S. Chokroverty, eds, 'Magn. Stimul. Clin. Neurophysiol.', Elsevier Health Sciences, p. 457.

Sackeim, H. A., Prudic, J., Devanand, D., Kiersky, J., Fitzsimons, L., Bobba, J. M., McElhiney, M. C., Coleman, E. and Settembrino, J. (1993), 'Effects of Stimulus Intensity and Electrode Placement on the Efficacy and Cognitive Effects of Electroconvulsive Therapy', *N. Engl. J. Med.* **328**(12), 839–846.

Schmierer, K., Parkes, H. G., So, P.-W., An, S. F., Brandner, S., Ordidge, R. J., Yousry, T. A. and Miller, D. H. (2010), 'High field (9.4 Tesla) magnetic resonance imaging of cortical grey matter lesions in multiple sclerosis.', *Brain* **133**(Pt 3), 858–67.

Sekino, M. (2011), 'Development of magnetic stimulators - Department of Neuromodulation and Neurosurgery, Osaka University'. [Accessed April 24th, 2015].
URL: *http://www.neuromod.med.osaka-u.ac.jp/eng/project.html*

Silva, M., Ferreira, C., Oliveira, H., Fonte, P., Jesus, L., Salvador, R., Silvestre, J. and Crespo, P. (2012), 'Multiple coils excited at single or multiple frequencies in a conducting liquid for deep and whole-brain transcranial magnetic stimulation. II. Multiple-frequency excitation', *Current* pp. 1–6.

Simões, H., Dias Silva, M., Vieira Ferreira, C., Jesus, L., Oliveira, H., Miranda, P. C., Salvador, R., Crespo, P. and Silvestre, J. (2013), 'Experimental demonstration of induction by means of a transcranial magnetic stimulator coil immersed in a conducting liquid', *3rd Port. Bioeng. Meet. ENBENG 2013 - B. Proc.* pp. 2–5.

Sommer, M., Alfaro, A., Rummel, M., Speck, S., Lang, N., Tings, T. and Paulus, W. (2006), 'Half sine, monophasic and biphasic transcranial magnetic stimulation of the human motor cortex', *Clin. Neurophysiol.* **117**(4), 838–844.

Sousa, S. C. P. (2014), 'Otimização de um Dispositivo de Estimulação Magnética Transcraniana'.

Sousa, S. C. P., Almeida, J., Miranda, P. C., Salvador, R., Silvestre, J. a., Simões, H. and Crespo, P. (2014), 'Optimization of multiple coils immersed in a conducting liquid for half-hemisphere or whole-brain deep transcranial magnetic stimulation: A simulation study', *36th Annu. Int. Conf. IEE Eng. Med. Biol. Soc.* .

Stanford, A. D., Sharif, Z., Corcoran, C., Urban, N., Malaspina, D. and Lisanby, S. H. (2008), 'rTMS strategies for the study and treatment of schizophrenia: a review.', *Int. J. Neuropsychopharmacol.* **11**(4), 563–576.

The Internet Stroke Center: National Institute of Neurological Disorders and Stroke (2015), 'What is a Stroke?'. [Accessed June 1st, 2015].
URL: *http://www.strokecenter.org/patients/about-stroke/what-is-a-stroke/*

The MathWorks Inc. (2015), 'MATLAB: The Language of Technical Computing'. [Accessed June 3rd, 2015].
URL: *http://www.mathworks.com/products/matlab/*

Thut, G., Northoff, G., Ives, J. R., Kamitani, Y., Pfennig, a., Kampmann, F., Schomer, D. L. and Pascual-Leone, A. (2003), 'Effects of single-pulse transcranial magnetic stimulation (TMS) on functional brain activity: A combined event-related TMS and evoked potential study', *Clin. Neurophysiol.* **114**(11), 2071–2080.

Tofts, P. S. and Branston, N. M. (1991), 'The measurement of electric field, and the influence of surface charge, in magnetic stimulation.', *Electroencephalogr. Clin. Neurophysiol.* **81**(3), 238–239.

Vahabzadeh-Hagh, A. (2014), Paired-Pulse Transcranial Magnetic Stimulation (TMS) Protocols, *in* A. Rotenberg, J. C. Horvath and A. Pascual-Leone, eds, 'Transcranial Magn. Stimul. Neuromethods, vol. 89', Springer Protocols, chapter 6, p. 384.

Čuntala, J. (2006), Simulation of electromagnetic shielding in COMSOL multiphysics environment, *in* 'COMSOL Users Conf.', Prague.

Vidal-Dourado, M., Conforto, A. B., Caboclo, L. O. S. F., Scaff, M., Guilhoto, L. M. D. F. F. and Yacubian, E. M. T. (2013), 'Magnetic Fields in Noninvasive Brain Stimulation.', *Neuroscientist* .

Wagner, T., Rushmore, J., Eden, U. and Cabre, A.-V. (2009), 'Biophysical foundations underlying TMS: Setting the stage for an effective use of neurostimulation in the Cognitive Neurosciences', *Cortex* **29**(6), 997–1003.

Wagner, T., Valero-Cabre, A. and Pascual-Leone, A. (2007), 'Noninvasive human brain stimulation.', *Annu. Rev. Biomed. Eng.* **9**, 527–565.

Walsh, V. and Pascual-Leone, A. (2003), *Transcranial Magnetic Stimulation: A Neurochronometrics of Mind*, The Massachusets Institute of Technology Press, Cambridge, Massachusets.

Wassermann, E. M. (1998), 'Risk and safety of repetitive transcranial magnetic stimulation', *Electroencephalogr. Clin. Neurophysiol.* **108**(1), 1–16.

Weast, R. C. (1989), *CRC Handbook of Chemistry, and Physics*, 70 edn, CRC Press, Boca Raton.

Wintrich, A., Nicolai, U., Tursky, W. and Reimann, T. (2011), *Application Manual Power Semiconductors*, SEMIKRON International GmbH.

Wolf, A. V. (1966), *Aqueous Solutions and Body Fluids*, Harper and Row, New York.

World Health Organization (2014), 'Schizophrenia: fact sheet'. [Accessed May 27th, 2015].
URL: *http://www.who.int/mediacentre/factsheets/fs397/en/*

World Health Organization Regional Office for Europe (2012), 'Depression in Europe'. [Accessed May 27th, 2015].
URL: *http://www.euro.who.int/en/health-topics/noncommunicable-diseases/mental-health/news/news/2012/10/depression-in-europe*

Young, H. D., Freedman, R. A. and Ford, A. L. (2004), *Sears and Zemanzky's university physics : with modern physics*, 13 edn, Addison-Wesley.

Zangen, A., Roth, Y., Voller, B. and Hallett, M. (2005), 'Transcranial magnetic stimulation of deep brain regions: Evidence for efficacy of the H-Coil', *Clin. Neurophysiol.* **116**, 775–779.